UNIVERSITY OF OKLAHOMA

GRADUATE COLLEGE

WIND TURBINE CLUTTER IN WEATHER RADAR: CHARACTERIZATION AND MITIGATION

A DISSERTATION

SUBMITTED TO THE GRADUATE FACULTY

in partial fulfillment of the requirements for the

degree of

DOCTOR OF PHILOSOPHY

By

FANXING KONG
Norman, Oklahoma
2014

WIND TURBINE CLUTTER IN WEATHER RADAR:
CHARACTERIZATION AND MITIGATION

A DISSERTATION APPROVED FOR THE
SCHOOL OF ELECTRICAL AND COMPUTER ENGINEERING

By

Dr. Robert Palmer

Dr. Yan Zhang

Dr. Scott Greene

Dr. Tian-You Yu

Dr. Guifu Zhang

Dedication

To my boy Jason.

Acknowledgements

First and foremost I want thank my lovely wife, Qing, for her support and tolerance in the past year. I am deeply grateful for her sacrifice to take good care of our child so that I can devote more time working on the dissertation. I also need to thank our little one, Jason, for bringing so much joy to my life and teaching me how to love. I thank my parents Yufang Wang and Qinghua Kong, for coming from thousands of miles away and help me out through this difficult time without ever complaining. I also need to thank my mother-in-law Li Li, for all her help and God bless her fighting cancer. I need to thank my grandma Yanming Han for always supporting me since I was a boy. I wish I were there to say goodbye to you when you were gone.

Next I must thank my advisors and mentors, Dr. Robert Palmer and Dr. Yan (Rockee) Zhang. You gave me the opportunity to start a program at OU six years ago. You always encourage me to pursue new ideas. I have been enjoying working with both of you, through which I gained tremendous knowledge. I also want to thank my committee members Dr. John Scott . Greene, Dr. Tian-you Yu and Dr. Guifu Zhang. I appreciate your help and support throughout my study at OU.

Finally, I want to thank my buddy Redmond Kelly, not only for your countless help in debugging various strange hardware problems, but also your "Kelly style" hospitality. I am looking forward for a camping reunion with you guys in the near future. Maybe, China?

Contents

List Of Tables

List Of Figures

Abstract

With the rapid growth of the wind power industry, many commercial utility-scale wind turbines have been built across the country. These extremely large man-made structures are reported to have negative impact on nearby radars due to their complex scattering mechanisms. Various forms of clutter effect caused by wind turbines in the radar vicinity are generally referred to as the Wind Turbine Clutter (WTC).

Due to the lack of awareness on this newly recognized clutter, many wind farms have been built in the Line of Sight (LOS) coverage of operational radars, potentially affecting their performance. Weather radar is the one affected most by WTC because the target of interest is precipitation particles, which is spatially inseparable from the wind turbine within the clutter contaminated resolution volume. Our study thus focuses on analyzing the cause of different types of clutter effects by wind turbines, characterizing the radar signatures of such clutter and mitigating the clutter effect for weather radar.

The Micro-Doppler signature of the WTC reveals interesting time-variant spectrum features which are closely related to the instantaneous motions of the wind turbine. The complex motions of a wind turbine can be mostly characterized by three rotations: roll, pitch and yaw. Electromagnetic (EM) characterization of such a dynamic electrical large target is challenging. Various scattering mechanisms are analyzed and the back scattered field and RCS of the wind turbine are computed using commercial EM solver and a hybrid high-frequency approximation approach developed from our study.

Field measurements were carried out by deploying the mobile radar to wind farms. The measurements give us the first non-aliased Doppler spectrum of wind turbines. In order to synchronize the wind turbine motion with radar data acquisition, the Radar Wind Turbine Testbed (RWT^2) was developed for indoor scaled measurements, which includes the scaled wind turbine model and the scatterometer. Both frequency and

time domain measurements were made to characterize the statistics of return signal from the wind turbine model.

Several mitigation schemes developed from our study will be discussed, including the telemetry based method, the Adaptive Spectrum Processing (ASP) and the mitigation scheme for moment data based on the Maximum A Posterior (MAP) criteria. A thorough analysis of utilizing LOS avoidance to prevent WTC at the first place will be presented at the end.

Chapter 1

Introduction

1.1 A Brief History of Radar

RADAR is the acronym for RAdio Detection And Ranging. There are various versions of the origin of radar, because many countries began the development of radar at almost the same time during World War II due to wartime needs. However, the theoretic foundation all originated from Scottish mathematical physicist James Clerk Maxwell's work on electromagnetism. He first established the sets of differential equations that form the foundation of classical electrodynamics [1], famously known as Maxwell's Equations. The equations predict the existence of oscillating electric and magnetic fields that travel at the same speed as light. His work led to a unified model of electromagnetism, which became one of the greatest advances in physics of all time.

Maxwell's theory was later verified by German physicist Heinrich Rudolf Hertz, who conclusively proved the existence of Electromagnetic (EM) waves by experiments and discovered that EM waves were reflected from metallic surfaces [2]. Inspired by Hertz's work, the German entrepreneur Christian Huelsmeyer invented his apparatus "Telemobiloscope" for ship collision avoidance, which is often considered to be the first radar in the world. The device could not directly measure the distance, thus not fully meriting the name of radar. However, it is the first patented device that detects targets in distance. The Telemobiloscope is shown in Fig. 1.1 and it was patented in 1904.

Figure 1.1: Christian Huelsmeyer's invention of "telemobiloscope" displayed at the Deutsches Museum in Munich. The antenna is on the left, the receiver in the middle, and the transmitter is on the right. If a target is detected, the bell keeps ringing until it moves out of the field-of-view. The detecting range is 3000 m. Picture from the "RADAR WORLD" $http://www.radarworld.org/huelsmeyer.html$.

By late 1930s, the concept of using radio waves to detect targets was well established in many countries. Pulsed waveforms were used to obtain the range information. The installation of aircraft detection and tracking stations in England, namely "The Chain Home" as shown in Fig. 1.2, provided early warnings that helped the Royal Air Force win the Battle of Britain over Germany in 1940 [3]. The success in England urged many other countries to begin developing and deploying radar in the battlefield. Almost simultaneously, the US, Germany and Japan, etc., developed their own radar designs. The radar system at that time were mostly ground based with large antennas, until the high-power microwave cavity magnetron technique was invented. The magnetron is a key advance in radar technology, allowing much smaller antennas to be used, which makes it possible to be carried by mobile platforms such as ships and aircrafts.

After the war, radar technologies continued a rapid growth. As high-power stable amplifiers such as klystron, traveling wave tube and solid state transistors were invented, phase coherency could be ensured and the Doppler effect was applied in many radar systems. The Moving Target Indicator (MTI) and pulse Doppler

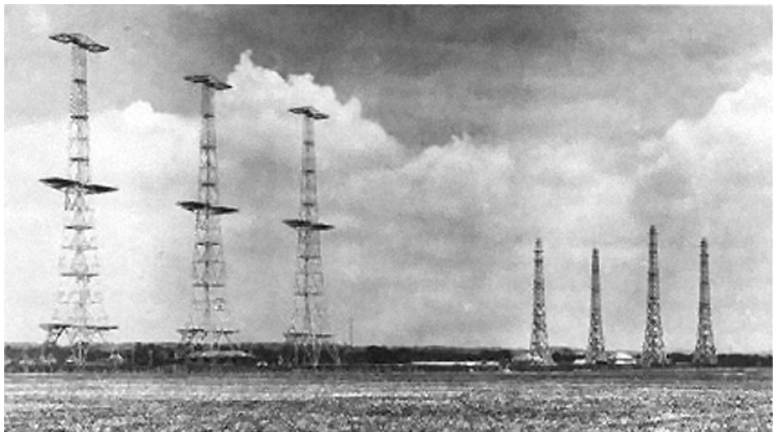

Figure 1.2: The coastal early warning radar stations built by the British during World War II. The system was called Radio Direction Finding. Though the antennas were stationary, the incoming direction could be estimated by comparing the received signal strength from a pair of antennas at right angle.

radar technologies were developed to separate moving targets from ground clutter by Doppler processing. The Doppler information extends radar observations beyond three-dimensional space, thus Doppler radar is sometimes referred to as 4-D radar with an extra dimension of the Doppler domain. The highly stable signal source also allows complex waveforms to be used for pulse compression, so that high transmit energy and fine range resolution can be achieved simultaneously.

Phased array technology was also adopted in radar to electronically steer the beam, offering rapid beam steering without mechanical movement of the antenna. A larger array aperture provides finer angular resolution, which leads to better cross range resolution. However, such a large array is impossible to carry on the mobile platforms such as aircraft and satellite. The Synthetic Aperture Radar (SAR) simulates a large array using only one antenna, by coherently recording along the platform orbit and then synthesizing the data for high angular resolution. Normally combined with pulse compression for high range resolution, SAR can provide high-resolution images, which has important applications in remote sensing and mapping of the surface.

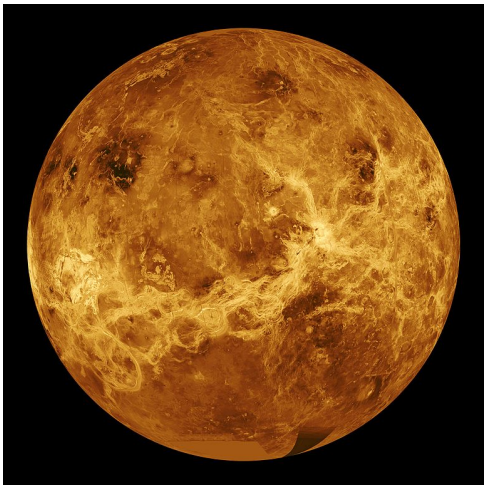

Figure 1.3: Venus SAR mosaics. The thick carbon dioxide atmosphere does not allow visible light to penetrate, but with the 13-cm microwave signal, the radar can penetrate the atmosphere and build up images of the surface. Picture from: *http* : *//photojournal.jpl.nasa.gov/catalog/PIA*00104

The technology of SAR imaging has been extensively exploited by NASA (National Aeronautics and Space Administration). Fig. 1.3 shows the rendered SAR image of the Venus surface from the NASA Venus radar mapper, known as the "Magellan".

As both the range and angular resolution become finer, radar engineers were not satisfied with the "blob" detection any more. High-resolution radar images not only provide the range and azimuth information, but also the detailed geometry of the target, which can be used for target identification and classification. EM numerical simulations and scaled measurements were also developing at the same time in order to establish the "radar signature knowledge base" for various targets for identification purpose.

Over The Horizon (OTH) radar is another technology quickly developed after the war. These radars extend the detection range beyond the horizon by using the ionosphere reflection. The concept that EM waves at High Frequency (HF), which is 3-30 MHz of the microwave spectrum, can be reflected from the ionosphere is not

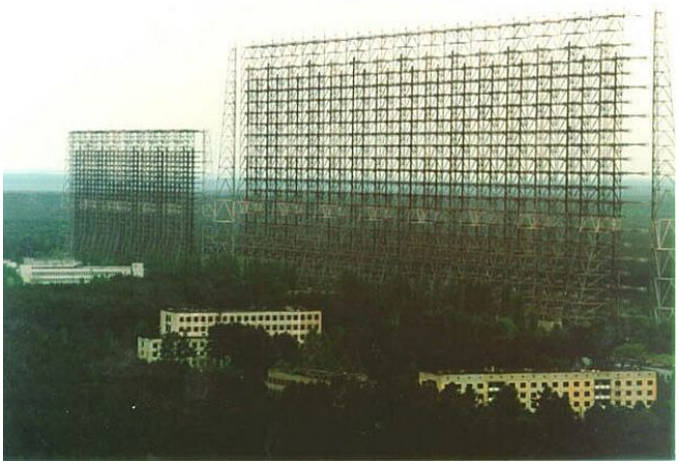

Figure 1.4: The Duga-3 OTH radar, part of the Soviet early-warning network. It was famously known in the amateur radio community as the "Russian Woodpecker", because it transmitted at an extremely high power of over 10 MW and interfered with the shortwave radio. The intercepted signal sounds like a sharp, wood-tapping noise. Picture source: *http* : *//www.panoramio.com/photo/*17261939

new. But applying it to radar was not practical due to extremely high sensitivity requirements until the first Low Noise Amplifiers (LNA) were designed in 1960s. The OTH radar was deployed as a bistatic early warning system to take advantage of its extended coverage. The aperture of the antenna array is usually extremely large in order to achieve acceptable cross range resolution in the far distance at HF band. Most OTH radars in the world were installed during the Cold War to meet the needs for accurate long-range detection and tracking of aircrafts and missiles. Fig. 1.4 shows the early warning system installed by the Soviet Union during the Cold War.

After the Cold War, radar technology found applications in civilian use and one such important application is weather radar, which has become a critical tool for the meteorologists to observe the atmosphere. Weather radars are used for measuring precipitation and wind shear. There are also vertical pointing profiling radar for clear air observation. Modern weather radars are mostly pulse-Doppler, capable of accurately

Figure 1.5: The Phase Array Radar in Norman, Oklahoma. The array antenna is from military radar AN/SPY-1A. PAR is the key instrument of the National Severe Storm Laboratory (NSSL) weather radar testbed for developing new algorithms and investigating the feasibility of multi-mission phase array radar. Photo is provided through the courtesy of A. Zahrai.

detecting the motions of hydrometers as well as the intensity. Weather radar observations are extensively used in predictions of severe weather, such as thunderstorms and tornadoes. The data are also incorporated into Numerical Weather Prediction (NWP) models to improve analyses and forecasts. Advanced radar technologies such as phase array has also been experimented in weather radar. Fig. 1.5 shows the Phase Array Radar (PAR) being installed for weather observation. The electronic scan can greatly enhance the storm prediction lead time.

Rapid advances in digital technology have made many theoretical discussions in the past practical with digital signal processing. Substituting analog components with digital circuits all the way to the RF (Radio Frequency) front end will make the system easily reconfigurable and less susceptible to interference. The fast evolving digital electronics also makes it possible to apply Software Defined Radio (SDR) to radar

Figure 1.6: A commercial hand-held speed gun "genesis hand-held directional", which is used to detect the speed of vehicles, locking and tracking up to two targets. Picture is from *http* : *//www.decaturelectronics.com*

Figure 1.7: Single-chip 24 GHz radar transceiver by ViaSat: a Frequency Modulated Continuous Wave (FMCW) radar on a 5 mm $\times$ 5 mm chip.

system design. Abstracting the system reconfigurability to software level will greatly simplify system upgrades as most can be done by changing the software. Significant amount of signal processing tasks are handled by the general-purpose processor such as Digital Signal Processor (DSP) instead of the special-purpose hardware. Introducing consumer electronics in radar systems will bring down the cost of the radar and largely expand radar applications in the civilian market. Fig. 1.6 shows a hand-held radar used by highway patrols to detect the speed of oncoming traffic.

Modern radar systems also benefit from the dramatic development of the semiconductor industry. More MMICs (Monolithic Microwave Integrated Circuit) are being used in radar transceiver module. A complete radar system can be fabricated on a single circuit board, or even a single chip as shown in Fig. 1.7. The advances in electronics have been gradually transferring the general public's impression on radar from a bulky heavy military device to portable miniature gadget. As the trend continues, more radar applications will be seen in everyday life.

1.2 Radar Fundamentals

As an active sensor, radar can operate both day and night. It is also able to work in fog, haze, rain, etc., conditions that are impervious to optical sensors. Fig. 1.8 shows the basic principles of a radar. First, the transmitter generates the signal with designed waveform at radio frequency. The signal is converted to EM waves through the antenna and radiated into the space in the desired direction. Some energy is scattered by targets and/or clutter back to the antenna and then converted to the electric signal. The received signal is comprised of target information together with interference such as clutter and noise, which needs to be further processed for target detection and estimation, etc. Some basic concepts about the radar is briefly introduced in the following.

• ***Radar Frequency*** is in the radio spectrum as the name suggests, which is the EM oscillation from approximately 3 kHz to 300 GHz. However, most radars operate in the microwave region, ranging from 3 MHz to 300 GHz [4]. Letter designations have been used and continued throughout the years to describe the frequency band of radar operation since World War II. These designations have been widely accepted by radar engineers, thus becoming the IEEE standard [5]. The letter designation and corresponding frequency range is shown in Table 1.1, where some typical applications are listed for each band. Microwave propagation characteristics change drastically as

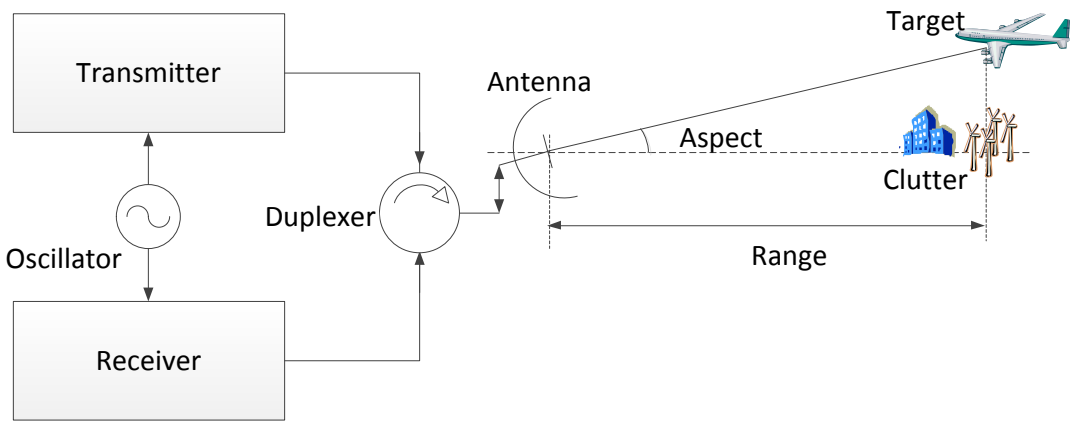

Figure 1.8: Demonstration of how the radar works: a mono-static setup is shown here, where the same antenna is used for both transmitting and receiving through a directional duplexer. There are also radars with a bi-static setup where the transmitting and receiving antennas are located separately, which is less common than this mono-static configuration.

Table 1.1: IEEE standard of radar frequency band letter designation

<table>
<tr><th>Band designation</th><th>Frequency</th><th colspan="2">Typical radar applications</th></tr>
<tr><td>HF</td><td>3-30 MHz</td><td rowspan="2">OTH early warning radar</td><td>Ionosond</td></tr>
<tr><td>VHF</td><td>30-300 MHz</td><td rowspan="2">GPR(Ground Penetrating Radar</td></tr>
<tr><td>UHF</td><td>300-1000 MHz</td><td>Wind profiler</td></tr>
<tr><td>L</td><td>1-2 GHz</td><td colspan="2">Long range surveillance radar</td></tr>
<tr><td>S</td><td>2-4 GHz</td><td>Air traffic control</td><td rowspan="2">Weather radar</td></tr>
<tr><td>C</td><td>4-8 GHz</td><td rowspan="2">Airborne imaging radar</td></tr>
<tr><td>X</td><td>8-12 GHz</td><td>Marine radar</td></tr>
<tr><td>Ku</td><td>12-18 GHz</td><td colspan="2">Short range surveillance radar</td></tr>
<tr><td>K</td><td>18-27 GHz</td><td colspan="2" rowspan="2">Police radar, traffic radar</td></tr>
<tr><td>Ka</td><td>27-40 GHz</td></tr>
<tr><td>V</td><td>40-75 GHz</td><td colspan="2">Vehicular radar</td></tr>
<tr><td>W</td><td>75-110 GHz</td><td colspan="2">Cloud radar</td></tr>
<tr><td>mm</td><td>110-300 GHz</td><td colspan="2">Experimental radar</td></tr>
</table>

the frequency varies, and the actual operating frequency of a radar system is normally a trade-off of many practical physical and engineering constraints.

• ***Range*** refers to the one-way propagation distance from the antenna to the target, which can usually be approximated by the line-of-sight distance under normal atmosphere condition for near to mid range targets. The slant range due to elevation or grazing angle is often projected to the ground to conveniently map the target location as shown in Fig. 1.8. Microwaves travel at the speed of light in free space. Therefore, target range R can be determined by the time it takes for the wave to travel to the target and back:

$$R = \frac{cT_d}{2} \tag{1.1}$$

where c is the speed of light, T_d is the time delay from sending out the signal to receiving the signal scattered back, and the factor of 2 in the denominator accounts for the round-trip distance assuming a mono-static configuration. Unless specifically pointed out, the mono-static configuration is used throughout this study. It is worth noting that equation (1.1) maps the range to time domain in a simple linear form. This means that time and range domain are equivalent except for a linear factor, which is one of the fundamentals of radar signal processing.

• ***Aspect angles*** (azimuth and elevation) are also needed to locate a target in 3-D space. The radar antenna is directional, which has high gain within a limited solid angle and relatively lower gain elsewhere. Pointing the antenna beam around illuminates different sectors in the space, from which the receiver will produce a "range profile". A 3-D surveillance map can then be generated once the beam sweeps through the entire volume of interest. The resolution in aspect is determined by the beamwidth in both azimuth and elevation, which are inversely proportional to the antenna aperture, i.e., the larger the antenna is, the higher resolution it has in that dimension. Higher resolution gives better accuracy in locating targets. However, it also takes longer to scan through the entire volume. Therefore, for rapid scanning radar such as the Air Traffic Control (ATC) radar, a parabolic dish antenna that forms a fan beam is often deployed. Compared with the pencil beam, which has similar resolution in both azimuth and elevation, a fan beam has much wider beamwidth in elevation, and only scans in azimuth. This type of radar only locates target in range and azimuth, but not in elevation, thus is often referred to as 2-D radar.

• ***Radar waveform*** refers to the signal that the radar transmits. For a long time after radar was invented, the transmitter could only send out continuous waves. As a result, targets in the same direction cannot be differentiated in range due to the lack of time reference. This was not changed until the pulsed transmitter was invented and widely deployed in World War II. Sending a pulsed signal into the environment

is equivalent to feeding a black-box system with a pulse excitation. The system can usually be well modeled as linear and fully characterized by the pulse response, which in radar terms is referred to as the range profile. Because the excitation is a pulse with finite width, the system impulse response is sampled with limited resolution. The range resolution, mapped from the time domain according to equation (1.1) is:

$$\delta_r = \frac{c\tau}{2} \tag{1.2}$$

where δ_r is range resolution and τ is pulse width. The narrower the pulse, the finer resolution the range profile has. For most conventional radar systems, pulses are sent out periodically to probe the ambient environment. This period is usually referred to as Pulse Repetition Time (PRT) or Pulse Repetition Interval (PRI) and the corresponding frequency is the Pulse Repetition Frequency (PRF). For pulsed radar, locating the target in range relies on referencing returned signal to corresponding transmitted pulse in the time domain. Therefore, periodically transmitting pulses may result in range ambiguity as the actual reference pulse may be sent more than one period before the received signal, in which case is referred to as the second-trip echoes. The range beyond which the targets appear as second-trip echoes is defined as the maximum unambiguous range, R_{un}, mapped from the time domain as:

$$R_{un} = \frac{ct_p}{2} = \frac{c}{2f_p} \tag{1.3}$$

where t_p and f_p are the PRT and PRF, respectively. It is obvious that the longer the PRT, the larger the maximum unambiguous range. However, there are other constraints that limit PRT, which will be discussed next. Although periodic pulse signal is the most common in radar systems, it is worth noting that radar signal takes a variety of waveforms for different applications.

- ***Doppler*** effect in radar is the change of received frequency from the transmit frequency of a wave due to the relative radial movement between the radar and the

target. The received wavelength of scattered wave is the distance between two consecutive wave fronts for a sine wave, which is slightly off from the transmit wavelength by ΔR due to the relative movement:

$$\Delta R = 2v_r \frac{\lambda}{c} \tag{1.4}$$

where λ is the wavelength of transmitted wave, v_r is the radial velocity, which is positive if receding ($\Delta R > 0$) and negative if approaching ($\Delta R < 0$). Thus, the received wavelength is:

$$\lambda_r = \lambda + \Delta R \tag{1.5}$$

And the received frequency is $f_r = c/\lambda_r$. The frequency offset caused by the relative motion is often referred to as the Doppler frequency:

$$f_d = f_r - f = \frac{c}{\lambda_r} - \frac{c}{\lambda} \tag{1.6}$$

Substituting equation (1.5) into the above:

$$f_d = \frac{-2v_r}{\lambda(1 + 2v_r/c)} \tag{1.7}$$

where v_r is much smaller compared to c for normal radar targets, thus $v_r/c \approx 0$. This gives a simple linear relation between the Doppler frequency and the radial velocity:

$$f_d = -\frac{2v_r}{\lambda} \tag{1.8}$$

It is worth noting that the Doppler frequency has opposite signs with respect to the radial velocity, i.e., $f_d > 0$ for approaching target and $f_d < 0$ for receding target. Therefore, the observed frequency is higher than the transmit frequency during target approaching and lower during recession. The implication of equation (1.8) is that the target radial velocity can be estimated by measuring the Doppler frequency, which is often referred to as the Doppler processing.

For conventional pulsed radar, multiple pulses are sent out periodically to sample the target movement. The sampling occurs in the time domain, but it is most

straightforward to convert the sampled time series into the frequency domain by Discrete Fourier Transform (DFT). Numerous methods have been studied for Doppler processing, either to speed up the process for real-time implementation, or to improve the estimate accuracy by incorporating prior knowledge about the target movement such as the Auto Regressive Moving Average (ARMA) model, MUltiple SIgnal Classification (MUSIC), etc. or compromising spectral resolution based on different windowing [6].

Where there is sampling, there is aliasing. The Nyquist Sampling Theorem applies to Doppler processing. If the sampling frequency, which is PRF in this case, is too low, then spectrum aliasing will occur [7]. To avoid this velocity aliasing, high PRF is preferable; however, it is worth noting that PRF increase is limited to avoid range folding. The selection of PRF for the radar system is therefore a trade-off between the maximum non-aliasing velocity and maximum non-aliasing range, this is often referred to as the "Doppler Dilemma".

• ***Receiver noise*** is the noise signal generated by the radar receiver. A major source of the receiver noise is the thermal agitation of the conduction electrons in the ohmic portion of the receiver circuits. Thermal noise is white, spreading the entire spectrum. However, radar receivers have band-limited frequency response. The thermal-noise power at the input of a receiver is [4]:

$$\sigma_n^2 = kTB_n \tag{1.9}$$

where k is the Boltzmann's constant, T is the receiver temperature in Kelvin and B_n is the noise bandwidth, which is often approximated by the receiver 3 dB bandwidth. The ratio of signal over noise power is usually referred to as the Signal-to-Noise Ratio (SNR), which is an important figure to evaluate the detectability of radar targets. The SNR at the input of radar receiver is the received target signal power over the input noise power. The SNR at the output of the receiver, however, will be lower and

the noise figure F_n is defined as a measure of the degradation of SNR as the signal passes through the receiver:

$$F_n = \frac{S_{in}/N_{in}}{S_{out}/N_{out}} \tag{1.10}$$

where N_{in} is the noise power at a standard temperature $T_0 = 290K$. Thus, the signal power at the input of the receiver in terms of output SNR is:

$$S_{in} = KT_0BF_n(SNR)_{out} \tag{1.11}$$

where the output SNR is proportional to the input signal power.

• ***Radar Equation*** relates target range to radar system parameters and target characteristics. It is the most intuitive way to understand how various factors contribute to the radar performance. It is also an important tool for designing radar systems. If the transmit power P_t is radiated into the space through an antenna with a gain of G, the incident power density at the target is:

$$W_{in} = P_t\frac{G}{4\pi R^2 l(R)} \tag{1.12}$$

where $l(R)$ is the one-way propagation attenuation, which can be significant in case of moist air. The target intercepts part of the energy and scatters in all directions, some of which is scattered back toward the radar. Radar Cross Section (RCS) characterizes the ability of an object to capture the EM energy and re-radiate in given direction, which, if not otherwise stated, is the direction going back to the radar. RCS is usually highly directional and is analogous to the directivity of an antenna. Thus, the scattered power density at the radar is:

$$W_s = P_t\frac{G}{4\pi R^2 l(R)} \cdot \frac{\sigma}{4\pi R^2 l(R)} \tag{1.13}$$

where σ is the target RCS. The antenna can only capture a portion of the scattered EM energy, and the amount is measured by the effective area A_e, which is proportional to the gain:

$$A_e = \frac{G\lambda^2}{4\pi} \tag{1.14}$$

Thus, the receiver input is:

$$S_{in} = \frac{P_t G A_e \sigma}{(4\pi)^3 R^4 l^2(R)} = \frac{P_t G^2 \lambda^2 \sigma}{(4\pi)^3 R^4 l^2(R)} \tag{1.15}$$

Comparing this with equation (1.11), the complete form of radar equation is obtained as follows:

$$R = \left(\frac{P_t G^2 \lambda^2 \sigma}{(4\pi)^3 K T_0 B F_n l^2(R) (SNR)_{out}} \right)^{\frac{1}{4}} \tag{1.16}$$

The radar equation interprets the relation of radar range in terms of radar system parameters and the target RCS. It is also worth noting that the receiver output SNR decreases to the fourth order of target range, indicating the target return power will drop rapidly as it goes away from the radar.

• ***Clutter*** is a relative term, which refers to any unwanted radar echoes from the ambient environment. For example, ATC radar is designed to detect aircrafts, thus echoes from the rain becomes clutter. On the other hand, for weather radar, rain is the desired target, and airplanes will be considered clutter. Another example is that biological scatters from birds and insects are clutter for weather radar observations, but desired targets for radar aeroecology studies [8].

Compared with the receiver noise, which is inherent to radar systems, clutter signals are more dependent on observed clutter objects. The larger RCS the clutter object has, the stronger radar echo it produces. Careful design of radar receiver can lower the noise power thus increasing SNR, but will not improve the Signal-to-Clutter Ratio (SCR), which is solely determined by target and clutter radar characteristics. In most cases, if the signal power is lower than the noise, it will be extremely difficult to detect the target. However, SCR can be very low due to strong clutter echoes from large structures, yet the target signal can still be recovered by clutter filtering based on the prior knowledge of the clutter spectrum, which will be further explored in the next chapter.

Airborne radar suffers from surface clutter contamination, shipborne radar works against sea clutter, and ground based radar deals mostly with buildings and terrains.

Some of these clutter types have been well studied in the past, based on which many clutter filtering techniques have been developed [9–11]. The rapid development of wind power in the past decade has led to many wind turbines in large groups emerging from the landscape, which has been discovered to have clutter effect on radar observations. This recently recognized radar clutter is called Wind Turbine Clutter (WTC) [12], and will be the focus of this study.

• ***Radar Cross Section*** was briefly introduced in the process of deriving the radar equation. There are two forms of definition for RCS, which are essentially the same, but emphasizing from different perspectives. One is from the point of view of EM field as shown in equation (1.17):

$$\sigma = \lim_{R\to\infty} 4\pi R^2 \frac{|E_s|^2}{|E_i|^2} = \lim_{R\to\infty} 4\pi R^2 \frac{|H_s|^2}{|H_i|^2} \tag{1.17}$$

where R is target range, E_i and H_i are the incident electric and magnetic field intensities at the target, E_s and H_s are the scattered electric and magnetic field intensities at the radar receiver. As R approaches infinity, σ is only determined by the target characteristics and radar frequency. Another definition of RCS can be derived from equation (1.13) and (1.15):

$$\sigma = \lim_{R\to\infty} 4\pi R^2 \frac{S_{in}}{A_e} \frac{1}{\frac{P_t G}{4\pi R^2}} = \lim_{R\to\infty} 4\pi \frac{W_s}{W_{in}} \tag{1.18}$$

It is obvious the two definition are the same, only that equation (1.18) is from the measurement aspect. It is also worth noting that the following criteria is often used to justify if R is large enough to meet the far field criteria:

$$R \geq \frac{2L^2}{\lambda} \tag{1.19}$$

where L is the larger of the antenna aperture and the longest target dimension. RCS has the same unit as area, though it is not determined by the actual physical cross section of the target. For example, a small corner reflector can have RCS of more than ten times of its physical cross section. The RCS of a complex target varies quickly in

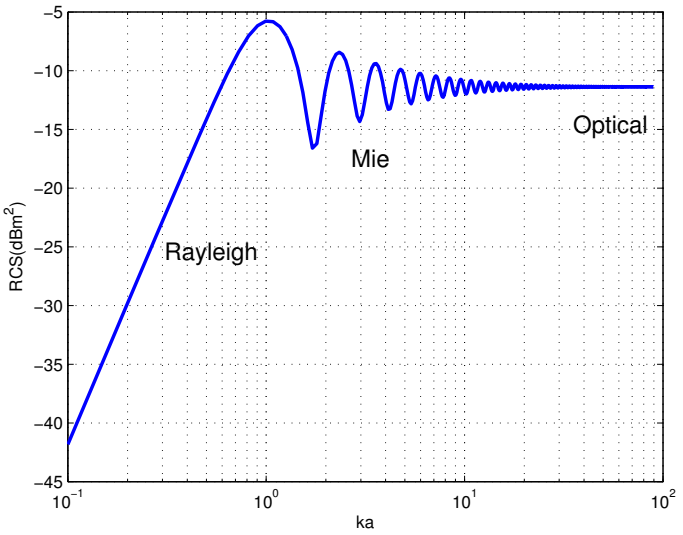

Figure 1.9: The RCS variation of a 12-inch metal sphere in terms of electrical scale. Notice as the electrical scale moves into the optical region, the RCS gradually converges to the physical cross section of the sphere, which can be misleading as the RCS is not necessarily determined by the physical cross section of the target.

a large dynamic range as the viewing angle changes, thus often represented in decibel unit, such as dBm^2.

$$1\,dBm^2 = 10log_{10}(1\,m^2) \tag{1.20}$$

The RCS of a target also varies as the frequency changes. In terms of the electrical scale, the RCS variation versus frequency can be divided into three regions: Rayleigh, Mie and Optical as is shown in Fig. 1.9. In Rayleigh region, the wavelength is larger than the target, normally with $ka < 0.5$, where $k = \lambda/2\pi$ is the wave number, while a is the longer target dimension. The RCS in this region is inverse-proportional to the 4^{th} power of wavelength. Thus, the bigger the target is, the larger its RCS becomes. When the target size is comparable to wavelength, however, the RCS starts to oscillate and this is called the Mie region. As the electrical scale keeps increasing,

the RCS will converge at certain point, which corresponds to the Optical region. There is not a clearly defined border between Mie and Optical regions. However, $ka = 20$ is often used to discriminate the two. In the Optical region, the target RCS is mostly determined by its shape and build material. It is worth noting that a complex target like a wind turbine is composed of many parts, each of which itself can be a complicated shape that may fall into any of the three regions.

1.3 Wind Power and Wind Turbines

Wind energy is an ancient energy resource discovered long ago. The conversion of wind energy to other more useful forms of energy is called wind power, including but not limited to: using wind turbines to obtain electrical power, windmills for mechanical power, wind pumps for water pumping and sails to propel ships. The earliest recorded usage of wind power by sails to propel boats can be traced back to 3200 B.C., where reed boats sailed upstream against the River Nile's current. Nowadays, wind energy is more often converted to electricity by large wind turbines, which can then be used for various applications.

Wind energy is renewable compared to conventional fossil fuels such as coal, oil and natural gas for generating electricity. It is also a clean energy resource since it has no emissions and consumes little water for electricity production. The development of this green and renewable energy solution helps diversify the energy portfolio. It also relieves energy dependency on fossil fuels and reduces greenhouse gas emissions. Therefore, wind power has been the fastest growing renewable energy sector compared to hydroelectricity, geo-thermal, biofule, solar energy and tidal power, etc.

In the past decade, the total installed wind power capacity in the US has been growing exponentially as shown in Fig. 1.10. The overall total wind power capacity reached 60 GW by the end of 2012 [13], a 15 times increase in one decade. A report released by the Department of Energy has discussed the scenario of providing 20%

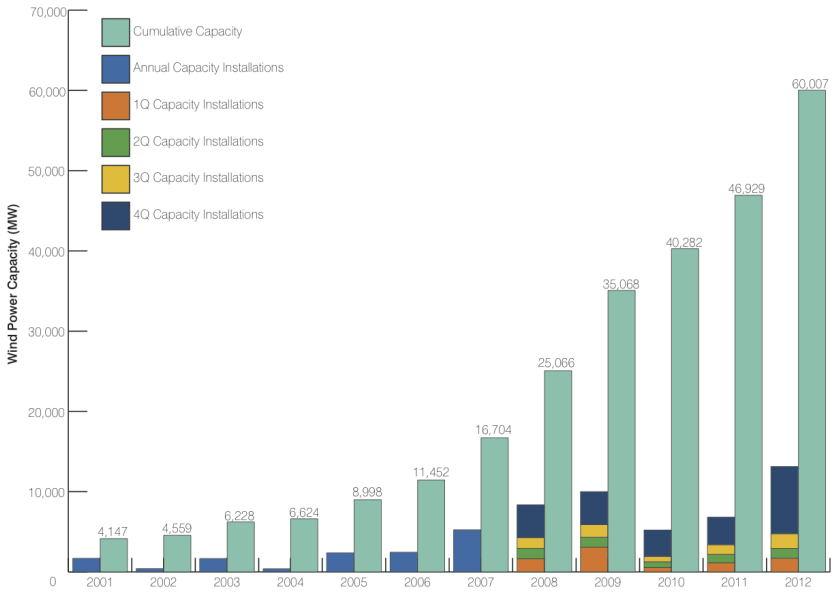

Figure 1.10: Quarterly, annual and cumulative wind power capacity growth in US from 2001 to 2012. Picture source: 2012 fourth quarter AWEA (American Wind Energy Association) market report. The quarterly installation data became available from 2008.

of the Nation's electricity needs using wind power by year 2030 [14]. Worldwide, the total installed wind power reached 282.5 Gigawatts in 2012, an increase of 10 times in less than a decade, among which China (75.6 GW), US (60 GW) and Germany (31.3 GW) are the top three countries by nameplate wind power capacity, accounting for about 60% of the world total wind power capacity. The rapid development of wind power in the recent decade is driven by the urgent needs to replace fossil fuels with renewable energy sources. Federal and state tax subsidies help lower the price of wind power generated electricity. On the other hand, the average cost for electricity production by wind power keeps decreasing because of improvement in manufacturing technology of wind turbine generators.

A wind turbine generator, often called the wind turbine, is a device that captures kinetic wind energy and converts it to electricity. The first electricity-generating wind

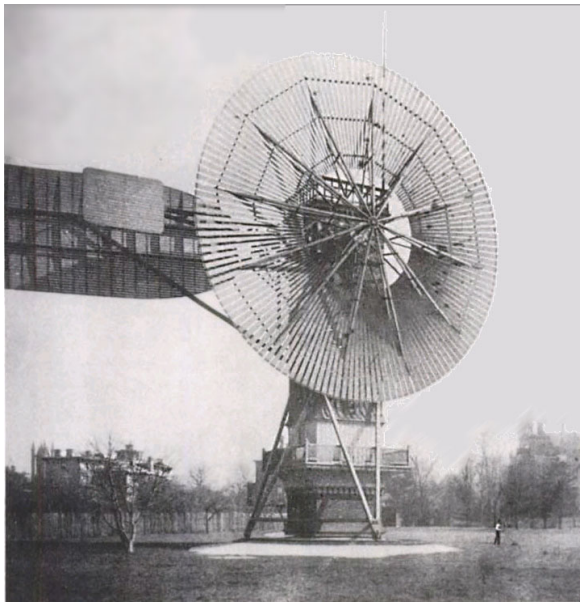

Figure 1.11: The first automatically operated wind turbine, built by American inventor Charles F. Brush, in Cleveland, Ohio, 1887. It was 18-m tall, weighted 4 tons and powered a 12-kW generator. Picture from: $http://www.generationeohio.com/$

turbine was a battery charging machine installed in July 1887 by Scottish academic James Blyth [15]. And the first automatically operated wind turbine generator was built by American inventor Charles F. Brush in Cleveland, Ohio as shown in Fig. 1.11. Today's wind turbines are manufactured in various types and sizes for a wide range of applications. Based on the direction of rotor shaft, wind turbines can be categorized as Vertical-Axis Wind Turbine (VAWT) and Horizontal-Axis Wind Turbine (HAWT). VAWT has the main shaft pointing vertically. The turbine of this kind can be driven by any horizontal wind from any directions, which is an advantage for sites where the wind direction changes quickly. This makes VAWTs particularly suitable for roof tops of buildings in the city. However, the inherent low efficiency and high torque makes VAWTs much less popular than HAWTs.

The blade rotation axis of a HAWT must be pointing into the wind for maximum efficiency. To achieve this, small turbines are driven by a special tail design like a

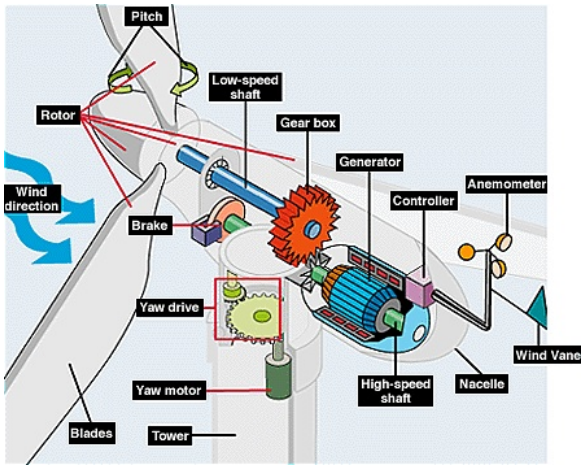

Figure 1.12: Typical HAWT structure. The gear box shown only has one stage for simplification, however, actual wind turbines may have multiple stages. Multiple gears are used for yaw driving. Picture provided through the courtesy of the Office of Energy Efficiency and Renewable Energy.

wind vane, while large turbines rely on a servo motor to actively drive a set of gears coupled to the yaw ring based on measurements from a wind vane. This driving system is often referred to as the yaw system. A gear box is usually used to couple the low-speed shaft and the high-speed shaft, bringing up the rotation speed to drive the generator, which resides in the nacelle on top of the tower as shown in Fig. 1.12.

In addition to the blade rotation and yaw, another moving part on a HAWT is the pitching mechanism of each blade. A wind turbine has a range of rotation rates, within which the generator is most efficient. The blades are thus feathered by the pitch mechanism to change the angle of attack so as to maintain a proper rotation rate as the wind speed changes. The wind speed at hub height is measured in real-time by the anemometer on top of the nacelle. Another usage of the pitch mechanism is to stall the blades. A cut-in speed is defined as the wind speed below which the electricity productivity is stalled and the cut-out speed is the wind speed above which the generator may be damaged. If the measured wind speed is lower than the cut-in

Table 1.2: Specifications of the GE 1.6-MW wind turbine

Parameter	**Value**
Capacity	1.6 MW
Hub height	80/100 m
Blade length	40.3 m
Blade diameter	82.5 m
Cut in speed	3.5 ms^{-1}
Rated speed	11.5 ms^{-1}
Cut out speed	25 ms^{-1}
Rotor speed	Variable
Blade material	Glass-fiber reinforced plastic

speed or higher than the cut-out speed, the wind turbine has to be actively stalled. In reality, two approaches are usually combined to properly stall wind turbines: all blades will be pitched to positions parallel to the wind and the break disc will also be activated.

Small wind turbines with capacity lower than 100 kW are often referred to as micro turbines, which are usually 2 to 8 m in diameter and produce 300 to 10,000 W output power. They are normally designed to be very lightweight and easy to install. These micro turbines can be found in many rural areas off the grid. The extremely large Megawatt wind turbines, often found in groups called wind farms, are utility-scale wind turbines, which are usually integrated to the grid. The hub height of such wind turbines can be over 100 m above the ground and the blade diameter ranges from 50 to 150 m. The GE 1.6-82.5M, as shown in Fig. 1.13, for example, is one of the most popular wind turbines from General Electric's product line. Some of the specifications are listed in Table 1.2. As the capacity of wind turbines increases, the

Figure 1.13: The state-of-the-art horizontal axis wind turbine manufactured by General Electric Company with a capacity of 1.6 MW. The wind turbine in the photo is installed near Minco, OK.

average manufacturing cost per watt has decreased consistently, which is why modern wind turbines have been designed with increasingly higher capacity.

The output power of a wind turbine is proportional to the 2^{nd} power of the rotor diameter and the 3^{rd} power of wind speed:

$$P_{out} = k\rho D^2 v^3 \tag{1.21}$$

where k is the efficiency coefficient, ρ is the air density, D is rotor diameter and v is the wind speed at hub height. It is obvious that the larger D is, the more wind energy a wind turbine can capture, which is why increasingly large rotor blades have been manufactured. Fig. 1.14 shows the size increase of wind turbines in the past 20 years.

As wind power becomes more popular, some environmental concerns have been raised as a result of installations of utility-scale wind turbines. Since the wind power consumes no fuel and emits no greenhouse gas, the impact on the environment in terms of air pollution is not an issue. However, there are reports of bird and bat mortality around wind turbines. Although all artificial structures can kill birds, wind turbines have a disproportionate effect on certain endangered species, such as golden

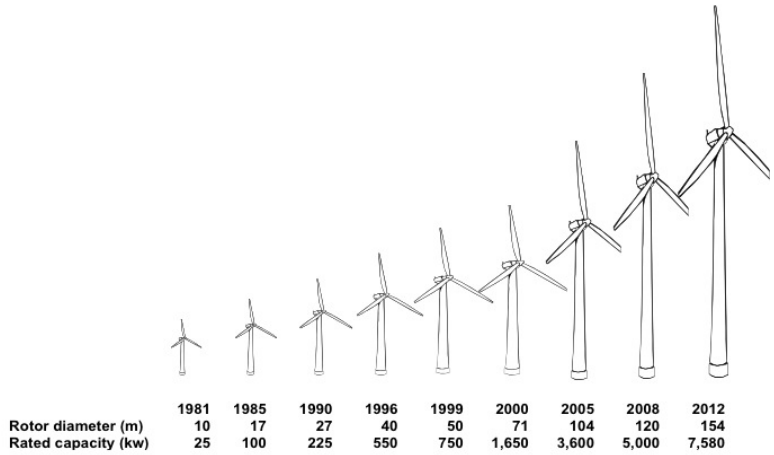

Figure 1.14: The rotor diameter and capacity increase of wind turbines from 1981 to 2012. Notice the capacity increase rate is approximately the square of rotor diameter increase rate.

eagles and raptors [16]. The actual cause and scales of impact depend on the specific circumstances and may require case-by-case studies. Another reported issue is the noise from spinning blades on people who live very close to wind turbines, although evidence on this is uncertain [17]. An important impact of wind turbines, however, has been found in the radar community, which will be discussed next.

1.4 Wind Turbines and Weather Radar Interaction

Wind energy is often criticized for being unreliable compared to fossil fuels. Whether the rotor blades are rotating and generating electricity is exclusively determined by the wind condition. The wind turbine stalls if the wind speed is less than the cut-in speed. If the wind speed is higher than the cut-out speed, the wind turbine also shuts down due to safety concerns. Therefore, uniform wind is important to increase the operating time of a wind turbine, and thus the amount of energy it actually produces.

According to equation (1.21), The amout of power that a wind turbine produces P_{out} is proportional to the third power of wind speed. Thus, sufficient wind speed is critical to meet the nominal capacity. At the bottom of the Planetary Boudary Layer (PBL) above the ground, surface friction from vegetation and topography cause turbulent eddies and chaotic wind patterns. As the altitude gets higher, however, the wind speed becomes more uniform and stronger due to a marked decrease in friction. An ideal location for a wind turbine would have a near constant flow of non-turbulent strong wind. Therefore, extremely tall towers have been built to place the blades higher above the ground. Many wind turbines are also installed on the top of ridges, where the wind is usually stronger and more uniform.

In addition, the average wind speed varies dramatically across the landscape. Based on past meteorological surveys, areas with high historic average wind speed are preferred for wind farm sites. Fig. 1.15 shows the estimated annual average wind speed at 80 m above the ground in the US. It is worth noting that the Midwest region has higher average wind speed, thus is usually selected for wind farm sites. As it will be mentioned later, this is also where many weather radars are located.

Weather radar is the type of radar used for detecting, locating precipitation and estimating its motions. It operates the same way as a generic radar by transmitting an EM wave and receiving backscattered signals, only that the targets of interest for weather radar are in different precipitation forms, such as rain, snow and hail, etc. The Next Generation Weather Radar (NEXRAD), also called Weather Surveillance Radar – 88 Doppler (WSR-88D) is the current weather radar network in the US, which includes 160 weather radars [18].

In 2013, the OPEN Energy Information (OPENEI) has updated the number of current wind farms in service to 1137, which accounts for a total installed wind power capacity of 60,688 MW. If projects under construction and proposed are included, there are 1295 wind farm projects in total, with potential to generate up to 87,624 MW

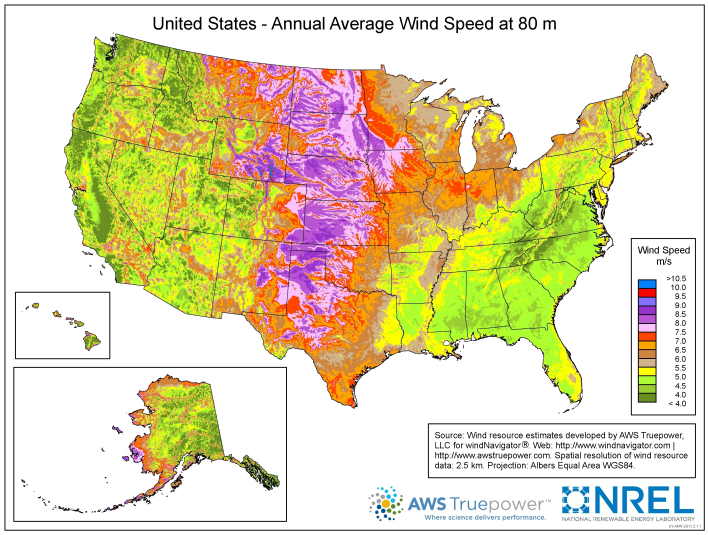

Figure 1.15: Wind resource distribution in the US: the annual average wind speed at 80 m above the ground. Picture from the National Renewable Energy Laboratory.

wind power. The interest in commercial wind power results in more wind turbines being installed in the radar Line of Sight (LOS) coverage.

The operating wind farms and NEXRAD radar in the contiguous US are pin pointed in Fig. 1.16. Combining this with the wind resource map, it is obvious that many wind farms are built in the Midwest, where the wind resource is most sufficient. Therefore, NEXRAD radars in the Midwest are the most affected by the wind power development. The weather radar in this area play an important role in the early warning of severe weather, such as tornado, flash flood, etc. Thus, it is critical to ensure that the wind farms near these radars have minimal impact on weather radar operations.

The distance to nearby NEXRAD radar from the wind farms aforementioned is calculated based on latitude and longitude obtained from the OPENEI database. This study is only concerned about wind turbines with nominal capacity greater than 250 kW, to exclude relatively small wind turbines. Wind farms with less than five wind

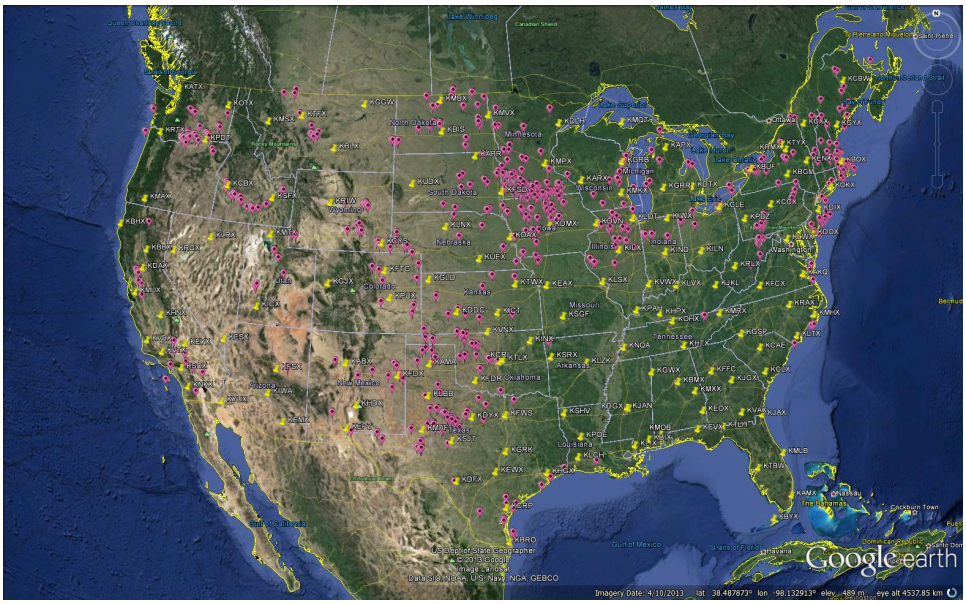

Figure 1.16: Wind farms (Magenta balloons) and NEXRAD weather radar (yellow pins) in contiguous US. The wind farm locations are provided by OPENEI.

turbines are also excluded. Out of 740 such wind farms studied, 417 of them have at least one NEXRAD radar nearby within 100 km of range, which is approximately the maximum Doppler coverage of NEXRAD radars at high PRF. The histogram of these wind farms and their range to the closest NEXRAD radar is shown in Fig. 1.17.

Wind turbines installed too close to the radar can potentially saturate radar receivers due to significant amount of backscattered EM energy [19]. Diffractions caused by closely spaced wind turbines may result in shadowing effect in the wind farm proximity [20]. Even at ranges up to several tens of kilometers, these structures can still cause various forms of clutter effects that may degrade nearby radar performance. Unlike conventional ground clutter, which is essentially stationary from pulse to pulse, wind turbines produce complicated Micro-Doppler characteristics primarily due to the blade rotation. Thus, conventional ground clutter filtering techniques have failed to mitigate this type of interference.

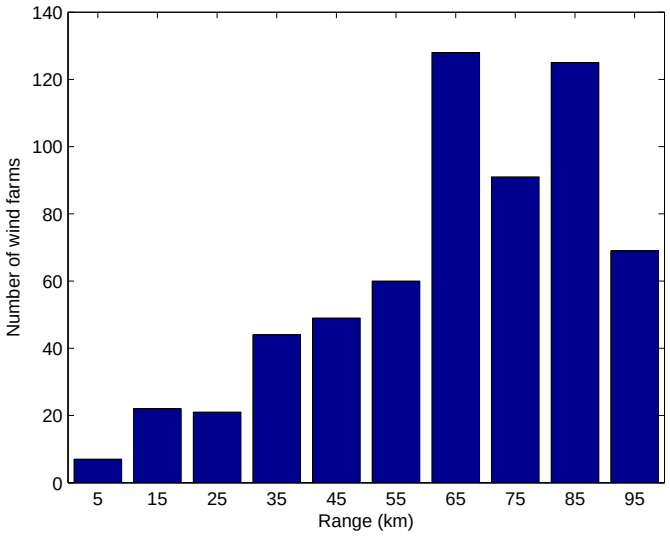

Figure 1.17: Histogram of the distance from wind farms to NEXRAD radar, distributed to uniformly spaced range bins of every 10 km. Only those within 100 km of a NEXRAD radar, whose total capacity is greater than 5 MW are counted.

Early investigations by researchers at the University of Michigan in the late 1970s revealed that large windmills have EM Interference (EMI) on television signals at VHF and UHF bands [21], which may affect wireless broadcasting and communication. However, it is not until the utility scale wind turbines began to thrive and the radar networks become so dense that these increasingly large man-made structures started to raise concerns in the radar community. As a result, the impact of large wind turbines on radars was not systematically studied until early 2000s by British scientists [22, 23].

As both the number and size of wind turbines increase dramatically in recent years, the potential impacts of wind turbines on radar performance has been gradually realized and the WTC, as a recently recognized new type of radar clutter, starts to attract more attentions from the radar community. In the US, the issue was first discussed in the Department of Defense (DOD) report [20] to the Congress regarding the effect of wind farms on military readiness, where the potential degradation of radar

performance was analyzed on long range defense radar, Air Surveillance Radar (ASR), Air Route Surveillance Radar (ARSR) and weather radar. The two-part paper [24,25] summarized the DOD sponsored wind turbine radar measurement campaign carried out by the Air Force Research Laboratory (AFRL), where spurious radar detection and tracking of aircraft caused by wind turbines were simulated to address potential impacts of wind turbines in the radar vicinity.

Due to the lack of awareness of this clutter, many of these wind farms were sited close to radars, whose performance may be affected. Most of the affected radars are weather radar due to the fact that the National Weather Service (NWS) does not have the legislative authority over wind farm siting, as compared to other federal bureaus such as the Federal Aviation Association (FAA) and DOD, who operate the ASR, ARSR and various military radar, which are also susceptible to WTC. In addition, as will be discussed in later chapters, it is more difficult to mitigate WTC from weather returns, as the weather activity may be inseparable from wind turbines in time spatial, time and frequency domains.

The negative impacts of wind turbines built in the vicinity of weather radar on storm detection and tracking have been discovered in early 2000s [26]. The first experimental campaign to study wind turbine weather radar signal characteristics was launched by the Radar Operations Center (ROC) [27, 28] in 2006. It has been found that weather radar observations of wind turbines have similar Micro-Doppler signatures to what discovered in early AFRL experiments [24, 25] . Several cases of wind farms built close to WSR-88D affecting radar operations have been reported [29–33]. The details of how wind turbines affect weather radar data quality in different modes and development of mitigation algorithms specifically for weather radar will be discussed in later chapters.

1.5 Motivation and Outline

At present, there is not a single solution that will mitigate the WTC, while keeping the desired target return signal unaffected. DOD, FAA and NWS, who operate most of the radar networks in US, have made dedicated efforts through Public Relation (PR) to raise the awareness on the impact of wind farms on nearby radars in the wind power community, hoping the wind power developers will take into account the potential impact to radars in the phase of siting. If necessary, regulations may be used against proposed wind farm sites in the radar LOS in order to maintain the performance of critical radars. Therefore, the lack of effective means to mitigate WTC on current radar networks has postponed installations of many wind farms, stalling the expansion of renewable energy development.

Wind turbine designers and manufacturers have been investigating stealth wind turbine technology, i.e., applying RCS reduction techniques in the designing phase to minimize the potential clutter return. In particular, near-specular reflection can be avoided by tapering the tower and nacelle [34, 35] as it is well established that RCS decreases significantly away from normal incidence. It is worth noting that this approach has little effect on modern radar with Doppler processing capability, as the return signal from the tower and nacelle can be mitigated by conventional ground clutter filtering techniques.

The shape of the blade, however, cannot be altered as it determines the aerodynamics of the wind turbine. Thus, there has been discussions about using Radar Absorbent Material (RAM) to conformally treat the blade [36, 37]. In fact, a prototype of stealth blade is reported to be fabricated by Vestas and tested by radar [38]. The return signal indeed drops for the stealth blade compared with the conventional blade; however, in the experiment, the decrease of peak RCS value of 6 dB was limited compared to the peak RCS of the original blade, which is over 35 dB^2. The cost

constraint for stealthy treatment of blades and its impact to wind power development is unknown.

For ARSR and ASR, the aircraft targets are normally higher than wind turbines, i.e., they can be distinguished in space. However, both types of radar have fan beams for fast volume coverage, which has wide beamwidth along elevation. Therefore, they have difficulties distinguishing wind turbine and aircraft returns even though they are spatially separated. The obvious solution is to use an antenna with narrower beamwidth in elevation, but this will slow down the volume coverage.

PAR utilizing electronic steering instead of mechanical steering can achieve fast update and narrow beamwidth simultaneously. Though the Multi-Function PAR (MPAR) has been proposed [39], upgrading all current radar networks to MPAR is a long-term project requiring a large amount of investment and time. Tilting the antenna to a slightly higher elevation angle is an intuitive solution to avoid wind turbines in the radar LOS. However, the radar coverage range at lower altitudes will be shortened, affecting the capability to detect long-range targets. Many use concurrent beam processing [40] alternating between a high beam and a low beam, to cover both the close and far range. Reduced sensitivity at lower elevations for the low beam is the major concern for this approach.

Other system upgrade solutions have also been proposed, including transmitting narrower pulses to increase range resolution, which will help in limiting WTC to only range cells they fall into [40]. Higher range resolution means wider bandwidth, which may raise problems in spectrum management. Furthermore, the benefit is extremely limited and will not relieve at all the clutter contamination at the wind turbine locations. For surveillance radar with tracking ability, the impact of wind farms on tracking has been studied [41] and several attempts have been made to recover the tracking performance. However, only the case that the aircraft and wind turbine are not in the same range cell was discussed, where the WTC impact is minimal.

Using a high resolution clutter map is also proposed to mark potentially contaminated range cells. However, the actually contaminated resolution volumes varies from scan to scan because of the reflectivity variations of wind turbine return signals. The propagation medium also varies with time. Therefore, the area with potential WTC contamination may include fairly large amount of range cells as compared to the actual number of range cells with a wind turbine in it. Nevertheless, the clutter map containing wind farms near the radar has been used in several NEXRAD radars to mark invalid data as a result of WTC contamination. Excluding erroneous estimates is important in reducing false alarms.

The gap-filler or in-fill radar concept [42] provides a potential solution to mitigate the wind turbine clutter impact on current operational radar networks. The idea is to deploy low-profile radars in/near the wind farm area to cover the clutter contaminated region caused by wind turbines. The data products of the gap-filler radar are then merged with the operational radar through a network. The principle concept is to avoid wind turbines in the LOS of the new radars, thus having a clutter-free view of the air space above the wind farm. However, there are several limitations: 1) the cost to install a gap-filler radar for every wind farm affecting radar operation can be tremendous, 2) to achieve the LOS avoidance, the new radar require to be installed on high ground, which is not always available, 3) the complexity of fusing the new radar data product with the operational radar is unforeseen and can be difficult since the new radar will be remote from operational radar and most likely to be at higher frequency due to its compact design, 4) LOS avoidance is to equivalent to filtering out the clutter spatially, which will be much easier to implement on PAR. In other words, upon upgrading current radar systems to phase array, these gapfiller concept will be meaningless.

Unlike air surveillance radar, the targets of interest for weather radar are various forms of precipitation, such as rain, snow, hail, etc., which are often spatially inseparable from wind turbines for low elevation scans. Spatial interpolation has been investigated [12] to patch the missing data by setting the exclusion zone using clutter map. Image processing techniques are also exploited to remove the Doppler flashes observed in the micro-Doppler signature of wind turbine spectrum [43], which eliminate useful signal at the same time. The difficulty in separating wind turbines and weather radar returns in both the spatial and Doppler domains has prompted ideas of combining information from both domains. Range-Doppler processing [44, 45] exploits the difference between wind turbine and weather radar return signals in the range-Doppler domain, alleviates Doppler spectral components identified as WTC, and reconstructs the weather signal based on the spatial continuity assumption.

In summary, none of the proposed mitigation schemes can completely solve the problem without raising up new issues. The lack of effective means to mitigate WTC is due to insufficient understanding about wind turbine radar signatures. Both EM simulations [46–53] and field measurements [22, 25, 28] have been carried out in efforts to characterize wind turbine radar signatures, and there have been challenge with both approaches. The major concern about simulations is its accuracy. Due to the large electric scale, a large amount of calculations have to be approximated and many scattering mechanisms are not taken into account in order to make computation tasks manageable. Reported results [24, 49, 50] are qualitatively comparable to actual measurements, but not accurate enough to provide quantitative match, which is the key to effective mitigations. The wind turbine, as a non-cooperative target, rotates and yaws according to wind conditions, whose control system is not easily accessible under normal circumstances. As a result, field measurements have difficulties in aligning measured data to instantaneous motions of the wind turbine.

The motivation of this work is to explore the interference from large commercial utility-scale wind turbines on nearby weather radars, characterize its radar signatures and mitigate the clutter effect. Following this introductory chapter, a more in-depth review about different aspects of pulse-Doppler weather radar is provided in Chapter 2. The unique micro-Doppler radar signature of wind turbine radar signal will be introduced in Chapter 3. Our EM characterization efforts will be detailed. Using NEXRAD radar data, various forms of impact of wind turbines on radar, the cause and how WTC contaminates radar data will be discussed. The deployment of mobile radar into wind farms and the data will also be analyzed in this chapter. Chapter 4 covers the scale measurement and related, such as the Radar Wind Turbine Testbed development, different measurement approaches, etc. The chapter ends with statistical characterization of wind turbine signal based on the scaled measurement. In Chapter 5, different mitigation approaches are discussed and compared. This dissertation ends with conclusions of the study and some important recommendation for future studies.

Chapter 2

Pulse Doppler Weather Radar

2.1 Pulse-Doppler Radar System

As the name suggests, a Pulse-Doppler radar is a radar that transmits a pulse for ranging and makes use of the Doppler effect to obtain moving information of the target, i.e., the radial velocity. A pulse Doppler radar sends out an amplitude modulated signal at the carrier frequency ω_0:

$$x_t(t) = p(t)cos(\omega_0 t) \tag{2.1}$$

where $p(t)$ is the baseband modulation signal with a pulse shape. For an ideal pulse signal, $p(t)$ has the following form:

$$p(t) = \begin{cases} 1 & 0 \leq t < T \\ 0 & else \end{cases} \tag{2.2}$$

As is discussed before, this pulse excitation is applied to the environment being observed by the radar, which can be assumed as a linear system with range/time profile $H(t)$. Therefore, the amplitude of the received signal is the pulse response of the system:

$$A(t) = H(t) * p(t) = \int_{t-T}^{t} H(\tau)d\tau \tag{2.3}$$

which is the integration of $H(t)$ within the pulse width. By gating at different time delays, the amplitude at the gate t_d is:

$$A(t_d) = \int_{t_d-T}^{t_d} H(\tau)d\tau \tag{2.4}$$

Conventional radar without Doppler processing relies on this amplitude return to detect the target. In this case, the transmit phase can be free-running. Therefore,

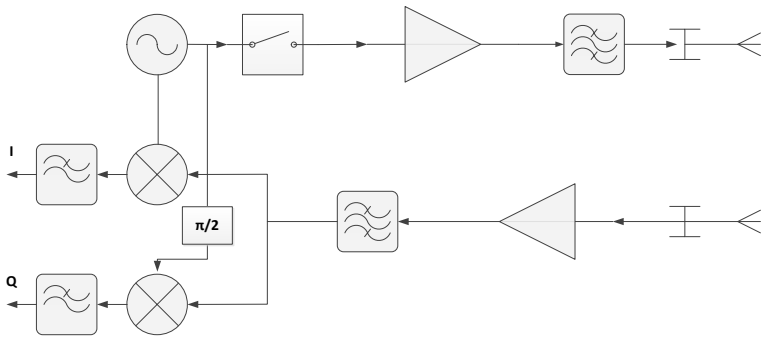

Figure 2.1: The block diagram of a pulse Doppler radar. Direct-conversion architecture is used in the receiver. Notice the local oscillator input of the down-convert mixer needs to be phase-coherent with the transmit oscillator.

the phase difference of the received signal from pulse to pulse can be caused by the frequency drifting of the transmitter itself. However, if the transmit phase can be kept stable for a few number of pulses, the phase change in the received signal will be solely due to the Doppler frequency shift caused by moving target. The returned signal from a moving target with Doppler frequency ω_d is:

$$x_r(t) = A(t_d)cos\left[(\omega_0 + \omega_d)(t - t_d)\right] \tag{2.5}$$

In order to extract the phase from the return signal, which contains Doppler information, the quadrature receiver demodulation is usually deployed as shown in the block diagram of Fig. 2.1. The same signal used for pulsing is used as the LO input of the demodulator. It was directly fed to one demodulator, however, delayed by $\pi/2$ for the other demodulator. The received signal, therefore, is projected onto the orthogonal pair of $\cos(\omega_0 t)$ and $-\sin(\omega_0 t)$:

$$\cos\left[(\omega_0 + \omega_d)(t - t_d)\right]\cos(\omega_0 t) = \frac{1}{2}\cos\left[(\omega_0 + \omega_d)(t - t_d) + \omega_0 t\right] + \frac{1}{2}\cos\left[(\omega_0 + \omega_d)(t - t_d) + \omega_0 t\right] \tag{2.6}$$

$$-\cos\left[(\omega_0 + \omega_d)(t - t_d)\right]\sin(\omega_0 t) = -\frac{1}{2}\sin\left[(\omega_0 + \omega_d)(t - t_d) + \omega_0 t\right] + \frac{1}{2}\sin\left[(\omega_0 + \omega_d)(t - t_d) + \omega_0 t)\right] \tag{2.7}$$

where the first term of each is the sum-frequency component and is filtered by the following low pass filter. The second term is the baseband IQ signal:

$$x_i(t) = \frac{1}{2} cos(\omega_d t + \phi_0) \tag{2.8}$$

$$x_q(t) = \frac{1}{2} \sin(\omega_d t + \phi_0) \tag{2.9}$$

where ϕ_0 is the constant phase term. The analytical signal $x_i(t) + jx_q(t)$ therefore has a Doppler frequency shift at ω_d, which can be estimated by various methods [6].

2.2 Wave Propagation in the Atmosphere

2.2.1 Refractivity

In free space, electromagnetic waves travel in a straight line at the speed of light:

$$c = (\mu_0 \varepsilon_0)^{-1/2} \tag{2.10}$$

where μ_0 and ε_0 are the free space permeability and permittivity constant, respectively. Through the atmosphere, however, the dielectric constant ε is higher than ε_0 and is vertically stratified. Therefore, the wave propagates slower than the speed of light along a curved path. Because the permeability in the air is almost the same as in free space, the wave propagation path is exclusively determined by the refractive index $n = c/v$ or the relative permittivity:

$$\varepsilon_r = \varepsilon/\varepsilon_0 = n^2 \tag{2.11}$$

where ε_r is near-unit for the air. Thus, the relative refractive index is also a near unit value. It is therefore, convenient to use a different measure for the refractive properties of the air. The refractivity [54] is defined as:

$$N = (n - 1) \times 10^6 \tag{2.12}$$

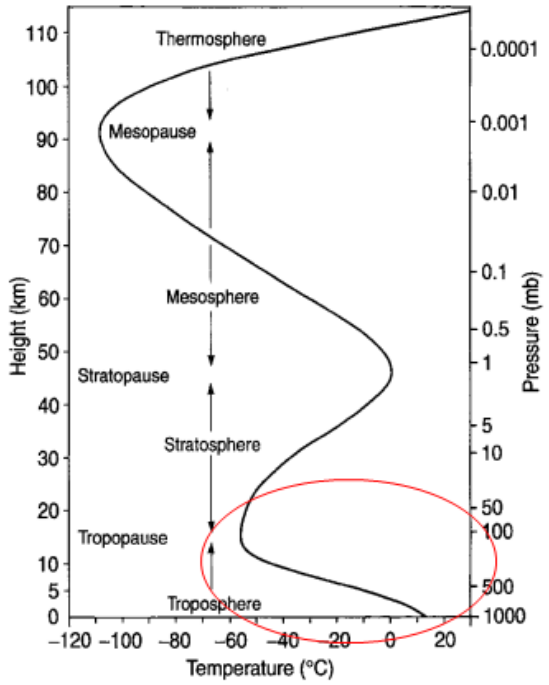

Figure 2.2: The stratified Earth atmosphere. The curve shows the dependence of the air temperature and pressure on altitude. The troposphere is circled in red, where most weather activities that weather radar observes occur.

For air with water content, the refractivity can be calculated using the following equation [54]:

$$N = (77.6/T)(P + 4810P_w/T) \tag{2.13}$$

where T is temperature in Kelvins, P is the total air pressure in millibars and P_w is the partial water pressure.

The Earth's atmosphere is stratified. Within the troposphere, where the ground base weather radar wave propagates and has most returns from, both the temperature and pressure normally decreases as the altitude increases as shown in Fig. 2.2 , up to approximately 10 km above the sea level, which is the top of the troposphere. In equation (2.13), the fractional decrease of pressure usually is greater than that of temperature, thus, the refractivity N will decrease with altitude.

2.2.2 Equivalent Earth Model

In the stratified atmosphere, EM waves travels along a curve instead of a straight line. Due to the fact that the Earth surface is near spherical, the radar beam usually is progressively higher above the ground as shown in Fig. 2.3. In radar observations, the ray path r can be measured by converting the time delay to range as in Fig. 2.3 (a). However, for a given elevation tilt θ_e, the arc distance s and beam height h are needed to precisely locate the radar return in the Earth coordinate. In fact, they can be rigorously solved if the refractivity variation over altitude is known. In the homogeneous atmosphere, where the ray path is straight, if the height of the straight line at distant s is the same as the actual curve in stratified atmosphere at the same distance, then this equivalent Earth model can simplify the relation of the aforementioned parameter pairs (r, θ) and (s, h). Furthermore, it is reasonable to assume a constant refractivity gradient dn/dh for the lower atmosphere, then this complicated geometry relation can be approximated in the following simple forms:

$$h = [r^2 + (a_e)^2 + 2ra_e sin\theta_e]^{1/2} - a_e \tag{2.14}$$

$$s = a_e sin^{-1}\left(\frac{rcos\theta_e}{a_e + h}\right) \tag{2.15}$$

where a_e is the equivalent Earth radius:

$$a_e = \frac{a}{1 + a(dn/dh)} \tag{2.16}$$

where a is the Earth radius (6371 km). It has found that the gradient of n in the first kilometer or two is typically $-1/(4a)$ ($dN/dh = -39$), or $a_e = 4/3a$, which is referred to as the 4/3 equivalent Earth model [54].

It is worth noting that the 4/3 equivalent Earth model is only accurate for the lower atmosphere where $dh/ds \ll 1$. For higher elevation, the refractive index will converge to unity. However, this model is widely adopted in weather radar for all θ_e, as the error caused by the model is smaller compared to the vertical resolution of the radar at far ranges.

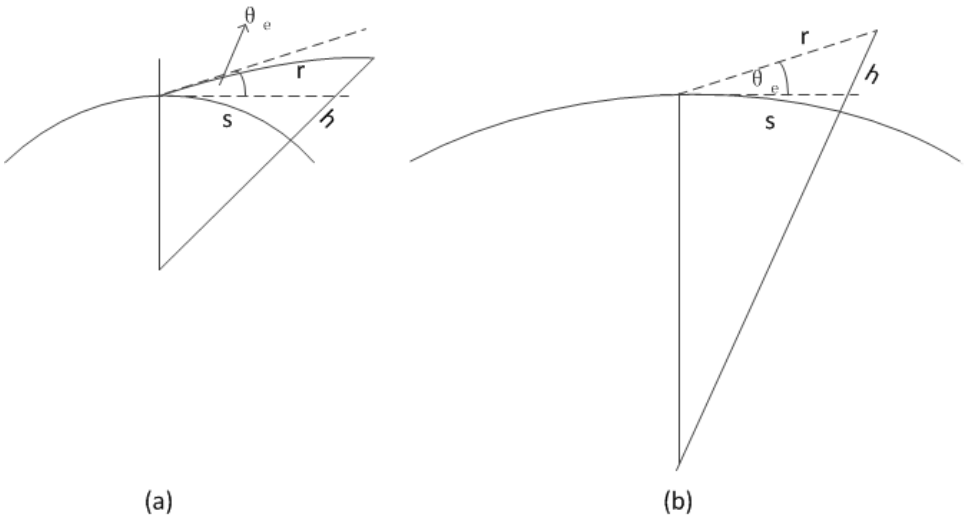

Figure 2.3: Demonstration of the equivalent Earth model: (a) curved propagation path in the stratified atmosphere, (b) straight ray path in the equivalent Earth model. The elevation angles of the two are the same.

2.2.3 Anomalous Propagation

The radar beam travels in a curve in the stratified atmosphere, which may be bent toward the Earth surface if there is irregular refractivity decrease. This wave propagation phenomenon in the lower atmosphere is called Anomalous Propagation (AP), which is usually caused by the temperature inversion. An inversion refers to the forming of a thin layer of the atmosphere near surface, where the temperature starts to increase with altitude, which causes the refractivity to drop significantly faster than it normally does. The ducting of the wave toward the ground may cause severe ground clutter contamination, where the clutter may not be visible in the standard propagation. Clutter may even be found where there are no clutter objects due to the wrongfully estimated range caused by the inversion.

The inversion often occurs at night when the surface cools with warm air aloft, which will disappear gradually after sunrise. It also occurs ahead of a warm front, where a warm airmass overrides a cooler one [55]. If the inversion layer is relatively

high, the radar observation range will be extended, where objects at longer distance usually not visible under normal circumstance become visible. Though the range measured will be wrong if the standard atmosphere model is still assumed. In the case where the inversion layer is shallow, the radar wave may be trapped in this layer and is reflected more than once to create multi-path spurious images of actual objects at multiple ranges. In both of these cases, the inversion results erroneous range if the 4/3 equivalent Earth model is used to estimate s and h from measurements.

2.3 Weather Radar Equation

The radar equation in equation (1.15) assumes a point target. Distributed targets such as those from weather phenomenon are composed of many small point targets, i.e., precipitation particles, which can be described individually by the Radar Equation. The RCS of each particle is determined mostly by its diameter as it is in the Rayleigh scattering region. The drop size distribution $N(D)$ characterizes the probability of occurrence of precipitation particles with diameter of D. The reflectivity, which is the the equivalent RCS in a unit volume is thus defined as:

$$\eta = \int_0^\infty \sigma(D)N(D)dD \tag{2.17}$$

where $\sigma(D)$ is the RCS of precipitation particle with diameter D. The expected return power from such a unit volume dV is:

$$E[dP] = I(r_0, r)dV\eta(r) \tag{2.18}$$

where $I(r_0, r)$ includes other terms in the radar equation that vary spatially:

$$I(r_0, r) = C\frac{f^4(\theta - \theta_0, \phi - \phi_0)|W_s(r_0, r)|^2}{l^2(r)r^4} \tag{2.19}$$

$$C = P_t G^2 \lambda^2/(4\pi)^3 \tag{2.20}$$

The expected return power from the resolution volume centered at (r_0, ϕ_0, θ_0) is the integration of $E[dP]$ over the entire space, which is actually confined by the antenna pattern $f(\theta, \phi)$ and the transmit waveform $W_s(r_0, r)$:

$$\overline{P}(r_0) = \int_0^{\infty} \int_0^{\pi} \int_0^{2\pi} \eta(r) I(r_0, r) r^2 dr \sin\theta d\theta d\phi \tag{2.21}$$

For weather radar, the antenna pattern is usually Gaussian and $W_s(r)$ is determined by the pulse width τ. The integration can therefore be solved and simplified [54] as:

$$\overline{P}(r_0) = \frac{P_t G^2 \eta c \tau \pi \theta_1^2 \lambda^2}{(4\pi)^3 r_0^2 l(r_0)^2 16 \ln 2} \tag{2.22}$$

where θ_1 is the 3 dB beam width. The received signal power is inversely proportional to the square, instead of the 4^{th} power of the range, which is the major difference between the weather radar equation and the radar equation. By comparing equation (2.22) with the radar equation (1.15), the following conversion from reflectivity to RCS can be obtained:

$$\sigma = \frac{\eta r_0^2 c \tau \pi \theta_1^2}{16 \ln 2} \tag{2.23}$$

2.4 Weather Radar Signal Processing

Due to the random motion of precipitation particles within the resolution volume, the return signal of weather radar is a random process. It can further be proved that both the In-phase (I) and Quadrature (Q) outputs of the radar receiver are Gaussian distributed [54]. This complex random process needs to be processed to statistic parameters which are meaningful to meteorologists.

The Power Spectrum Density (PSD), or simply referred to as the Doppler spectrum, is the power-weighted distribution of radial velocities of the precipitation scatterers within the resolution volume [54], which is defined as the Fourier transform of the Auto Correlation Function of the IQ signal:

$$S(f) = \lim_{M \to \infty} \sum_{l=-(M-1)}^{M-1} R(l) e^{-j2\pi f T_p l} \tag{2.24}$$

where T_p is PRT. l is the delay lag of the ACF $R(l)$, which is defined as:

$$R(l) = E\left\{x^*(m)x(m+l)\right\} \tag{2.25}$$

where $x(n)$ is the IQ time series. In reality, only a few samples can be acquired for each azimuth dwell, therefore, the following estimation for ACF is usually used:

$$\widehat{R}(l) = \frac{1}{M}\sum_{m=0}^{M-|l|-1} x^*(m)x(m+l) \tag{2.26}$$

where M is the number of samples. Using the Fourier transform of the ACF estimate above for PSD is called the correlogram estimation of the Doppler spectrum:

$$\widehat{S}(f) = \sum_{m=0}^{M-1} x(m)\widehat{R}(l)e^{-j2\pi f T_p l} \tag{2.27}$$

The Doppler spectrum can also be estimated using the periodogram method:

$$\widehat{S}(f) = \left(\sum_{m=0}^{M-1} x(m)e^{-j2\pi f T_p m}\right)^2 \tag{2.28}$$

And these two methods can be proved to be equivalent [6].

The Doppler spectrum of the weather return signal typically follows a Gaussian shape because the random motions of the precipitation particles are Gaussian distributed. An example of the spectrum of weather return and the Gaussian spectrum, whose moments are estimated from the signal, is shown in Fig. 2.4. Notice the Abscissa has been switched to the radial velocity v, which can be linearly converted from the Doppler frequency. The three moments of the radial velocity therefore are defined as the following:

$$P = \int_{-v_a}^{v_a} S(v_r)dv_r \tag{2.29}$$

$$\overline{v_r} = \frac{1}{P}\int_{-v_a}^{v_a} v_r S(v_r)dv_r \tag{2.30}$$

$$\sigma_v = \frac{1}{P}\int_{-v_a}^{v_a} (v_r - \overline{v_r})S(v_r)dv_r \tag{2.31}$$

where the power P is the 0^{th} order, $\overline{v_r}$ is the 1^{st} moment about zero and σ_v is the 1^{st} moment about the mean. The estimates of these moments can be obtained by similar

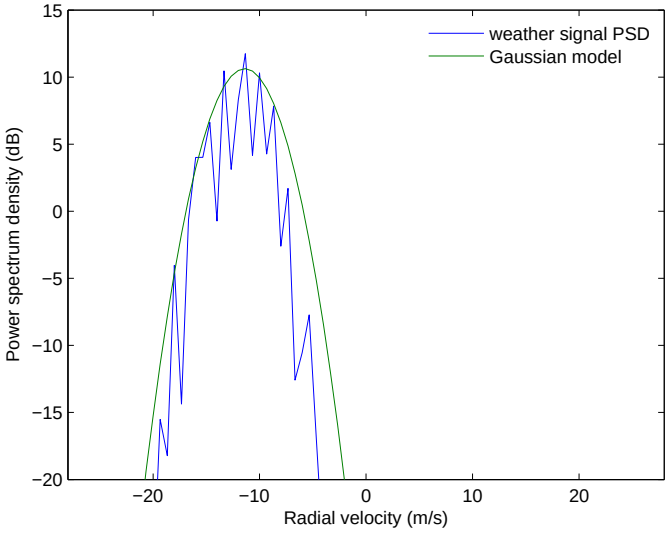

Figure 2.4: Typical Doppler spectrum of the weather return and the Gaussian-model approximation. The Gaussian-model spectrum is constructed using covariance moment estimates.

spectrum processing from the above definitions, which would require first estimating the Doppler spectrum [56]. In reality, to meet the real-time processing requirement, the covariance method using only a few lags of the ACF is often used. Based on the algebraic properties of the Fourier transform:

$$P = \widehat{R}(0) \tag{2.32}$$

$$\overline{v_r} = \frac{\lambda}{4\pi T_p} \angle \widehat{R}(1) \tag{2.33}$$

$$\sigma_v = \frac{\lambda}{2\pi T_p \sqrt{(2)}} |\ln\left(\frac{P}{|\widehat{R}(1)|}\right)|^{\frac{1}{2}} \tag{2.34}$$

where only $\widehat{R}(0)$ and $\widehat{R}(1)$ need to be estimated. The covariance processing is computationally efficient and straightforward, which will be used throughout our study.

Table 2.1: System specifications of the WSR-88D radar

Frequency	2700-2900 MHz
Peak power	750 kW
Beam width	1°
Gain	44.5 dB
First sidelobe	26 dB
Polarization	Dual polarized
Pulse width	1.57-4.57 μs
PRF	320-1300 Hz

2.5 The NEXRAD Weather Radar

The NEXRAD is a network of 160 high-resolution S-band Doppler weather radars. The network is operated by NWS, a joint agency of the National Oceanic and Atmospheric Administration (NOAA) within the United States Department of Commerce, FAA within the Department of Transportation and the US Air Force within DOD. The common name of the radar is WSR-88D, which was developed in the late 80s last century to replace the legacy non-Doppler weather radar WSR-74 and WSR-57.

The WSR-88D is a pulse-Doppler radar and some of the system specifications are listed in Table 2.1. The elevation angles are not given in the table. In normal operational mode, the radar antenna rotates continuously from bottom to top at each predetermined elevation angle. Different scan mode has different elevation angle set, rotation rate, pulse width and PRF, often referred to as the Volume Coverage Pattern (VCP), which is deployed in different weather conditions. The radar operators can select proper VCP based on the weather being observed.

There are, basically, two major scan modes: clear air and precipitation. The clear air mode includes VCP31 and VCP32, where the latter will be frequently mentioned in many case studies throughout this study. In VCP32 mode, the radar rotates slowly 4° to 5° per second for increased sensitivity to perceive clear air objects. Only 5 low elevation angles are covered: 0.5° , 1.5° , 2.5° , 3.5° and 4.5°. A short pulse is applied so the range resolution is relatively high. The PRF is 322 Hz for 0.5° and 1.5° , 446 Hz for higher elevations. The low PRF is selected for increased unambiguous range coverage as the Doppler information is not that important in clear air surveillance.

The precipitation mode is further divided into shallow precipitation mode known as VCP21 and convection mode, which includes VCP 11, 12, 121, 211, 212 and 221. More elevation angle choices are provided in these modes. The lowest elevation angle, however, is 0.5° for all VCPs. The scanning rate of the radar increases in precipitation modes as the data update rate speeds up. A longer pulse has higher sensitivity but lower range resolution. Higher PRF means higher Doppler aliasing velocity but shorter unambiguous range. Similarly, a quicker update speed means lower sensitivity and less elevation coverage. In summary, different VCPs are constructed to meet some of the needs, but will compromise in other areas.

It is worth noting that the WSR-88D can also be configured to spotlight mode, which is important in this study. In this mode, the radar antenna stops scanning, and dwells on a fixed azimuth and elevation direction to collect data for a relatively longer period of time. This allows the radar to dwell on a specific target for much longer instead of revisiting the same target only every several minutes. This is critical for observing continuously moving targets such as a wind turbine.

2.6 Clutter Filter in Weather Radar

A ground clutter filter is usually a high pass filter, which blocks the frequency response from ground clutter. Because most types of ground clutter are stationary or at very

low speed, the corresponding Doppler frequency is usually low compared to moving targets. Hence, a well designed high pass filter can attenuate a strong clutter return, and preserve the desired target signal at the same time. Filter design is too broad a topic to be discussed here, however, a brief overview of the clutter filter GMAP (Gaussian Model Adaptive Processing), which is deployed in the signal processor of the NEXRAD radar, will be provided.

GMAP is an adaptive filtering technique developed by Vaisala [11]. It is based on spectrum processing, therefore the Doppler spectrum needs to be estimated first. Compared with classic FIR and IIR filters, GMAP adapts the stop band with different PRF and number of points configurations. Thus, minimal operator intervention is required. If there is no clutter present, GMAP has little impact on the spectrum. GMAP makes a few assumptions on the weather and clutter spectrum characteristics:

- The spectrum width of the weather signal is greater than that of the clutter.
- The Doppler spectrum consists of ground clutter, a single-peak weather spectrum and noise. The filter is not valid for the multi-peak weather spectrum, which may occur in some rare cases.
- The width of the clutter is approximately known, which is mainly determined by the radar scan speed.
- The weather spectrum can be well approximated by the Gaussian model.

The first step for any spectrum-based processing is to accurately estimate the Doppler spectrum. A Hamming window followed by DFT is implemented for the first trial. The noise level is then estimated from the spectrum, which can be done using the Hilderband approach [57]. Using the central three points of the spectrum to fit a Gaussian curve having the heuristically assigned spectrum width, the points within the intersections of the Gaussian spectrum and the noise level will be discarded. The remaining points above the noise level are used to fit a Gaussian curve as an

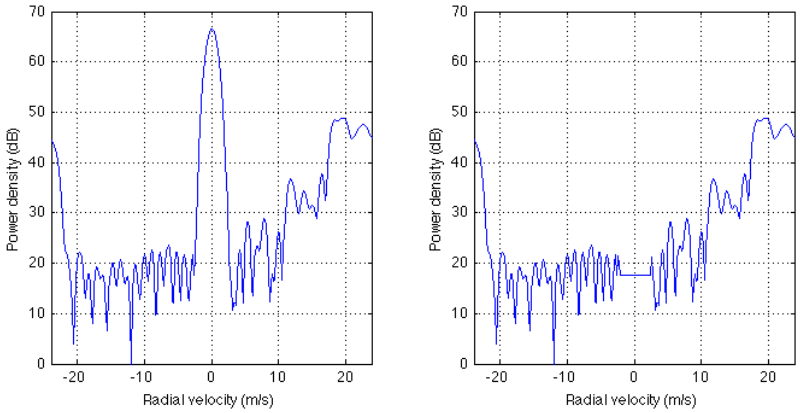

Figure 2.5: An example of applying the GMAP filtering on weather signal contaminated by ground clutter. The left shows the Doppler spectrum estimate of the ground clutter contaminated weather signal. Hamming window has been applied for spectrum estimate. The spectrum after filtering is shown on the right. For simplicity, the discarded points are replaced by linear interpolation instead of Gaussian fitting.

approximation for the weather spectrum. The previously discarded points are then filled by these fitted values. The Clutter to Signal Ratio (CSR) is then estimated. If the CSR is too high, this process is repeated with a more aggressive window such as the Blackman window. If the CSR is too low, a rectangular window is used for better spectrum resolution.

A showcase of the GMAP filtering is given in Fig. 2.5, where the weather spectrum is slightly aliased to the other side of the spectrum. The spectrum of the weather is indeed much wider than that of the ground clutter. Only the ground clutter and weather spectrum are present in the example given. Before filtering, the clutter power is dominant and it is difficult to detect the weather signal without spectrum processing. After the filtering, however, the clutter spectrum is around noise level and the weather spectrum can be effectively recovered.

Chapter 3

Radar Observations of Wind Turbines

3.1 Micro-Doppler Signature of WTC Signal

The blade rotation of a wind turbine is oscillatory micro motion with respect to the entire wind turbine structure. This type of motion may cause extremely complicated Doppler modulations [58]. Various parts of the blade move at different speed and in both radial directions, i.e., toward and away from the radar. The Doppler spectrum of targets with micro motions is usually time-variant. Therefore, the micro-Doppler signature of wind turbine radar return signal is best perceived by continuous radar observation, i.e., the spotlight mode.

Fig. 3.1 shows the time-variant Doppler spectrum (spectrogram) of WTC, where each vertical line is Doppler spectrum estimated from the raw IQ signal for a short time period. Obviously, the spectrum changes from time to time. There are some spectra, the density of which are much higher than others especially at higher frequencies. This feature is referred to as the Doppler flashes. These flashes also appear to follow some periodic pattern. This periodicity must be related to the blade rotation, which has a period of 120° assuming the three blades are identical. Therefore, there are certain rotation phase when these Doppler flashes occur.

For the time span of a few seconds as in Fig. 3.1, the rotation speed of the rotor blade can be considered constant. The period of flashes can thus be linearly converted to rotation phase by multiplying the rotation rate. Furthermore, if the initial phase of the rotation is known, each spectrum line can be mapped to the actual blade position. Hence, the blade position corresponding to the flashes can be located. However,

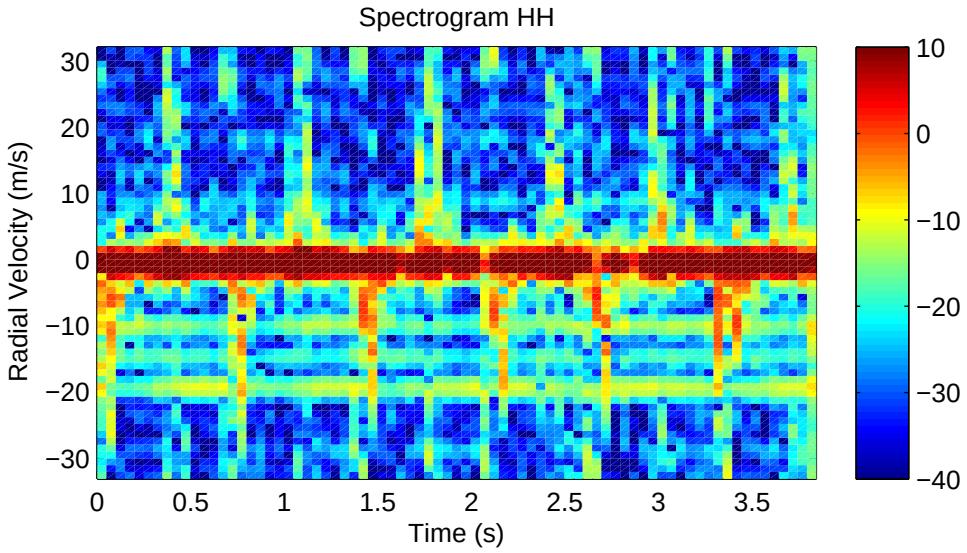

Figure 3.1: Spectrogram of WTC: the data is from the campaign led by ROC at the KDDC NEXRAD radar. The radar was configured in spotlight mode focusing on a wind farm approximately 40 km away.

neither the rotation rate nor the initial phase is known in this measurement. Thus, this Micro-Doppler signature cannot be mapped to the actual blade position of the wind turbine without synchronizing radar data acquisition with the instantaneous blade position. This issue will be further addressed in the next chapter.

The Doppler flashes are single sided. The velocity signs of the flashes alternate as the blade rotates. In Fig. 3.1, the flashes with negative radial velocities (moving toward the radar) are stronger than the ones on the other side. The PRF of the radar is 1282 Hz, which is already the fastest option of NEXRAD system. The corresponding aliasing velocity is approximately 33 ms^{-1}. The wind turbines being observed have a nominal rotation speed of $\omega = 28.5rpm$ and rotor diameter $D = 47m$. The tip speed thus is $\omega D/2$=70 ms^{-1}. Therefore, it is possible for the spectrum to be aliased. As a matter of fact, the Doppler flashes appear to be aliased in Fig. 3.1.

In addition to the vertical spectrum lines, there are a few horizontal lines in Fig. 3.1, too. These originate from single-tone signal components. At the zero frequency, the extremely strong line corresponds to relatively stationary parts of the wind turbine, i.e., the tower and nacelle. They can be considered as stationary in a few second time span. Because the spectrum density is significantly higher than the noise level, the other horizontal lines could be due to the sidelobe leakage in estimating the spectrum. However, the lines in Fig. 3.1 only appear on the negative side of the spectrum. Therefore, they are not from sidelobe leakage, which is supposed to be symmetric. They are, in fact, the result of radar receiver saturation, which will be discussed in later sections.

3.2 EM Characterization of the Wind Turbine

3.2.1 Challenges in Wind Turbine EM Characterization

The EM characterization of wind turbine is critical in understanding its interaction with radar. Predicting the back scattered electric field from the wind turbine is a common approach for EM characterization. The field intensity is proportional to the RCS in case of far field target. Furthermore, RCS prediction of the wind turbine is usually the very first step to evaluate potential impact of a proposed wind farm to nearby radars. However, it is extremely difficult to correctly predict the RCS of a wind turbine in a wind farm even for an approximate value. The challenges of calculating the wind turbine RCS are summarized as follows:

1. Utility-scale wind turbines are electrical large.

2. Wind turbine is dynamic.

3. The design of wind turbine is proprietary.

4. Multi-path scattering may have to be considered.

5. Wind turbine is in the radar near field.

Most commercial EM solvers mesh the target surface into small triangles/polygons, the minimum edge of which are required to be shorter than radar wavelength, normally from 1/12 to 1/6 of wavelength. For example, the wavelength of NEXRAD radar is approximately 11 cm, the meshing requirement thus is 1-2 cm, which means millions of such elements for a normal utility-scale wind turbine. The meshing process is extremely computationally intensive, making the calculation practically impossible on regular computers.

For radar observation, the characteristic that exclusively distinguishes the wind turbine from other large ground clutter such as buildings, mountains, etc. is its complicated motions. Most obviously, the blades rotate around the rotation axis. The rotor blade typically spins clockwise when viewed from upwind. The thick edge of each blade leads the way, thus is called the leading edge. The thinner one is the trailing edge. Throughout this study, the blade position θ is used to represent rotation phase. θ is defined as the angle from the yaw axis to a reference leading edge, as shown in Fig. 3.2. Though the blade rotation is only passively driven by the wind flow, its rotation rate needs to be controlled in a range. Therefore, each blade can be actively feathered to change the angle of attack β in order to adapt to the wind speed, which is often referred to as the pitch mechanism.

Another major motion of the wind turbine is yaw. When wind direction changes, the nacelle together with the hub and blade, rotate around the yaw axis to keep the blade rotation plane perpendicular to the wind direction for maximum efficiency. The yawing of wind turbine changes the azimuth aspect angle ϕ of the rotation axis with respect to the radar LOS as shown in Fig. 3.2. Calculating the RCS for all possible combination of $\sigma(\theta, \phi, \beta)$ for such a large target will be extremely difficult even for super computers. The blades may also vibrate due to gusty wind force. Therefore,

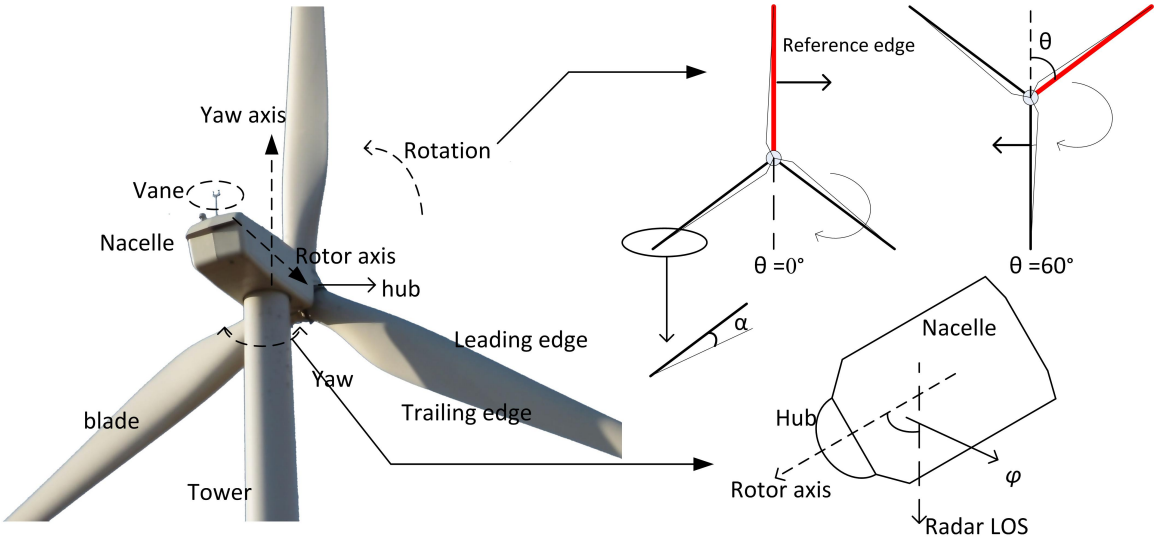

Figure 3.2: Wind turbine motions: the blade position $\theta(0° \leq \theta < 360°)$ is the angle swept by the reference leading edge from the upper vertical position. The aspect angle $\phi(0° \leq \phi < 360°)$ is the angle from the radar LOS to the rotor axis. α is the blade angle formed by the leading edge and trailing edge of the same blade.

it is practically impossible to deterministically calculate the RCS of an acutual wind turbine in the wind farm.

Electrical large targets are in the optical scattering region, where the RCS is mostly determined by target shape. The shape of the rotor blade is solely determined by the airfoil, i.e., cross section of the blade. However, as the airfoil design is proprietary, it is difficult to obtain the 3-D model, which is needed for the meshing at the first place. Even if the model becomes accessible, as the design varies from one to another, getting the RCS for all wind turbine models in the market and keep updating with new products is a tremendous work. In addition, the blades are made of composite material, which is also proprietary and varies from one manufacturer to another. Some may use fibre-glass enhanced plastic, some may be made of carbon-fiber. Different material may have significant impact on the RCS.

There are several multi-path scattering possibilities in and around a wind farm: between wind turbines, from/to the ground, and from/to nearby scattering objects, such as buildings, mountains, etc. Depending on the specific terrain and wind turbine alignment in the farm, the contribution of these multi-path scattering may be significant. Taking these into account means tremendous computation, as not only the back scattered field, but also the bistatic scattering field needs to be calculated.

The definition of RCS assumes infinite range from the radar [59]:

$$\sigma = 4\pi \lim_{r\to\infty} r^2 \frac{|E_s|^2}{|E_i|^2} \tag{3.1}$$

where E_i is the incident field amplitude at the target and E_s is the scattered field amplitude at the radar receiver. Generally, the RCS calculation is made in the far field:

$$r > R_{ff} = \frac{pL^2}{\lambda} \tag{3.2}$$

where R_{ff} is referred to as the far field range, L is the longest dimension of both the antenna and the target. p determines the largest phase variations of incident/scattered spherical wave over the entire radar target/antenna. $p = 2$ results in a $\pi/8$ maximum phase variation, which is usually acceptable for RCS characterization [60, 61]. For example,the GE-1.6M-82.5 wind turbine has a tower and blade combined length of approximately 120 m, then R_{ff}=262 km for NEXRAD radar. In reality, most wind farms with lasting impact on nearby radar are within 50 km of the radar, thus in the near field.

Therefore, even for a single wind turbine, the RCS is a function of many parameters in the form of $\sigma(\lambda, r, \theta, \phi, \beta, \varepsilon, \cdots)$, where ε is the effective dielectric constant of the composite blade material. In order to simplify the calculation, the following assumptions are made:

1. The blade material is Perfect Electric Conductor (PEC)

2. The rotor blade is in the far field.

The RCS will be overestimated by assuming PEC blade, which gives the worst-case evaluation of the impact. The tower is stationary, whose return signal can be mitigated by conventional ground clutter filter. Therefore it makes sense to only consider the rotor blade when calculating the far field range. The longest dimension of the rotor blades is from one tip to another $L = 0.85D$, where D is the rotor diameter. For the GE-1.6M-82.5 wind turbine, R_{ff}=89 km, which is significantly closer than the one calculated using the combined length of the tower and blade. However, it is still in the near field. So it is further assumed that the maximum distance between major scattering centers on the blade contributing to the RCS is short enough that the blades are effectively in the far field. The scattering center concept will be introduced next. The assumption can be validated by Doppler spectrum observations in our studies.

3.2.2 Scattering Centers

In radar cross section theory, it is well known that the EM field scattered from an electrical large target can often be modeled as if it is emanating from a discrete set of points, namely the scattering centers. They conceptually represent the scattering mechanisms contributing most to the target RCS. In the optical region, scattering centers are closely related to target geometry and are often found where geometric discontinuity occurs, which is usually identified with a mathematical discontinuity in the $Stratton - Chu$ radiation integral [62].

The concept of scattering centers much simplifies the computation of RCS for complicated radar target, as they can be divided into typical geometries with known analytical solutions or approximations, such as polygon, sphere, cylinder, etc. The RCS of the radar target is the square of the following coherently combined complex scattering amplitude:

$$\sqrt{\sigma}e^{j\phi} = \sum_{n=1}^{N} \sqrt{\sigma}_n e^{j\phi_n} \tag{3.3}$$

where $\sqrt{\sigma}_n e^{j\phi_n}$ is the complex scattering amplitude of the nth scattering center, with normalized incident amplitude. N is the number of significant scattering centers. The target RCS therefore is:

$$\sigma = \left| \sum_{n=1}^{N} \sqrt{\sigma}_n e^{j\phi_n} \right|^2 \tag{3.4}$$

and the scattering phase is:

$$\phi = tan^{-1} \left\{ \frac{\sum_{n=1}^{N} \sqrt{\sigma}_n \sin\phi_n}{\sum_{n=1}^{N} \sqrt{\sigma}_n \cos\phi_n} \right\} \tag{3.5}$$

Therefore, by treating only a small number of N, the target RCS can be solved. This simplification makes the computation relying only on the number of such significant scattering centers and their scattering characteristics. Compared with the commonly used meshing treatment, this reduces the computation task tremendously, making it possible to solve the RCS of electrical large target fast.

Two major scattering mechanisms resulting in most scattering centers are specular reflection and edge diffraction. For back scattering in a monostatic radar, reflection occurs when a smooth surface is illuminated from normal direction. The radius of surface curvature needs to be larger than wavelength. For this type of scattering center, depending on the radius, Physical Optics (PO) or Geometrical Optics (GO) are often good approximation to its analytical solution in the optical region. If both the meridional and zonal radius of the curved surface are infinite, such as the plane, the RCS is inversely proportional to the square of wavelength:

$$\sigma \propto \frac{1}{\lambda^2} \tag{3.6}$$

If only one of them is infinite, such as revolved bodies like cone and cylinder, the RCS is found to be inversely proportional to the wavelength:

$$\sigma \propto \frac{1}{\lambda} \tag{3.7}$$

Sphere and ellipsoid have finite radius in both dimensions, their RCS does not vary with wavelength. It is worth noting that scattering centers from reflection are significant only near specular incident.

The edges corresponding to geometric discontinuities result another type of scattering mechanism called diffraction. Compared to the specular reflection, this type of scattering is usually significant for a wide range of viewing angles. The scattering center is usually located at the intersection of the incident plane and the edge. The Geometric Theory of Diffraction (GTD) provides close approximation for this type of scattering mechanism in the optical region. The RCS of such scattering center is found to be proportional to the wavelength:

$$\sigma \propto \lambda \tag{3.8}$$

The rotor blade of a wind turbine is a complex electrical large target in the optical region. A typical profile of the blade is shown in Fig. 3.3. Near the root, a relatively short section of cylinder provides rigid connection to the hub. The airfoil changes its shape and size from root to tip. The wider end of the airfoil corresponding to the leading edge has tapered radius of curvature as the airfoil progresses to the tip of the blade. The radius is normally larger than the radar wavelength. The radius along the blade is usually infinite. Both the root cylinder and the leading edge are suitable for PO approximation and their RCS is inversely proportional to the wavelength. The other end of the airfoil has discontinuous 1^{st} order derivative, forming the sharp trailing edge, which is typical structure that creates diffraction.

The sides of the blade have large radius of curvature, which contributes to the RCS only at near specular incident. The tip of the blade is a sharp edge and will

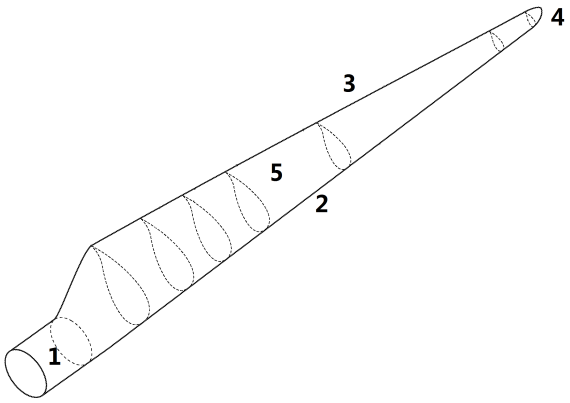

Figure 3.3: Airfoils of a typical wind turbine blade. Actual wind turbine blade has more sophisticated airfoil designs, which are proprietary to the manufacturers.

Table 3.1: Scattering mechanisms of a typical wind turbine blade

Number	**Parts**	**Scattering mechanisms**	**EM solution**
1	Rroot cylinder	Specular reflection	PO
2	Leading edge	Specular reflection	PO
3	Trailing edge	Diffraction & crawling wave	GTD
4	Tip	Diffraction	GTD
5	Surface	Specular reflection	PO

cause diffraction. The possible scattering mechanisms for different parts of the blade are summarized in Table 3.1. As the blade rotates, pitches and yaws, shading also needs to be taken into account when calculating the RCS. The phase of scattered field with respect to the reference phase at the rotation center can be obtained by projecting the corresponding ray path of each scattering center to the LOS.

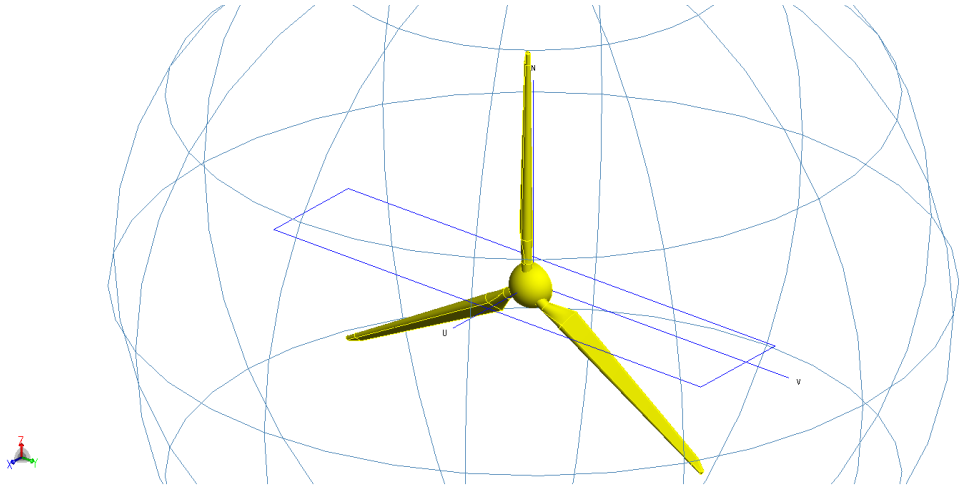

Figure 3.4: CAD model of the wind turbine blade including the hub. The rotation axis is along X-axis and the rotation plane is in the YZ plane. The yaw axis is the Z-axis. The rotor diameter is 78 m. The pitch is approximately 45°. The model has been provided through the courtsey of Ying Bai and Isaac Meier.

3.2.3 RCS of Rotor Blade

The rotor blade is the most important part of a wind turbine. The rotation results in scattering centers moving at different speeds with different directions. The amplitude and phase also change as the blade position θ increments. Though the azimuth aspect ϕ and pitch β may affect the scattering pattern significantly, they can be treated as constant each time the radar beam revisits the wind turbine. Therefore, the RCS variation is studied in terms of the blade rotation with fixed ϕ and β, i.e., $\sigma(\theta, \phi_0, \beta_0)$, or simply $\sigma(\theta)$. Without the knowledge of the airfoils of any particular commercial wind turbine, a general design created based on publicly available specifications has been used throughout this study. The 3-D Computer Aided Design (CAD) model of the blade including the hub is shown in Fig. 3.4.

The commercial EM solver FEKO [63] provides a series of advanced methods for solving complex scattering problems, such as Method Of Moments (MOM), Multi-level Fast Multipole Method (MLFMM) and Finite Element Methods (FEM), etc.

However, for an extremely large target like the wind turbine, composed by millions of meshed elements, PO provides a realistic time frame for computing the RCS from multiple viewing angles. Therefore, PO with full ray-tracing is applied in FEKO as the solver in our study.

Both the excitation and the calculation is plane wave assuming the blade in the far field. When the azimuth aspect $\phi_0 = 90°$, θ ranges from 0° to 360°, the calculation is made. Notice the viewing angle in FEKO is different from the blade position. The viewing angle θ' is the direction of the observer (the radar receiver). Therefore, in the calculation, the blades stay still but the radar receivers rotates around it, which is equivalent to the blades spinning in the opposite direction. The two can be converted as:

$$\theta = mod(90° - \theta', 360°) \tag{3.9}$$

The calculated RCS of the blade is shown in Fig. 3.5. The RCS repeats every 120° due to the symmetry of the rotor blades. On average, the RCS is approximately 5 dBm^2. However, there are 6 peaks with relatively high values. Three of them occurs at 30°, 150° and 270°, and the RCS is approximately 20 dBm^2. At these viewing angles, the trailing edge of the blade is perpendicular to the radar LOS. The other three peaks are even higher, at around 30 dBm^2, corresponding to viewing angle of 90°, 210° and 330°. This time, the leading edge is perpendicular to the radar LOS. High RCS values occur at these positions because the scattered field is phase coherent, thus combines constructively. However, these peaks have narrow viewing ranges as slight movement of the blade comparable to wavelength will break the coherent alignment.

It is obvious that there are many high-frequency signal components in Fig. 3.5. To better understand the complexity of the signal, the scattered field is calculated at extremely small increment and the resulting time-variant Doppler spectrum is shown in Fig. 3.6. Each Doppler spectrum line is estimated from 50 scattered field samples every 0.09°. The spectrum illustrates similar micro-Doppler signatures observed from

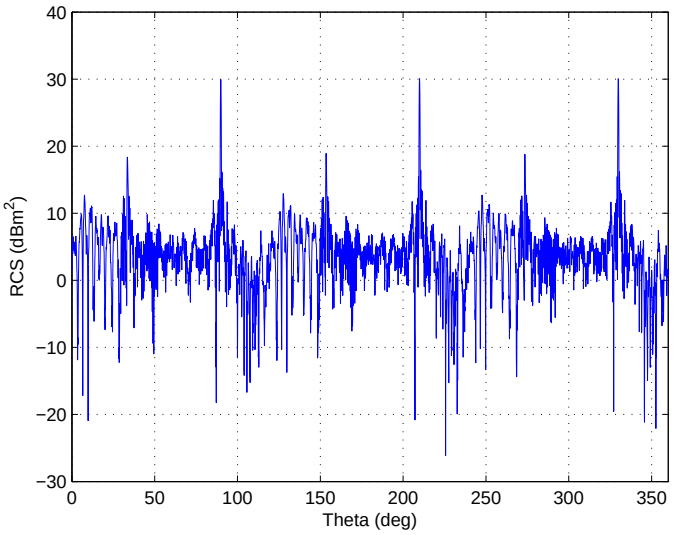

Figure 3.5: Variation of RCS in terms of viewing angle by FEKO using PO solver with full ray tracing. The RCS is calculated every 0.09° in the YZ plane. For a complete revolution of 360°, 4000 samples are obtained.

actual radar signal of wind turbines in Fig. 3.1. However, because the sampling of the rotation is finer in the calculation, the spectrum is non-aliased. From Fig. 3.6, it is clearly seen that the flashes are where the trailing/leading edge turns to be perpendicular to the radar LOS. Therefore, by EM calculation of the scattered field of the wind turbine blade, a preliminary understanding is established on these Doppler flashes as when and how often they will occur. It is also interesting to notice the sinusoid envelope, which should correspond to the tip of the blade. The tip has sharp edge causing diffraction, which has a wide range of viewing angles. There are two trajectories of the envelope, which are the results of two visible tips as the third one is shaded.

Most EM solvers are computationally intensive because fine meshing is involved. A close-form approximation is needed to model the general effect of the wind turbine blade. Thus, an analytical solution based on uniformly distributed scattering centers

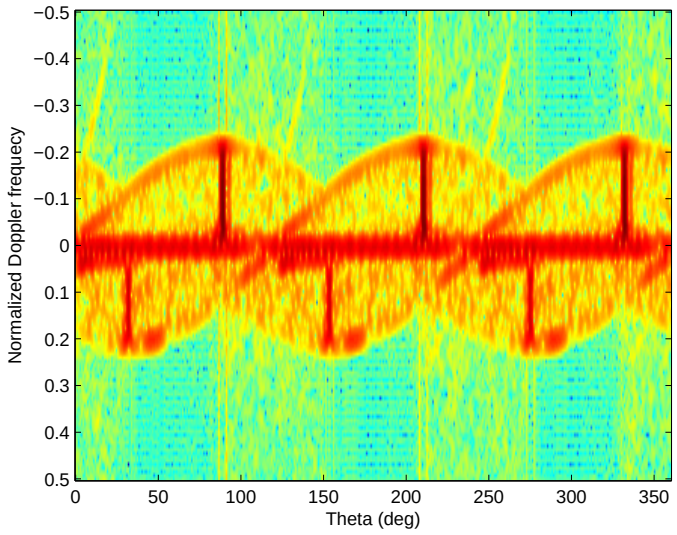

Figure 3.6: Micro-Doppler signature generated using sattered field of the wind turbine calculated using FEKO. The Doppler frequency has been normalized to the sampling rate.

is derived. The complex amplitude of scattered field from an arbitrary point (r, θ) on the blade is:

$$E_b(r, \theta) = A(r, \theta) e^{j2kr \sin\theta} \tag{3.10}$$

where $A(r, \theta)$ is the scattering amplitude, k is wave number. Assuming all major scattering centers are along a straight line, then the overall complex scattering amplitude of the blade is:

$$E_b(\theta) = \int_0^L A(r, \theta) e^{j2kr \sin\theta} dr \tag{3.11}$$

where L is the blade length. Simplifying the scattering center amplitude to be uniform and rotation invariant, i.e., $A(r, \theta) = 1$, then,

$$E_b(\theta) = \int_0^L e^{j2kr \sin\theta} dr = \frac{\sin(kL \sin\theta)}{k \sin\theta} e^{jkL \sin\theta} \tag{3.12}$$

$\theta = \omega t$, where ω is the rotation rate.

$$E_b(\theta) = \frac{\sin(kL \sin\omega t)}{k \sin\omega t} e^{jkL \sin\omega t} \tag{3.13}$$

Thus, the instantaneous Doppler frequency is:

$$f_d(t) = \frac{1}{2\pi}\frac{d[kL\sin(\omega t)]}{dt} = \frac{\omega kL}{2\pi}\cos(\omega t) \tag{3.14}$$

$$f_d(\theta) = \frac{\omega kL}{2\pi}\cos(\theta) \tag{3.15}$$

And the scattering amplitude of the blade becomes:

$$|E_b(\theta)| = \frac{\sin(kL\sin(\omega t))}{k\sin(\omega t)} \tag{3.16}$$

It is clear that the highest positive Doppler frequency and the amplitude maximum are reached at $\theta = 0^\circ$ when the blade moves toward the radar perpendicularly; the highest negative Doppler frequency with another amplitude peak occur at $\theta = 180^\circ$ when the blade moves away from the radar perpendicularly.

A simulation based on the this simplified model is made as shown in Fig. 3.7. Only a single blade radar return signal is simulated. The scattering amplitude periodically reaches peak value at positions perpendicular to the radar LOS. Because unitary scattering amplitude is assumed for both edges, the amplitudes are exactly the same for the blade passing vertically above the nacelle and below it. The spectrogram looks similar to FEKO simulation with periodically Doppler flashes, but with much simplified computation.

3.2.4 RCS of Tower

The tower of the wind turbine is built to be stiff and strong to support the weight of the blades and nacelle, and to withstand the loading from the blade rotation and fluctuation. Therefore, cast iron and steel are the most commonly used material for tower as they are low in cost and have good physical characteristics. The tower also needs to be high above the ground for two reasons: 1) To avoid the tip of the blade hitting the ground, the tower needs to be at least taller than the length of a blade; 2) Wind condition is more favorable higher above the ground. The ideal height of the

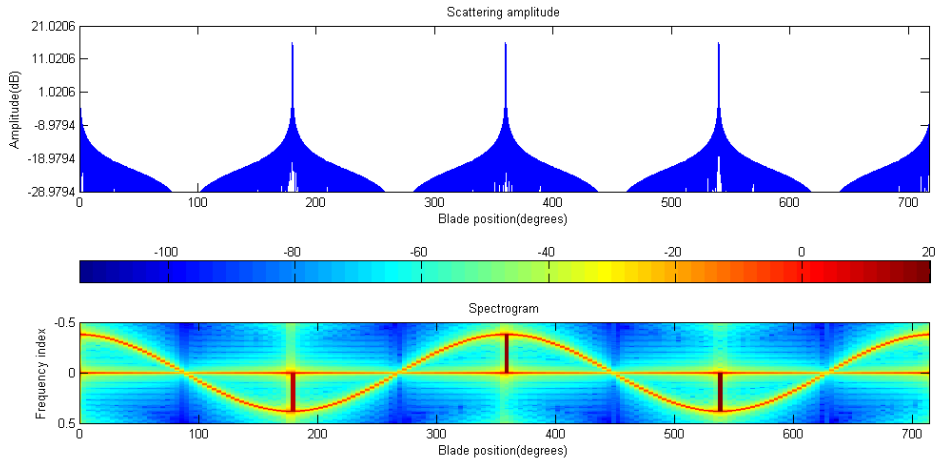

Figure 3.7: Scattering amplitude and spectrogram of simulated single blade radar returns. The scattering amplitude is calculated every 0.01°. Blade length is 40 m and radar frequency is at 2.72 GHz. The dwell for each Doppler spectrum is 3.9°.

tower is above the PBL, which can be over 1000 m in tropical regions. However, the cost to build the concrete foundation, to transport the tower and maintain the wind turbine determines the actual height of the tower. As a trade-off, typical commercial wind turbines have tower height 2-3 times the length of a blade.

Because of the large size and metallic material, the RCS of the tower is normally the most significant among all parts of a wind turbine. Modern wind turbines have cylinder or truncated cone shaped towers as compared to the legacy lattice structure. Both cylinder and cone are perfectly symmetric, thus the backscattered RCS only varies with one aspect angle, usually referred to as the incident angle, which is formed by the incident direction and the axis of the tower as shown in Fig. 3.8. In reality, this angle is determined by the radar elevation angle and the relative terrain. For ground based radar, the elevation angle ranges from 0° to 90°. However, because of the earth curvature, the wind turbines are usually visible to radar at lower elevation scans. Taking into consideration reasonable terrain variations, the common incident

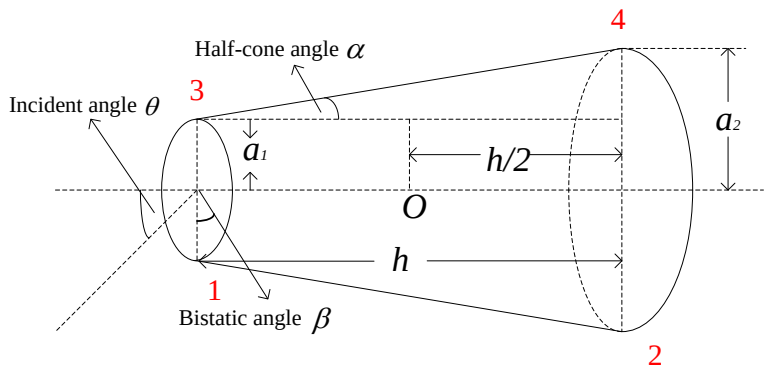

Figure 3.8: Structure of a truncated cone with all four scattering centers. Phase reference is at the Volume center O. The bistatic angle is angle between incident and scattered waves projected on the cross section.

angle is between 85° and 95°. The RCS of a typical wind turbine tower within this range is shown in Fig. 3.9.

For the ease of transportation, the wind turbine tower is manufactured in multiple sections of cylinder or cone. As an example, the dimensions of each section of the 80 m GE wind turbine tower are listed in Table 3.2, where h is the height, a_1 and a_2 are the top and base diameter, respectively, and α is the half cone angle, as defined in Fig. 3.8. From bottom to top, the diameter is tapered down. The half cone angle α is different from one section to another. Thus, the normal incident angles $90 - \alpha$ are 89.22°, 89.01° and 89.61°, from top to bottom. The maximum RCS of the tower is approximately 50 dBm^2, at 89.1°, where all sections are near normal incident. The RCS drops quickly as the incident angle moves away from this direction. At 90°, it is over 20 dB lower. It is also worth noting that the RCS oscillates quickly as the incident angle changes, which is the characteristic of scattering for large revolving bodies in the optical region.

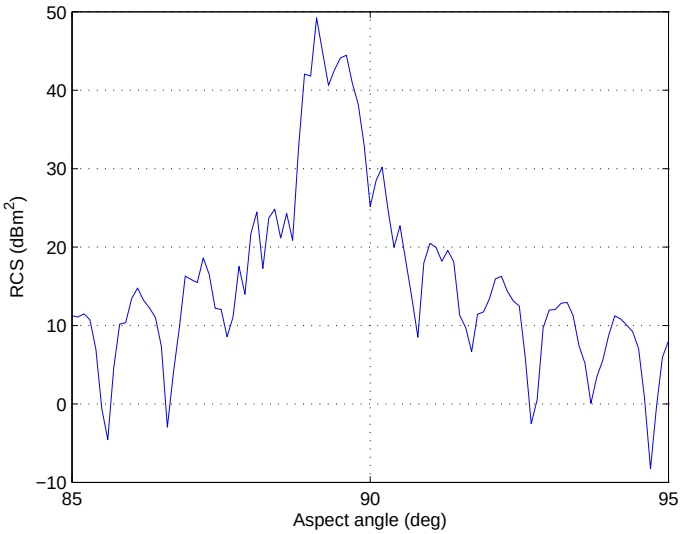

Figure 3.9: Backscattered RCS of the 80-m tower of a GE wind turbine. FEKO is used to calculate the RCS at incrementing incident angles at every 0.1°. The frequency used is 1 GHz.

Table 3.2: Dimensions of the GE 80-m wind turbine tower

	h **(m)**	a_1 **(m)**	a_2 **(m)**	α **(deg.)**
Top	29.5	2.6	3.4	0.78
Middle	26	3.4	4.3	0.99
Bottom	22	4.3	4.6	0.39

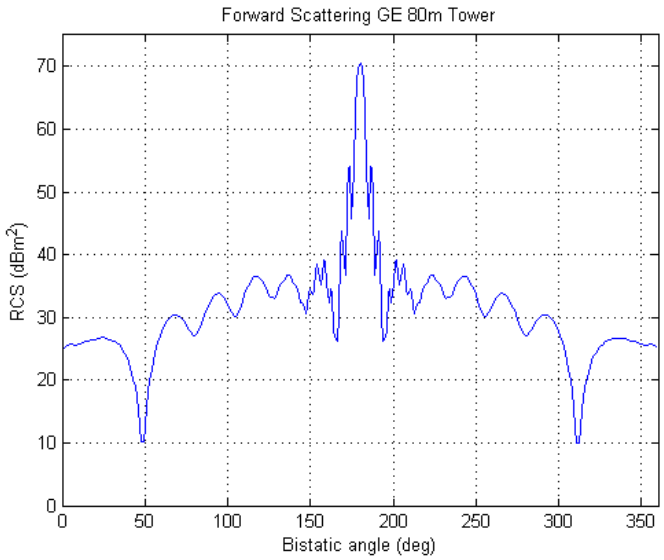

Figure 3.10: Bistatic RCS of the GE 80-m tower with horizontal incident. 0° is the backscattering direction and 180° forward scattering.1 GHz frequency was used in the calculation.

The bistatic scattering of the tower with 90° incident angle is shown in Fig. 3.10. The RCS at 0° is approximately 25 dBm^2, which is consistent with Fig. 3.9. The highest bistatic scattering RCS occurs at 180° along the incident direction. The extremely high forward scattering of the tower is a result of the crawling wave. At different incident angle, the bistatic scattering varies tremendously as shown in Fig. 3.11. The forward scattering is dominant except for the 88° and 89° near specular incident, when the back scatter is higher. The strong forward scattering indicates the incident field is refocused into the forward direction.

FEKO requires fine mesh of the target surface into many small pieces of triangles with edges 1/16-1/6 of the wavelength. For the frequencies of most radar application, the scale is good enough for the fidelity of the shape. However, the computation is tremendous as the tower is too large. The GE-1.6 M 80 m tower requires over 5 million such triangles at 2.7 GHz if meshing in FEKOCAD, which is the CAD tool

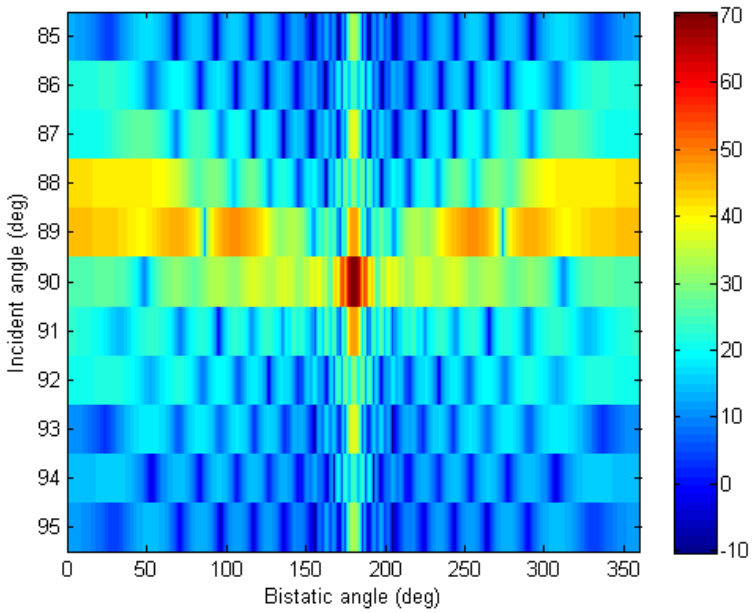

Figure 3.11: Bistatic RCS at different incident angles from 85° to 95°. Both the bistatic angle and the incident angle increment by 1°.

of FEKO. The mesh requirement makes it practically impossible to calculate wind turbine tower RCS for many viewing angles at very high frequency.

GTD is a high-frequency approximation method developed to solve the RCS of typical targets in the optical region. Compared to PO, which is good in solving RCS near specular incident, GTD is accurate in describing geometric discontinuities such as edge, tip and corner. The basic theory is too extensive to be covered here, but the equations used to calculate the RCS of a truncated flat cone [62] are listed as follows for reference:

$$\sigma = \left| \sum_{j} \sqrt{\sigma_j} e^{i\phi_j} \right| \tag{3.17}$$

where $\sqrt{\sigma_j}$ is the scattering amplitude from the j^{th} scattering center, which corresponds to an edge diffraction point and ϕ_j is its phase relative to the reference point.

The scattering centers in the incident plane are shown in Fig. 3.8, which are the intersections of the incident plane and the cone surface. $\sqrt{\sigma_j}$ and ϕ_j are given as [62]:

$$\sqrt{\sigma_1}_{\parallel}^{\perp} = \frac{\sin\frac{\pi}{n_1}}{n_1}\sqrt{\frac{a_1 \cdot csc\theta}{kcos\frac{\beta}{2}}}\left[\frac{1}{\cos\frac{\pi}{n_1} - \cos\frac{\pi+2\theta}{n_1}} \mp \frac{1}{\cos\frac{\pi}{n_1} - \cos\frac{\beta_a}{n_1}}\right] \tag{3.18}$$

$$\sqrt{\sigma_2}_{\parallel}^{\perp} = \frac{\sin\frac{\pi}{n_2}}{n_2}\sqrt{\frac{a_2 \cdot csc\theta}{kcos\frac{\beta}{2}}}\left[\frac{1}{\cos\frac{\pi}{n_2} - \cos\frac{3\pi-2\theta}{n_2}} \mp \frac{1}{\cos\frac{\pi}{n_2} - \cos\frac{\beta_a}{n_2}}\right] \tag{3.19}$$

$$n_1 = \frac{3}{2} - \frac{\alpha}{\pi} \tag{3.20}$$

$$n_2 = \frac{3}{2} + \frac{\alpha}{\pi} \tag{3.21}$$

$$\phi_1 = -2kcos\frac{\beta}{2}\left(a_1 sin\theta + \frac{h}{2}\cos\theta\right) + \frac{\pi}{4} \tag{3.22}$$

$$\phi_2 = -2kcos\frac{\beta}{2}\left(a_2 sin\theta - \frac{h}{2}\cos\theta\right) + \frac{\pi}{4} \tag{3.23}$$

Only the 1^{st} and the 2^{nd} scattering centers are given above as the other two are shaded for all sections in the tower. a_1 and a_2 are the top and base radius, respectively. h is the height. θ is the incident angle. β is the bistatic angle formed by $\hat{k}_i$ and $\hat{k}_s$, β_a is the projection of β on the incident plane.

The above equations have singularity at specular reflection, i.e., $\theta = \pi/2 - \alpha$, where PO is used to get the scattering amplitude and phase in case of normal incident:

$$\sqrt{\sigma} = \frac{2}{3}\left(a_2^{1.5} - a_1^{1.5}\right) cot\alpha\sqrt{kcos\alpha \cdot \cos\frac{\beta_a}{2}} \tag{3.24}$$

$$\phi = -2kcos\frac{\beta}{2}\cos\alpha\frac{a_1 + a_2}{2} + \frac{\pi}{4} \tag{3.25}$$

Near the specular incident, the RCS is interpolated using the PO and GTD result to keep a reasonable smooth transition. This analytical solution (GTD+PO) is compared with FEKO as is shown in Fig. 3.12. The two results match closely especially near specular because both use PO at this incident angle. However, the analytical solution is much more efficient as it does not require meshing.

The complete tower is the superposition of three cones as indicated in Table 3.2. To obtain the RCS of the tower using the analytical solution, the scattering amplitude

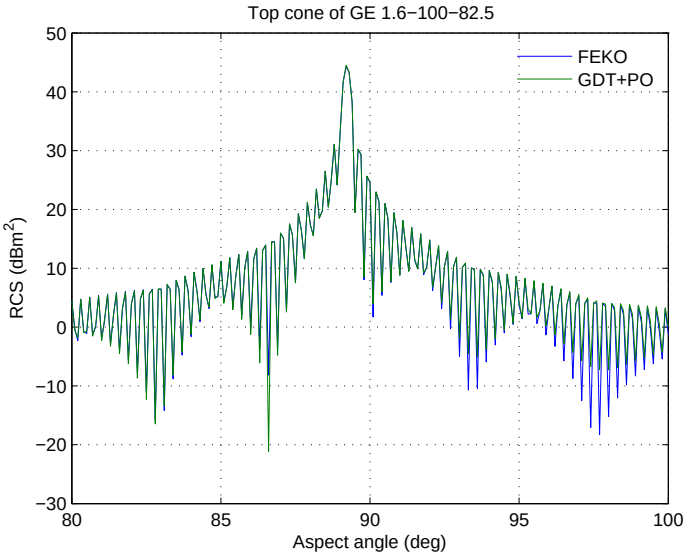

(a)

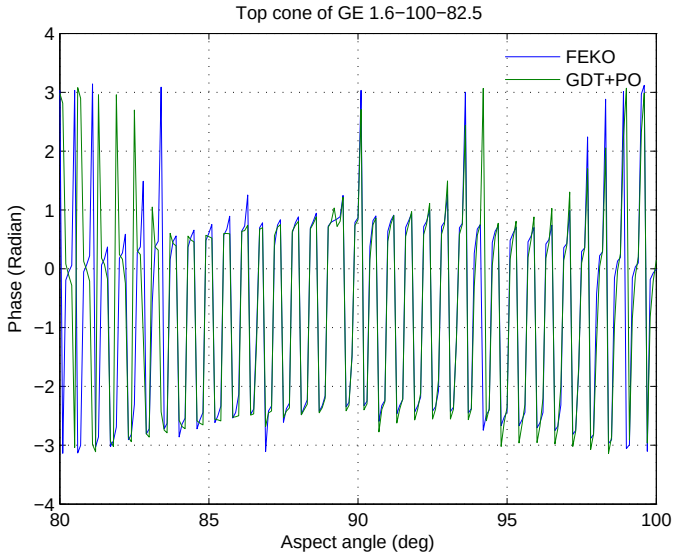

(b)

Figure 3.12: Comparison between the analytical solution and FEKO. Calculation made on the top section of the GE 80-m tower: (a) backscattered RCS, (b) phase referenced to the cone center. The incident angle increments by 0.1°.

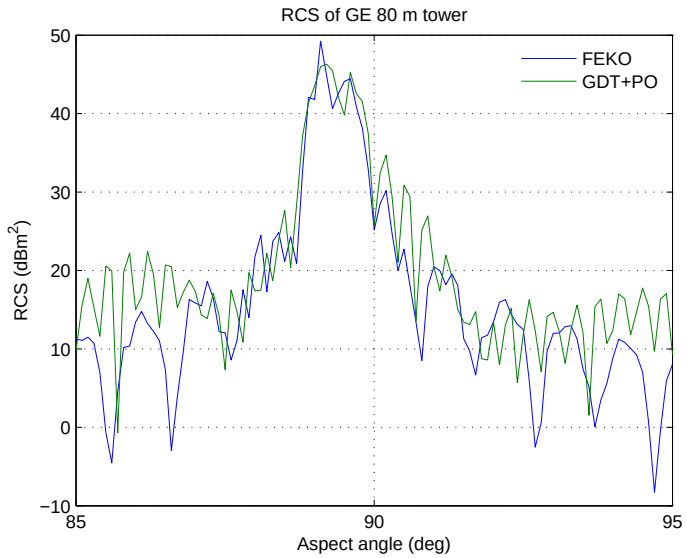

Figure 3.13: Calculated RCS of the GE 80 m tower: comparison between FEKO and the analytical solution. Incident angle increments by 0.1°.

and phase are calculated independently for each cone section, which are then summed coherently. Setting the top cone center as the reference point, then the middle and bottom section have phase delays of:

$$\phi_{mid} = kcos\theta(h_{top} + h_{mid}) \tag{3.26}$$

$$\phi_{bot} = kcos\theta(h_{top} + 2h_{mid} + h_{bot}) \tag{3.27}$$

where h_{top}, h_{mid} and h_{bot} are the height of each cone section from top to bottom respectively. The RCS of the complete tower is calculated and compared with the FEKO result in Fig. 3.13. The two match closely, especially near specular incident. Off specular direction, the analytical solution results more oscillation as it takes into the consideration of edge diffraction, which starts to dominate as the incident wave moves away from the specular direction.

3.3 Impacts of Wind Farms on Weather Radar Operations

3.3.1 Receiver Saturation

There are two types of receiver saturation: the RF saturation and the digital saturation, which are usually related to each other. RF saturation normally refers to the 1 dB compression of the RF receiver, i.e., when the actual output signal is 1 dB lower than the linear output. The digitizer often set its maximum sampling value equal or slightly higher than the 1 dB compression output of the RF receiver, in which case the two types of saturation occur together. When saturated, the overshoot of the output is flattened, resulting in multiple harmonics in the spectrum as illustrated in Fig. 3.14.

The WSR-88D radar replaced the legacy receiver with the Open Radar Data Acquisition (ORDA) platform. The signal path includes the RF link, the Intermedium Frequency Digitizer (IFD) and the signal processor RVP8. The measured system noise with terminated output is -81 dBm when the short pulse is transmitted. The IFD reaches full scale with 6.5 dBm input, which roughly matches the 1 dB compression point of 6 dBm. Therefore the dynamic range is approximately 88 dB. However, a statistical linearization technique is used, which gives an extra 6 dB over the 1 dB compression output to boost the dynamic range to 94 dB [64].

The WSR-88D has the system performance requirement that a reflectivity factor of -7.5 dBz at 50 km must produce an SNR greater than 0 dB. Therefore, a reflectivity factor of -7.5+94 = 86.5 dBz at 50 km will saturate the the receiver. The reflectivity can be converted to equivalent RCS using equation (2.23). The equivalent saturation RCS at 50 km is 56 dBm^2. Adding back the range attenuation of r^4, the saturation

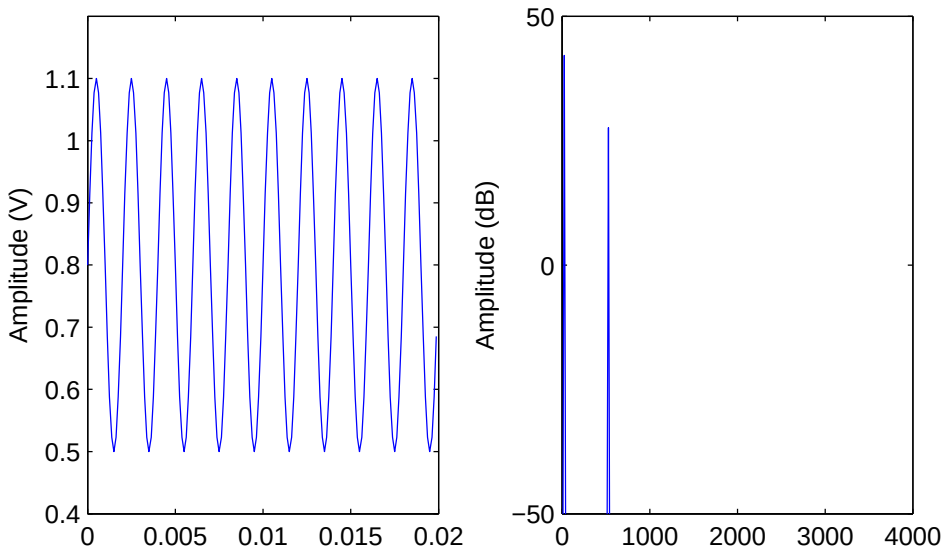

(a)

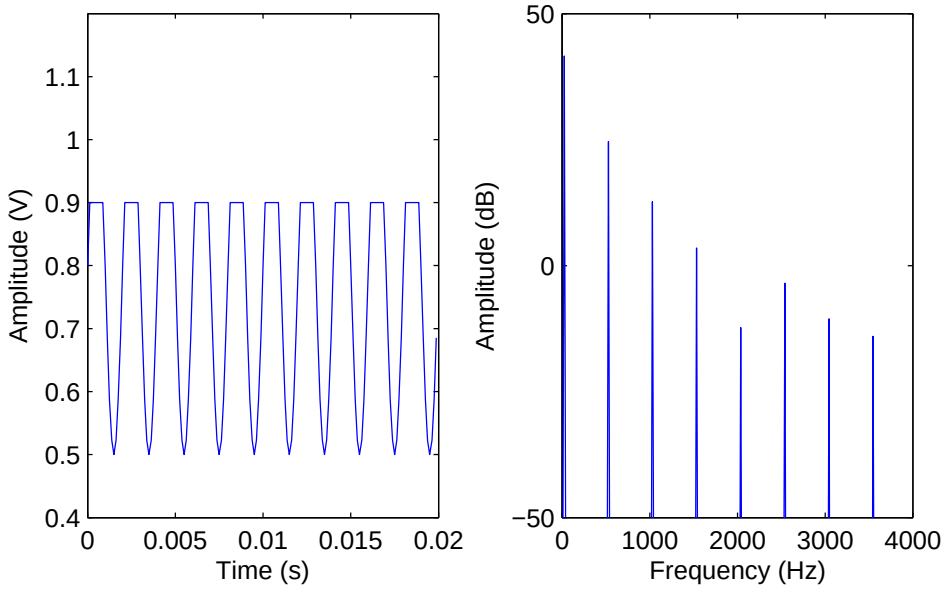

(b)

Figure 3.14: Demonstration of the receiver saturation: (a) unsaturated sinusoid signal in the time domain (left) and frequency domain (right), (b) the overshoots are flatten in time domain of the saturated signal (left). Multiple harmonics are found in the corresponding spectrum (right).

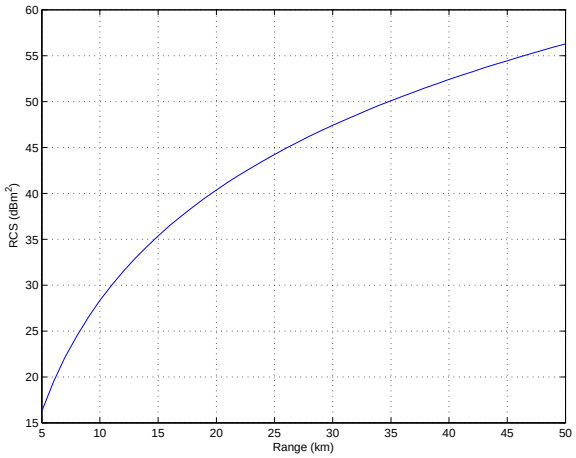

Figure 3.15: Receiver saturation curve of the WSR-88D radar. The curve shows the minimum RCS to saturate the radar receiver at different ranges. The result is derived from the reference sensitivity performance at 50 km and a dynamic range of 93 dB.

curve of RCS versus range is shown in Fig. 3.15. The saturation RCS at range r is obtained from the following equation derived from the radar equation:

$$\sigma_s(r) = \sigma_{ref} \left(\frac{r}{r_{ref}} \right)^4 \tag{3.28}$$

where σ_{ref} =56 dBm^2, r_{ref}=50 km and $\sigma_s(r)$ is the saturation RCS at range r.

As is shown in Fig. 3.15, at 35 km, an object with 50 dBm RCS can saturate the radar receiver. The GE wind turbine tower itself has a RCS of 50 dBm at normal incidence. Therefore, when viewed from the right angle, the wind turbine can potentially saturate the radar receiver within 35 km of range. Simulations of the saturation effect indicate that multiple harmonics of a tone signal may be observed from the spectrum. The actual spectrum of wind turbine from the radar observation in Fig. 3.1 indeed has a few horizontal lines with constant frequencies.

Saturation maybe the cause of these lines; however, a fundamental tone signal does not exist from the wind turbine operation. If the RF input is greater than the 1 dB compression input, the signal will be flattened even before it is demodulated, creating multiple harmonics of the passband signal. These high-power images can

extend to extremely high frequencies. Because it is difficult for filters to have desired attenuations at these high frequencies due to parasitic effect, they will wrap into the baseband when sampled. The sampling frequency used in spectrum analysis is the PRF, which is so low compared to the harmonic frequencies that the harmonics need to wrap around millions of times to get into the baseband. Thus, small phase difference between the sampling clock and the carrier frequency will accumulate to large non-zero frequency bias, which results in the horizontal lines like the ones shown in Fig. 3.1.

3.3.2 Beam Blockage and Diffraction

When a large obstacle is close to the radar, the beam can be partially blocked, resulting in an "EM shadowing zone" behind it. One evident cause for this shadowing effect is that most of the transmitted wave is scattered away from the radar LOS, resulting in the much attenuated EM field intensity behind the obstacle. An example of this effect is shown in Fig. 3.16, where the radar beam is blocked by terrain. Though many wind turbines were installed close to the NEXRAD radar, by far, there has been no documented case for wind turbine blockage.

Many wind turbine blades are made of glass fiber reinforced composite, through which a significant amount of EM wave may propagate. Although the swept area of the rotor blades is large, the instantaneous projected area onto the radar LOS is much smaller. Therefore, the major contribution to blockage, if any, should come from the tower. However, the wind turbine tower has strong forward scattering. The beam is actually refocused forward, thus the blockage effect is minimal.

Diffraction occurs when propagating wave encounters obstacles. The scattered wave combines constructively and destructively, creating complicated interference patterns beyond the obstacle. If the obstacle is relatively small and far from the radiating source, i.e., not scattering the majority of wave back from the propagation

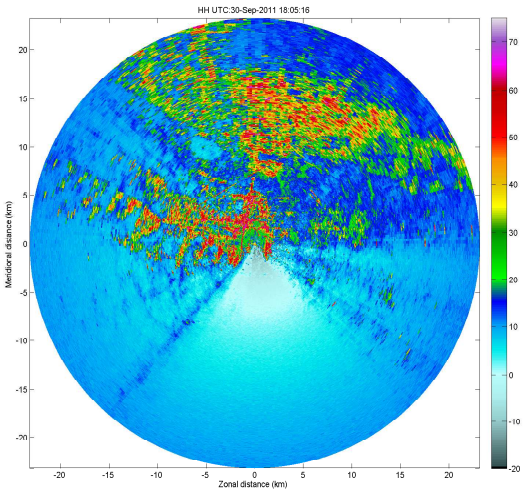

Figure 3.16: An example of beam blockage: a PPI scan at 0° elevation angle from a mobile radar parked off the road. The shoulder on the south is significantly higher than the road, blocking the radar beam and creating a shadow sector behind it.

direction, the blocked section will be illuminated again in a short distance behind the obstacle. If, however, multiple wind turbines are spaced close to each other, the diffraction effect may result several shadowed areas due to the destructively coherent integration of multiple diffractions as illustrated in Fig. 3.17. This shadowing effect resulted from diffraction was first discussed in [20], but no such case has ever been documented, either.

3.3.3 Isolated Clutter

The isolated clutter refers to the type of WTC contamination that is limited in the wind farm area. At the lowest elevation scan where most isolated clutter cases occur, there might be hundreds to thousands of radar resolution volumes within a wind farm. Based on the locations of radar and wind turbines, the terrain and the wind turbine dimensions, the resolution cells potentially contaminated by WTC can be roughly determined by simple geometry.

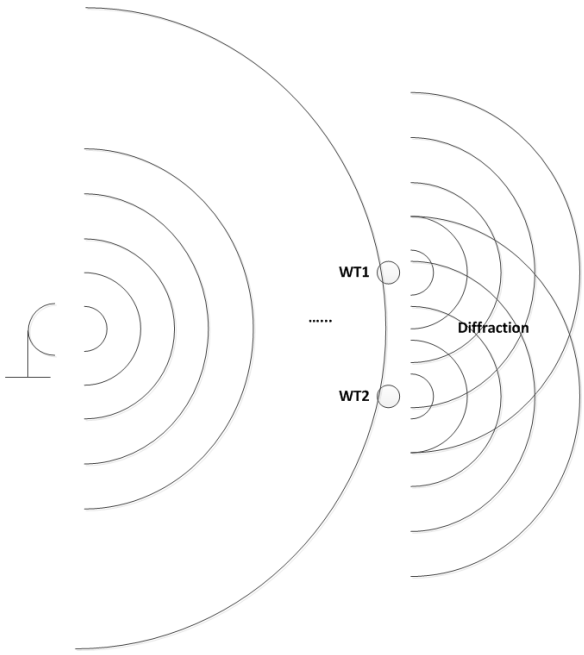

Figure 3.17: Demonstration of the diffraction effect caused by two closely spaced wind turbines. Because the scattered waves interfere with each other, complicated interference patterns exist behind the wind turbines.

The NEXRAD radar has 250-m range resolution, which is longer than the rotor diameter of even the largest wind turbine. Thus, a wind turbine may affect two range gates at most, taking into the account the sampling uncertainty. In the azimuth dimension, the beam becomes wider as the range increases. Beyond 10 km, the beamwidth is greater than 170 m, which is also large enough to accommodate any large wind turbine. Hence, a wind turbine may affect 2×2 resolution volumes at most in one scan. Therefore, the spatial extension of the clutter effect usually follow the shape of the wind farm, making it possible for experienced radar operators to recognize.

The isolated clutter effect of two wind farms near Dodge City, KS, were studied. The radar and wind turbine locations are pinpointed on Google Earth map in Fig. 3.18. A brief description of the wind farms and the wind turbines installed is given in Table 3.3. The wind farms were built six years apart in 2000 and 2006, respectively. It is interesting to notice the wind turbine technology evolving as the wind turbine capacity increases significantly. Although the number of wind turbines in the Spearville wind farm is only about 1/3 that of the Gray County wind farm, the total capacity of the former is 20 MW more than the later.

Fig. 3.19 shows the impact of wind turbines in the Gray County wind farm on reflectivity estimate. The 12 scans are reflectivity estimates of the Gray County wind farm over an hour at every five minutes. It is clear that the clutter effect is limited to the wind farm area only, thus is isolated clutter. The clutter ranges from 37 to 44 km away from the radar, and the azimuth spans 240° to 252° . The cross range illumination of the NEXRAD radar beam is 700 m at 40 km. Thus, the affected area is approximately 28x12 radar resolution volumes or 58.8 km^2 in area, which is small compared to the entire radar coverage. Therefore, excluding data from the wind farm areas has limited impact on radar performance given both the isolated clutter area and the number of such clutter region are small. However, as the number of

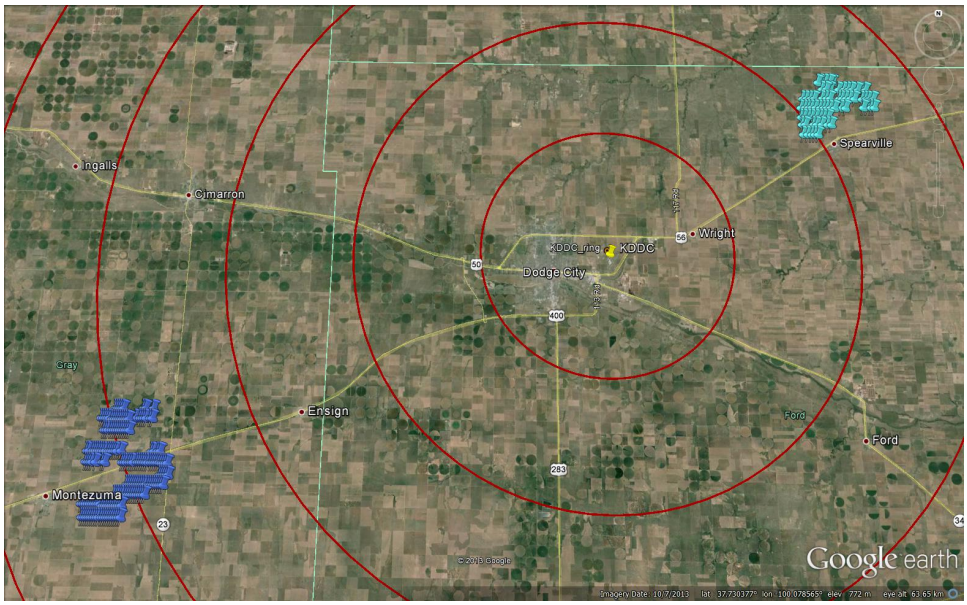

Figure 3.18: Google Earth map of the two wind farms near KDDC radar in Dodge City, KS. The wind turbines in Gray County wind farm are blue pins and the ones in Spearville wind farm are cyan. The range rings are 10 km apart.

Table 3.3: Wind farms near Dodge City, KS

Wind farm	**Gray County**	**Spearville**
Turbine Model	Vestas V47	GE 1.5M
Rotor diameter	47 m	77 m
Hub height	65 m	80 m
Rotation rate	26 rpm	10-20 rpm
Turbine capacity	470 kW	1.5 MW
Number of turbines	172	67
Total capacity	80.8 MW	100.5 MW
Operation year	2000	2006

wind farms grows, more exclusion zones can severely degrade radar performance by reducing valid radar data products.

The reflectivity also varies significantly from turbine to turbine and from scan to scan, which is a result of the non-stationary nature of the wind turbine. Because the rotation is completely unsynchronized with the radar azimuth scan, each time the radar beam revisits the same wind turbine, the blade can be in a different position, therefore, the Doppler spectrum changes from scan to scan. A time-invariant filter thus will fail to mitigate this non-stationary clutter effect. The variation of reflectivity from turbine to turbine is partly due to the same unsynchronized rotation phase from turbine to turbine, and partly because of the fact that the aspect angle may vary given the wind farm occupies a large area.

It is interesting to notice that some wind turbine locations on the north side of the wind farm have transparent color, indicating low SNR. They are not censored all the time, but reemerge from scan to scan. It could be that the reflectivity is low at certain blade positions. However, because this phenomena occurs on the north side only, it is most likely that these wind turbines happened to be in the azimuth position where the rotation axis aligned along the radar LOS. The projection of the velocity of the blades onto the radial direction is close to zero, thus the clutter can be mitigated by conventional clutter filter, resulting low residue power. As the blade rotates, in some scans, the radar happened to capture some radial movements that are outside the ground clutter filter bandwidth, making the clutter to reappear.

Due to the failure of conventional clutter filter on mitigating the clutter caused by moving parts of wind turbines, the reflectivity of post clutter filter wind turbines is still high and often comparable to strong weather returns. Fig. 3.20 shows an example of storms moving across the Spearville wind farm. Without knowledge of the location of the wind turbines, it is difficult to distinguish the WTC contaminated area from the rest of the storm. In fact, WTC resembles radar signatures of several

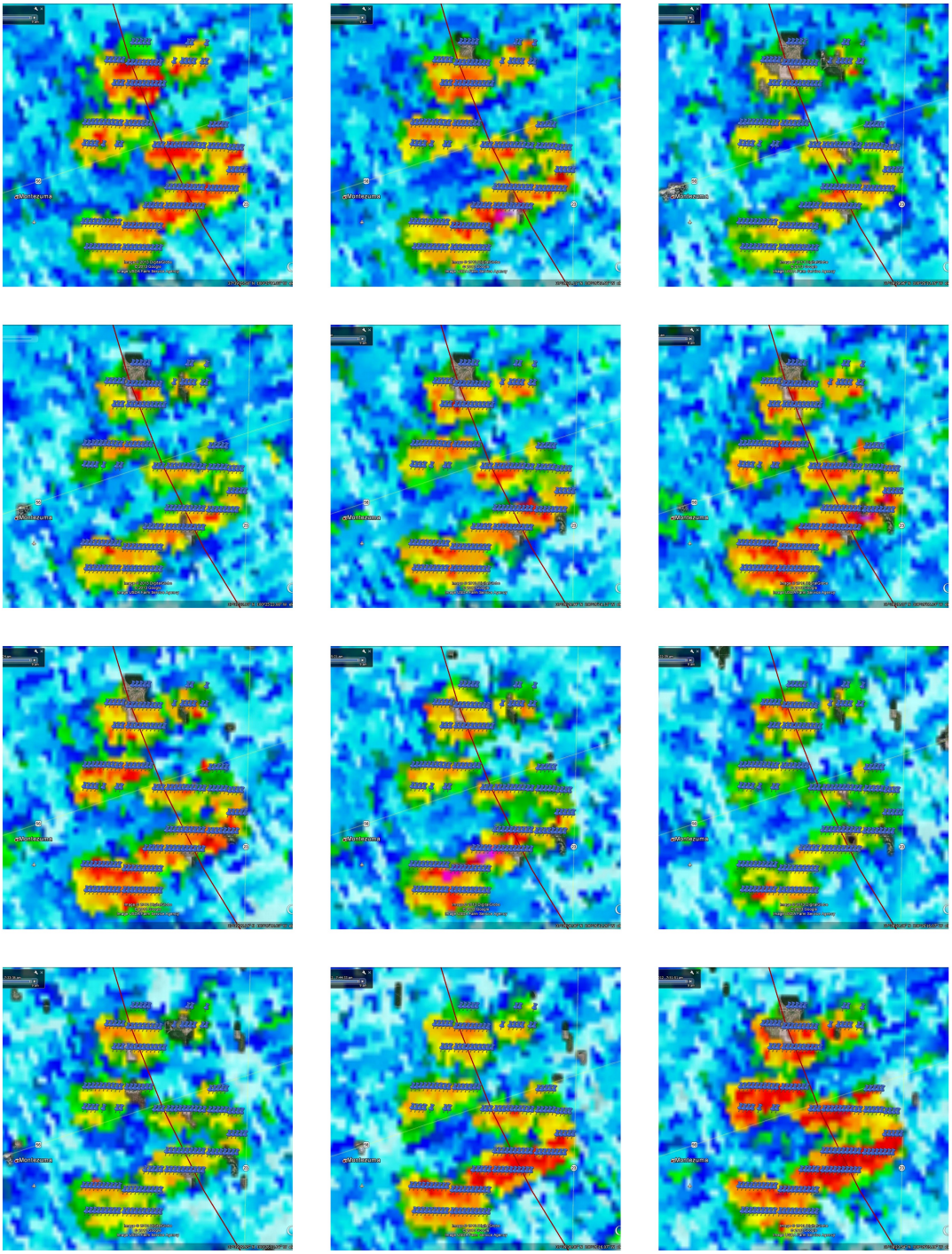

Figure 3.19: WTC impact on reflectivity estimates in Gray County wind farm. Images shown are consecutive scans at 0.5° elevation every 5 minutes. Markers are wind turbine locations. The arc across the farm is 40 km range ring.

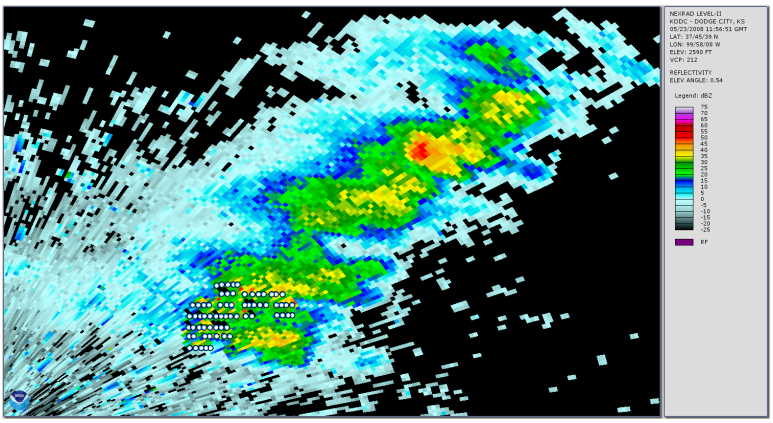

Figure 3.20: Reflectivity near Spearville wind farm. All wind turbines are pinpointed to indicate the wind farm location. The storm was moving from west to east across the wind farm.

types of severe storms, such as tornado, which has high reflectivity, dual-direction radial velocity and wide spectrum width. It is therefore possible for radar operators and signal processing algorithms to falsely recognize wind turbines as severe storm (false alarm or type I error) and vice versa (miss detection or type II error).

3.3.4 Wind Farms in Anomalous Propagation

When evaluating the impact of a wind farm to nearby radar, the first thing to investigate usually is whether the wind turbines fall into the radar LOS coverage. The NWS-ROC has made LOS coverage maps of different clutter heights for all NEXRAD radars. Fig. 3.21 shows an example of the LOS coverage of two NEXRAD radars near Oklahoma City. Obviously, the taller a wind turbine is, the further it stays in the radar LOS and interfere with radar operations.

The LOS coverage map provides a first-step guidance on siting proposed wind farms to avoid interference with the radar. It also helps determine if an existing wind farm may be seen by nearby radars. However, it is worth noting that the LOS coverage varies as the wave propagation medium changes. Depending on the

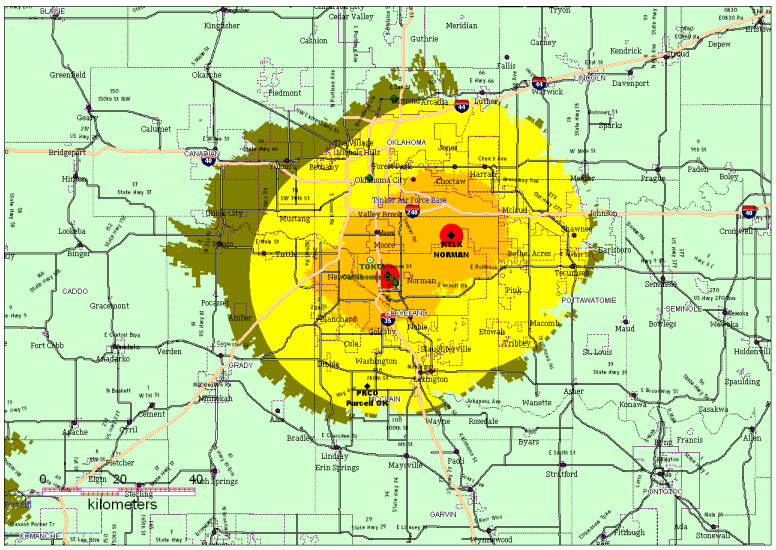

Figure 3.21: LOS coverage of the KTLX and KCRI radar. The orange region is radar LOS coverage at or below 130 m above the ground. Yellow is between 130 m and 160 m. Green is between 160 m and 200 m. Picture can be found on ROC's website.

conditions of the lower atmosphere, the actual LOS coverage can be much larger. For example, in the case of AP, waves that travel above the wind turbines in normal atmospheric conditions may be bent over to hit the wind turbines instead. As a result, wind turbines usually not covered by the radar LOS may emerge when AP occurs. Fig. 3.22 shows an example of wind farms seen by KTLX radar due to AP. The three large wind farms from north to south are the Weatherford wind farm, Minco wind farm and Lawton wind farm, which are normally not in the LOS coverage of KTLX as shown in Fig. 3.21. However, the refractivity gradient at lower altitude at the time was extremely low and AP occurred. The radar beam was therefore bent down instead of shooting over the wind turbines.

3.3.5 Multi-path Clutter Effect

In free space propagation, radar wave travels to the wind turbine, part of which is scattered back, where the return signal is determined by the back scattered field

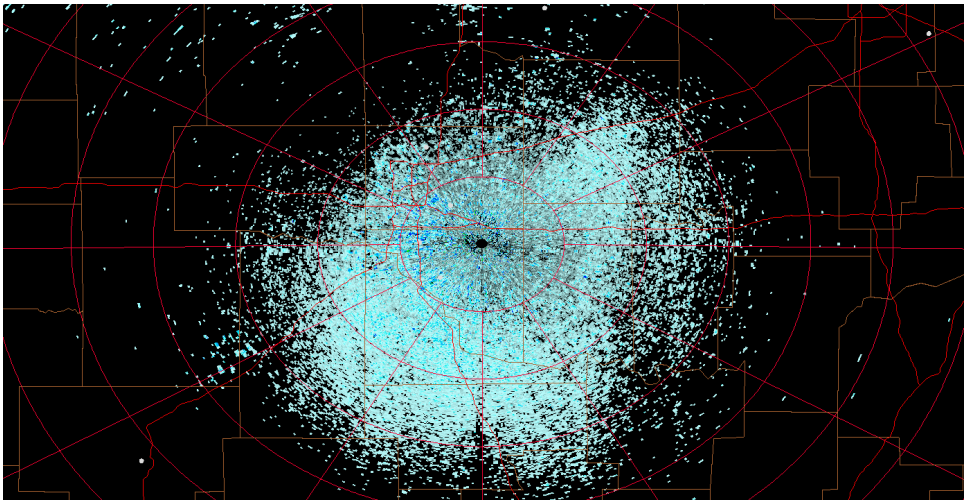

(a) Normal atmospheric condition

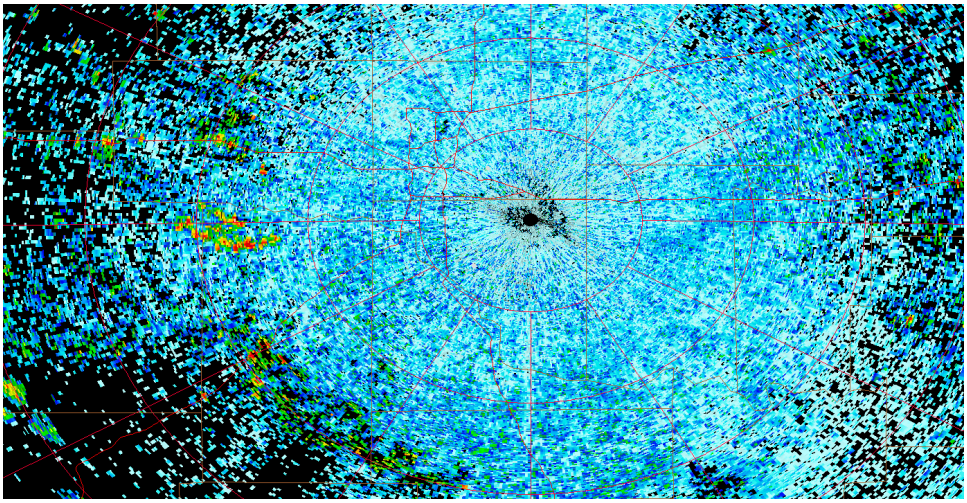

(b) Anomalous propagation

Figure 3.22: Example of wind farms out of the radar LOS coverage in normal atmospheric conditions emerge on the radar map when AP occurs. The three wind farms from north to south are the Weatherford wind farm, the Minco wind farm, and the Blue Canyon wind farm.

of the wind turbine. In reality, in addition to this direct path, there are multiple paths that the wave can travel along to and back from the wind turbine. These higher order scattering mechanisms usually result in much weaker scattered wave compared with the direct-path. Nevertheless, if the wind turbines are close enough to the radar, and/or if the geometry is such that most of the scattered wave is along the direction that favors multi-path, the multi-path clutter effect can result in severe clutter contaminations due to range spreading of WTC.

In the multi-path scattering, the wave is scattered by another object before and/or after it is scattered by the wind turbine. This intermediate scattering resembles the mirroring effect in optics. Because the wave travels further than the direct path, the multi-path clutter seems like the mirrored images of the isolated WTC at further distance. It is worth to clarify though, that the"multi-path WTC" only refers to the clutter effect caused by the multi-path scattering mechanism of a wind farm, which results clearly visible range extension of the clutter compared to isolated WTC. If, however, the images from the multi-path scattering still fall in the wind farm area, it will be categorized as the isolated clutter as it does not expand the clutter contaminated area.

Because the sidelobe of the radar antenna pattern is usually extremely low, it is reasonable to assume that the multi-path clutter only occurs in the main beam, .i.e., both the wind turbine and the third party scatter are in the main beam of the antenna. Under this assumption, the multi-path clutter image only extend WTC in range, but not azimuth, which is consistent with our observations. This assumption also simplifies the multi-path scattering scenarios from three to two dimensions. Weather radar has relatively narrow pencil beam, normally around 1 degree. For the purpose of determining the range of spurious images due to multi-path, the two dimensional geometry in the vertical plane as is shown in Fig. 3.23 can be applied.

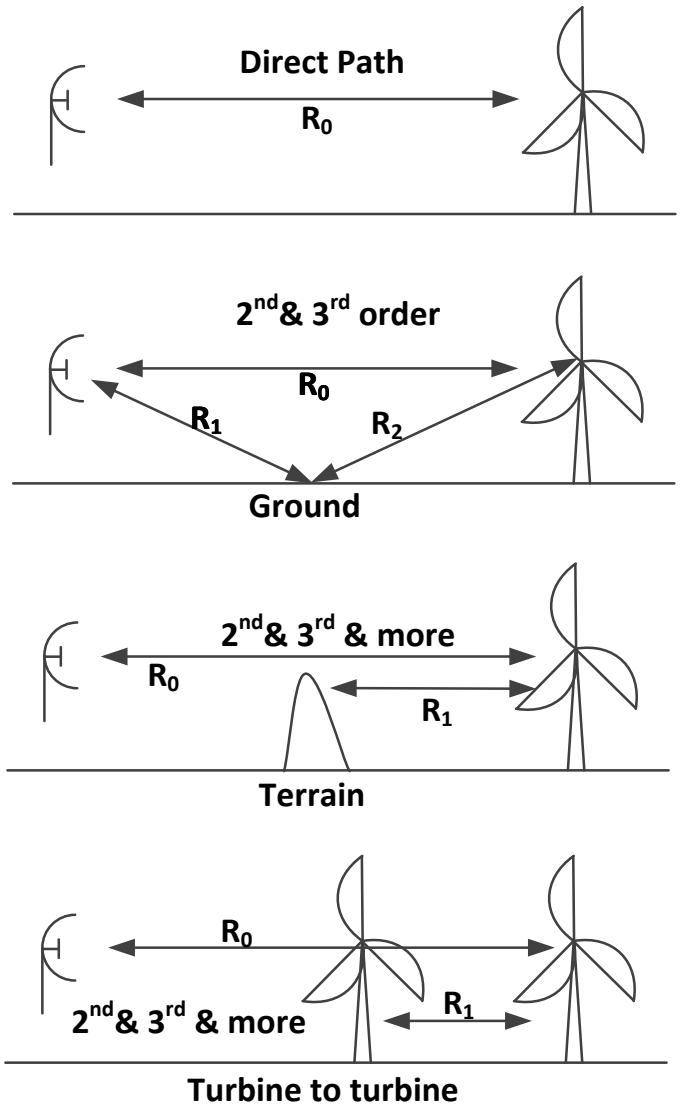

Figure 3.23: Different scattering scenarios. The difference between these scenarios is the third-party scatter, which can be ground, terrain or other wind turbines. Notice the wave needs to be scattered from the rotor blades at least once to be considered as wind turbine clutter.

In case of direct path, the isolated clutter occur at the actual range of the wind turbine R_0. When the wave is scattered by the ground between the radar and the wind turbine, the multi-path WTC will appear at $(R_0 + R_1 + R_2)/2$ for the 2^{nd}-order path and $R_1 + R_2$ for the 3^{rd}-order, both of which are greater than R_0 according to the Triangle Inequality Theorem. However, the difference between $R_1 + R_2$ and R_0 is relatively small given that the elevation difference between the radar and the wind turbine is usually minimal compare to the range distance. Therefore, the multi-path scattering in the "radar-ground-turbine" scenario may not cause the multi-path clutter effect.

As for the scenario where the wave is scattered by the terrain, such as hills between the wind turbine and the radar, the spurious image will appear at $R_0 + (k-1)/2R_1$, where $k(k \leq 3)$ is the order of multi-path scattering, i.e., the 3^{rd}-order multi-path has spurious image at $R_0 + R_1$, the 5^{th} order at $R_0 + 2R_1$, and so on. The larger k, the weaker the return signal becomes from the multi-path scattering. The multi-path scenario of turbine-to-turbine scattering is similar but less terrain dependent, which is more likely to occur. Both may result in significant range spreading of WTC. The return power from higher order scattering may be too low to be noticed on the radar map. There may be other multi-path scenarios, such as the multi-path propagation caused by very low inversion layer, which is extremely rare and too weak to be noticed.

An example of the multi-path clutter effect on NEXRAD radar is shown in Fig. 3.24. There are two large wind farms near the KDYX radar at Albany, TX: the Lone Star wind farm and the Hackberry wind farm. The Lone Star began operation in June 2008, with a full capacity of 400 MW. There are 200 Gamesa 2 MW wind turbines, with rotor diameter of 114 m. These wind turbines were installed 20 to 30 km west of the KDYX radar. The Hackberry wind farm consists of 72 Siemens 2.3 MW wind turbines, with rotor diameter of 100 m. The total capacity is 165.6

MW. The wind farm is located approximately 30 km to 40 km north-northwest of the radar.

A close look into both wind farms in Fig. 3.24 (a) and (b) shows strong clutter reflectivity, where the wind turbines are located, indicating the strongest return comes from the direct path scattering. In Fig. 3.24 (c), some light weather activities were also present. The range spreading effect due to the multi-path scattering is clearly seen. The clutter effect is extended much further beyond the wind farms. The clutter return power is comparable to that of the weather signal and will affect the radar data quality. It is interesting to notice the discontinuities circled in Fig. 3.24 (c) of the weather return near the radar. The missing data is caused by clutter filtering due to hills in the region, while the filter may not be applied elsewhere [65]. The weather activity was moving at low speed, which were also mitigated, resulting in low SNR, thus being censored.

The terrain map of the area is shown in Fig. 3.25. First, it is clear that all wind turbines are installed on the ridge for better wind conditions. The hills between the wind farms and the radar is clearly shown. This type of terrain may lead to the multi-path scattering scenario of "radar-turbine-hill-turbine-radar" or even higher orders. It is believed that this particular terrain contributes significantly to the multi-path clutter effect in this case. Furthermore, it is interesting to notice that many of the wind turbines are aligned along the radial, creating the scenario of "turbine-to-turbine" multi-path scattering, which may also contribute to the multi-path clutter effect.

Based on our case studies, there are many factors that contribute to the occurrence of the multi-path clutter, such as being close to the radar, hills in between the wind farm and the radar, radial alignment of the wind turbines and large wind turbine size, etc. The actual cause of the multi-path clutter, however, varies on a case-by-case basis. The complexity of the multi-path scattering makes it extremely difficult

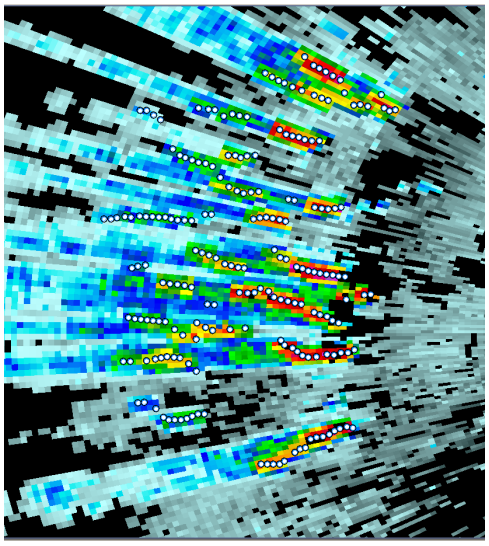

(a)

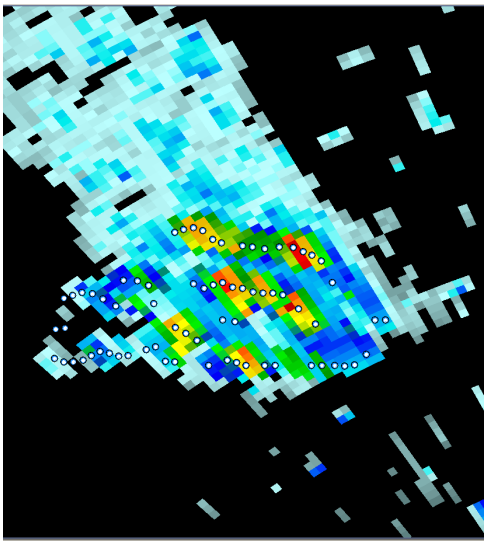

(b)

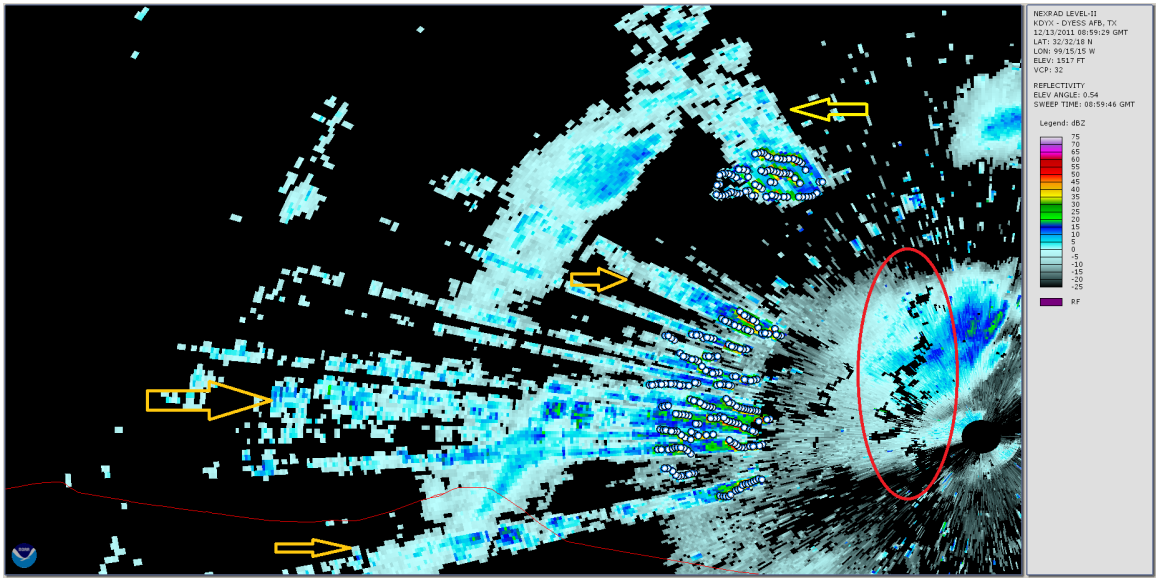

(c)

Figure 3.24: Examples of the multi-path clutter effect on NEXRAD radar KDYX: (a) the reflectivity estimate of the lone star wind farm, (b) the reflectivity estimate of the Hackberry wind farm, (c) full-scope view of the range spreading clutter effect due to multi-path scattering. The arrows points to some of the spurious images caused by multi-path clutter. The hills in between the wind farms and the radar is circled in red.

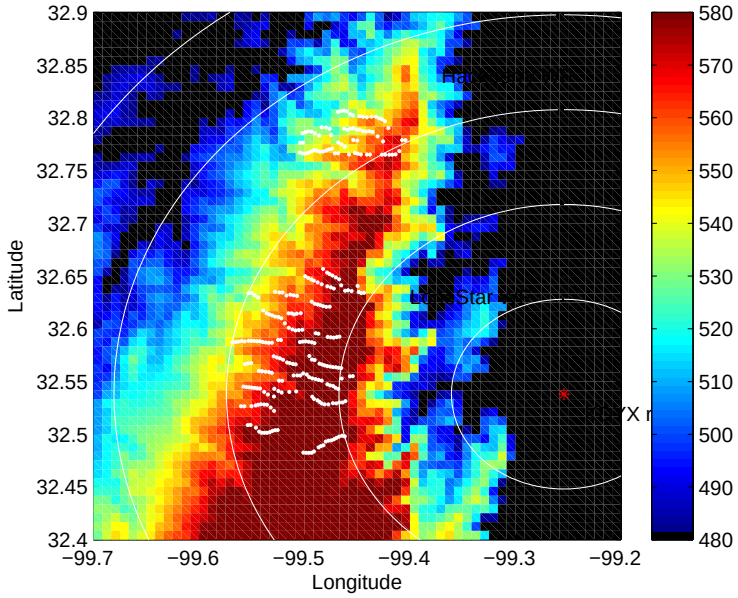

Figure 3.25: Digital Elevation Map (DEM) of the KDYX radar and wind farm area. All wind turbines are marked by white dots. The red dot is the KDYX radar. The color bar is elevation above sea level in meters.

to accurately predict. However, these possible causes provide some basic indications on the presence of this type of clutter.

3.3.6 Impact of WTC on Moment Estimate

NEXRAD data are categorized into three levels: Level I is raw IQ data, Level II is moment data and Level III is weather products such as the base reflectivity images usually seen on public media. Level I data have not been parameterized to be related to weather activities. Level III data are numerous derivatives of Level II data customized to different applications. Therefore, only the impacts of wind turbine clutter on Level II data, i.e., the moment estimates, will be discussed.

The blade rotation of wind turbines results in complicated Doppler spectrum with rich high-frequency components. Because the clutter may coexist with target return at higher Doppler frequencies, conventional clutter removal techniques based on high-pass filter usually fail to mitigate WTC. The tower and slow moving parts such as the hub cause low-frequency clutter, which can be suppressed by such filters. The fast moving blade, however, results in the residue clutter.

One of the most important signal processing step of the NEXRAD radar is the GMAP clutter filter, which is based on the assumption that the clutter is stationary or near-stationary. The WTC, however, has complex spectrum components, which appear in all frequencies, especially when the Doppler flashes occur. An example of applying GMAP to WTC is shown in Fig. 3.26. The same weather signal is coherently added to both the WTC and conventional ground clutter.

Stationary ground clutter is eliminated by GMAP, thus has minimum impact on moment estimate. In fact, the reconstructed Gaussian spectrum based on the moments of the true weather and GMAP filtered ground clutter with weather are almost the same in Fig. 3.26. The WTC, however, has high level of clutter residue after GMAP. The reconstructed Gaussian spectrum indicates significant bias from

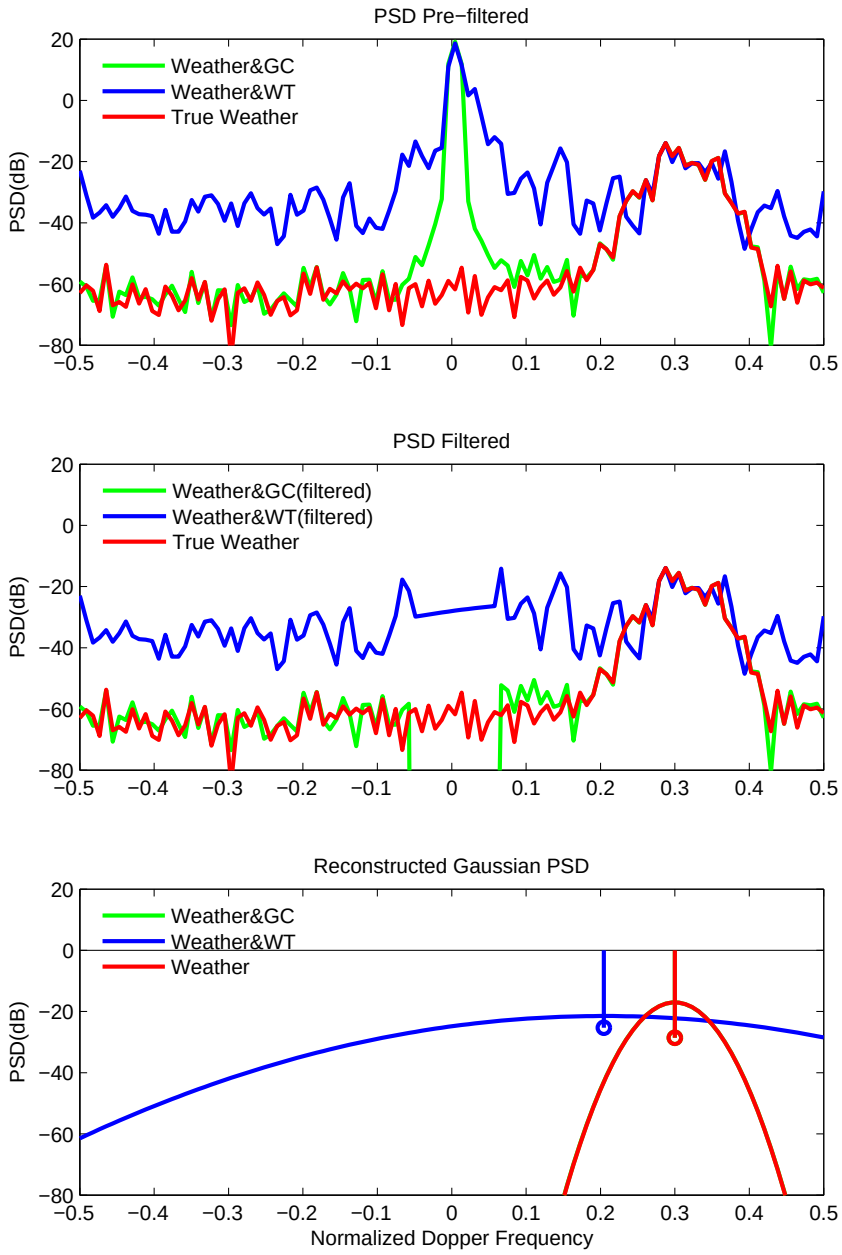

Figure 3.26: Comparison of applying the OU-GMAP filter on weather with Ground Clutter (GC) and weather with WTC. From top to bottom: spectrum before filtering, spectrum after filtering, reconstructed Gaussian spectrum based on moment estimates. The OU-GMAP filter applied is a similar derivation from the actual operational GMAP filter.

the actual moments of weather signal. Therefore, GMAP can be used to mitigate the clutter spectrum components caused by the tower and nacelle. However, it is ineffective to mitigate other spectrum components at higher frequencies caused by blade rotation. The moment estimates using the spectrum after the GMAP filter may be severely biased.

The radar return signal from a resolution volume with both weather activity and wind turbine is:

$$x(t) = s(t) + n(t) + w(t) \tag{3.29}$$

where $s(t)$ is weather return, $n(t)$ is noise and $w(t)$ is the wind turbine return. Both $s(t)$ and $n(t)$ are zero-mean Gaussian distributed random process. $w(t)$ is also treated as a random process as motions of the wind turbine are unknown to the radar. Furthermore, it is reasonable to assume that $w(t)$ is uncorrelated with $s(t)$. All three terms have zero mean after GMAP. Thus, the power of this return signal is:

$$P_x = E|x(t)|^2 = E|s(t) + n(t) + w(t)|^2 \tag{3.30}$$

Upon expansion, all cross terms turn to zero because of zero mean and uncorrelation. And the return power is simply:

$$P_x = E|s(t)|^2 + E|n(t)|^2 + E|w(t)|^2 = P_s + \sigma_n^2 + P_w \tag{3.31}$$

Thus, the return power is the sum of power of weather return, receiver noise and wind turbine. Because the reflectivity is proportional to radar return power, the wind turbine clutter will bias reflectivity estimate to much higher value.

The residue clutter will also bias the mean radial velocity estimate. This bias can be either positive of negative, depending on the actual shape of the clutter spectrum, which varies from turbine to turbine. This random bias renders mean radial velocity estimate meaningless. The radial velocity map of the Spearville wind farm is shown in Fig. 3.27. The dominant color inside the wind farm is gray and dark green/red,

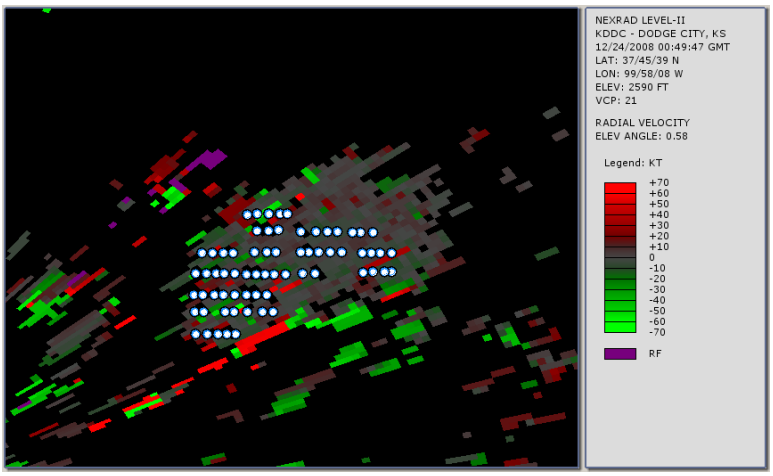

Figure 3.27: Mean radial velocity estimate in the vicinity of Spearville wind farm. The conventional clutter filter has been applied to remove low-frequency spectral components. White dots are the wind turbine locations.

indicating slow-moving targets. Therefore, although the blade tip speed can be extremely high, the main contribution to the Doppler spectrum is still from the slow moving parts, namely the nacelle, hub, nose cone and the root of the blades.

Because of the spreading of Doppler spectrum due to WTC, the spectrum width estimate should be much higher than the actual value. The spectrum width estimate of the Spearville wind farm is shown in Fig. 3.28. As the blade rolls, the Doppler spectrum has continuous response up to the maximum Doppler velocity corresponding the tip of the blade. However, as the scattered wave from the three blades combine coherently, some of the spectral components are enhanced, while some are reduced. Nevertheless, the overall spectrum is widened, over-estimate of the spectrum width.

3.4 Field Measurements Using Mobile Radar

In order to understand the fundamentals of wind turbine and radar interactions, baseband IQ radar signal from the wind turbine are needed. For investigating particular wind farm impact, it is best to study the data of the affected radar, as there can be

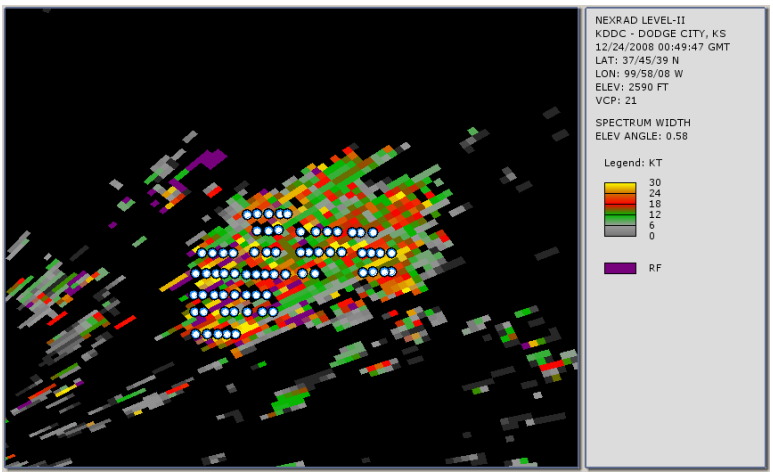

Figure 3.28: Spectrum width estimate in the vicinity of Spearville wind farm from KDDC radar Level II data in VCP21 mode. The elevation angle is 0.5°.

many site-specific factors contributing to the wind turbine return signal, such as terrain, wind turbine locations, climate, etc. A data acquisition campaign was launched back in 2006 to collect a series of Level I IQ data of wind turbines using NEXRAD radars [26]. However, for general wind turbine radar signal characterization, it is better to exclude all these factors and only focus on the wind turbine radar return itself. Our experiment mobile radar RaXPol is thus deployed to two wind farms in Oklahoma and configured to collect IQ data for further study of wind turbine radar interactions.

RaXPol (Rapid X-band Polarimetric Radar) is a rapid scanning mobile radar operated by the Advanced Radar Research Center (ARRC) at the University of Oklahoma [66]. The radar is mounted on a mid-size truck as shown in Fig. 3.29, allowing for rapid deployment. The radar is also rapid in scanning and sampling, as 30 rpm of azimuth scan is achieved using an extremely responsive powerful pedestal. The fast sampling rate is in both the fast time (range sampling) and slow time domain (repeated pulse). 7.5 m range gate spacing and up to 10 kHz PRF are realized by customized digital radar receiver. A brief description of the system specifications [67]

Figure 3.29: RaXPol radar leveled for field experiment. The photo is provided through the courtesy of Dr. Philip Chilson.

is listed in Table 3.4. This radar was developed for weather observation as all the "rapid" features are customize designed for observing fast evolving severe weather activities.

3.4.1 Minco Wind Farm Field Survey

The Minco wind farm was built in three phases from 2010 to 2012. The total capacity is more than 300 MW, produced by 188 GE 1.6 MW wind turbines. The 63 wind turbines in Phase I are pinpointed on Google Earth map in Fig. 3.30, where the two sites that RaXPol was deployed to are also marked. Two PPI scans of different elevation angles were made at site one. The 0° scan has been shown previously in Fig. 3.16 as an example of beam blockage. The 2° scan is shown in Fig 3.31, where the wind turbines are clearly visible. The red and yellow dots of high power are wind turbines returns as they match the wind turbine locations.

At the 2^{nd} site, the RaXPol was configured in spotlight mode. The elevation angle was lowered to 0.5 ° as there is no clear visual blockage along the radar LOS. The wind

Table 3.4: RaXPol system specifications

Parameter	**Value**
Transmit power	20 kw
Frequency	9730 MHz
Pulse width	0.1-40 μ sec
Beam width	1 °
Gain	44.5 dBi
Sidelobe level	-26 dB
Polarization	dual (H and V)
Sampling resolution	16 bits

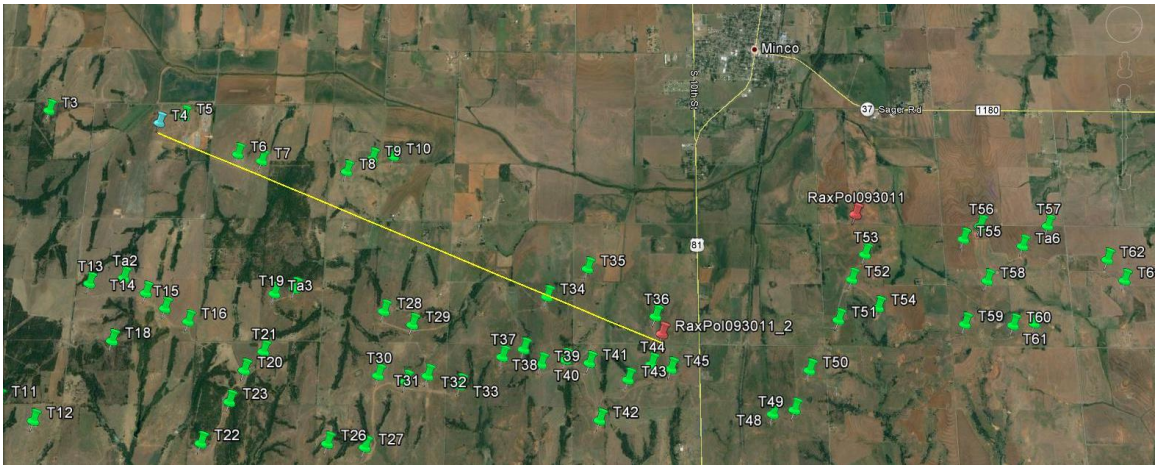

Figure 3.30: Wind turbines (green pins) in Minco Phase I project. The two red pins are sites where the RaXPol was deployed.

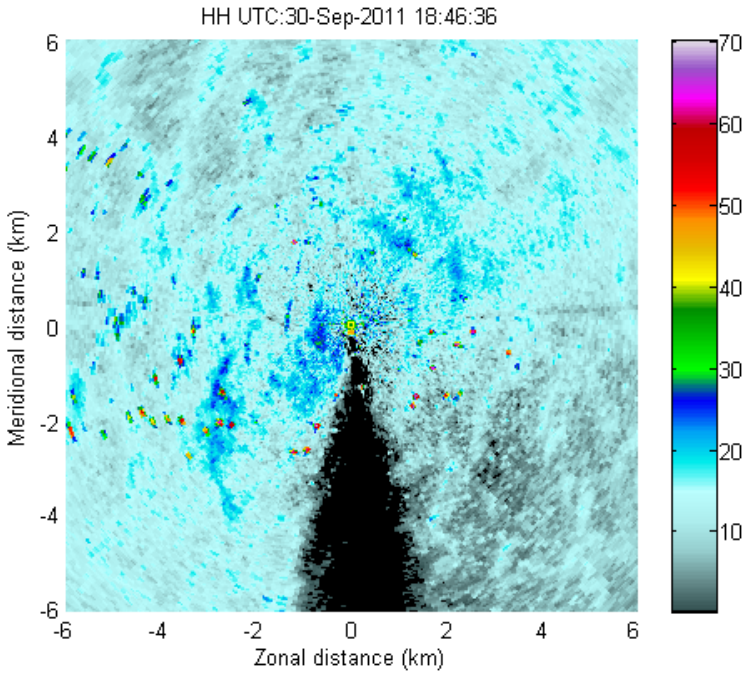

Figure 3.31: Power estimate of the 2° scan at site one. Range gate spacing is 30 m. Notice the sector on the south of radar has extremely low return power due to partial beam blockage.

turbine under study is T4 in Fig. 3.30, which is approximately 7300 m from the radar, with an azimuth angle of 292.8° from north. The radar beam was precisely steered to the wind turbine in this case. The beam width at this distance is approximately 127 m. In elevation, the beam center is at 66.5 m above the ground. The GE 1.6M wind turbine has an overall height of 121 m. The wind turbine base elevation is 6 m lower than the radar feed horn height. Thus, almost the entire wind turbine falls in the radar beam height wise, except where it is close to the base, as is shown in Fig. 3.32.

At the time of measurement, the wind direction recorded at the Minco Mesonet [68] station was approximately 12° from north. Since the wind turbine blades always yaw into the wind direction, assuming the wind direction at the wind turbine is the same as the Mesonet measurement, the wind turbine blades were illuminated by the radar beam from behind with an aspect angle of 10° , which is close to parallel to the radar LOS as is shown at the top of Fig. 3.32. In fact, the visual observation of the wind turbine blade was almost parallel to the radar LOS at the time of measurement, which was consistent with the Mesonet records. The highlighted leading edge moves away from the radar at the top and toward the radar at the bottom of the rotation, given the blades spins clockwise when viewed from upwind. Meanwhile, the span of T4 in azimuth dimension is:

$$L = Dsin(\phi) \tag{3.32}$$

where D is the rotor diameter and ϕ is the angle between rotation plane and LOS, which was estimated to be 10°here. Therefore, the azimuth span is 14 m, which is much less than azimuth beam width. In this case, the wind turbine was illuminated by the radar beam uniformly in the main beam.

The spectrogram of T4 is shown in Fig. 3.33. It is worth noting that only the horizontal polarization is shown as the two polarized channels were not well calibrated at the time of measurement. Because the radar configuration and the wind turbine model observed are both different, the spectrogram is not supposed to be comparable

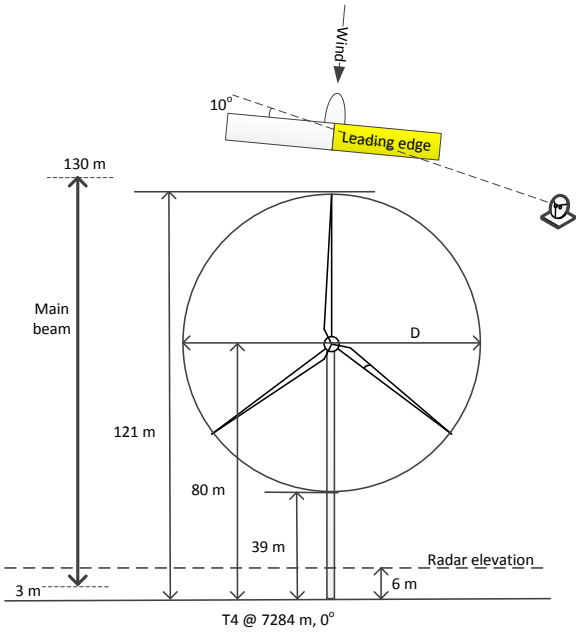

Figure 3.32: Beam coverage of the wind turbine T4 in the Minco wind farm. The azimuth aspect with respect to the radar beam is shown on the top. The bottom shows the elevation coverage. The range of the wind turbine and the azimuth offset from the beam center are marked at the bottom.

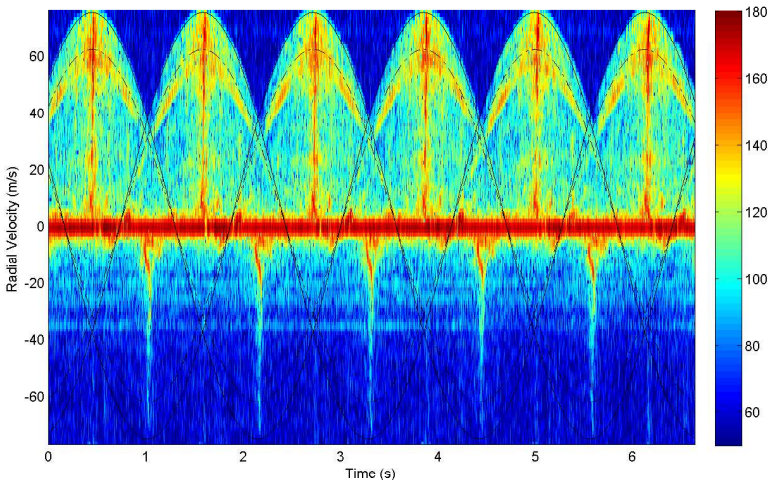

Figure 3.33: Spectrogram of the wind turbine T4 in the Minco wind farm. Derived sinusoid envelopes are overlaid on the top.

with the previous KDDC measurement in Fig. 3.1. However, there are a few similarities between them. The periodic single-sided Doppler flashes are found on both of them. The much weaker horizontal lines are also found on both, which are suspected to be caused by saturated RF front end.

The difference, however, is much more significant. Because the PRF of RaXPol was configured to 10 kHz, which is much higher than that of the NEXRAD radar, even though the operating frequency is also higher, the aliasing velocity is raised to approximately 77 ms^{-1}. The rotation rate can be estimated from the period of the flashes, which is approximately 3.4 s every three flashes (one complete revolution). Thus, the rotation speed is 17.6 rpm. The rotor diameter of the wind turbine is 82.5 m. The tip velocity thus is 76 ms^{-1}. After taking into account the radial projection, the maximum radial velocity is approximately 75 ms^{-1}. Hence, the spectrogram is non-aliased.

The non-aliased spectrogram reveals more details about the Micro-Doppler signature of wind turbine radar return. For the first time in this study, a clearly defined envelope is observed. The power density immediately drops to the noise floor beyond

the envelope. Therefore, the envelope corresponds to the tip of the blade, which has the maximum radial velocity at all time. The time varying radial velocity of the blade tip is:

$$v_t = \omega \frac{D}{2} \cos(\phi) \cos(\omega(t - t_n)) \tag{3.33}$$

where ω is the rotation rate in radians per second, ωt_n is the initial rotation phase. This trajectory is overlaid on top of the spectrogram, which closely match the envelope. However, the envelope only exists on the positive side of the spectrogram. Based on the orientation of the blade, the positive radial velocity occurs when the trailing edge is facing to the radar LOS with a small incident angle. This observation is consistent with the RCS characterization that diffractions from the trailing edge should have much wider viewing angle range than the specular reflection from the leading edge. Within the envelope, there is another sinusoid trajectory, with maximum radial velocity of approximately 62 ms^{-1}. This strong back scattering must correspond to geometric and/or material discontinuity.

On the other side of the spectrogram, the envelope fades away. However, Doppler flashes are found where the extension of the envelope reaches the maximum speed. Therefore, the Doppler flashes on both sides of the spectrogram occur when the tip of the blade reaches the maximum radial velocity, indicating that the flashes correspond to when the blade is perpendicular to the radar LOS or $\theta = k \cdot 120°$, where k is a non-negative integer, which is consistent with previous RCS calculation. It is interesting to notice that the spectrum is "broken" at lower frequency for each flashes on the negative side. This may be due to the shading from the tower.

3.4.2 Blue Canyon Wind Farm Measurement

The Blue Canyon wind farm is the largest wind farm in Oklahoma. It is located northwest of Lawton. The project is built in 3 phases (I, II and V). Phase I has 45 NEG Micon 1.65 MW wind turbines, with a collective nameplate capacity of 74.25

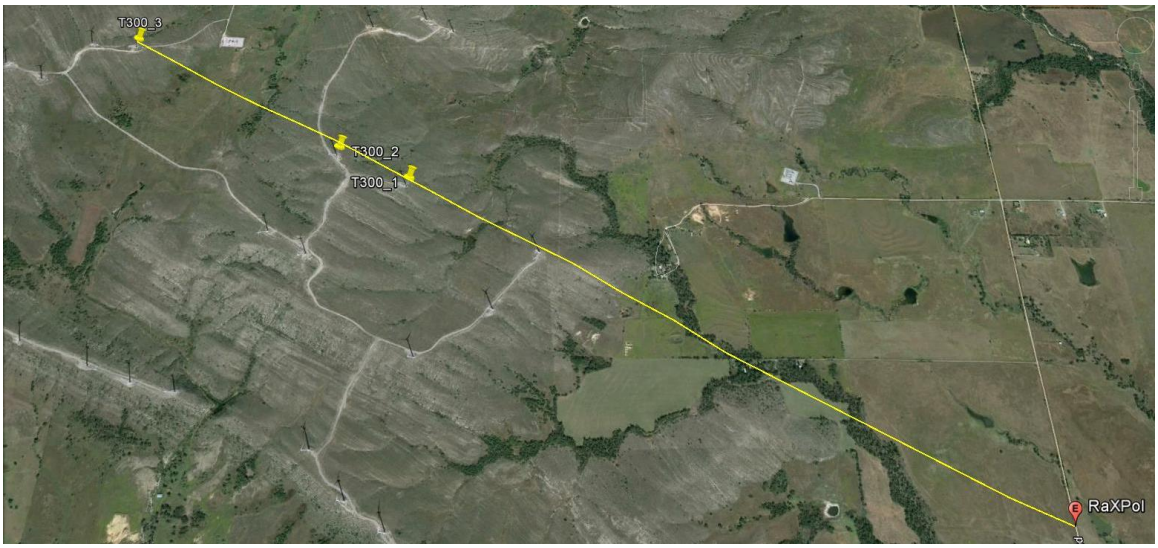

Figure 3.34: RaxPol deployment in the Lawton wind farm. The red pin is RaXPol, and the three yellow ones are wind turbines found along the radar beam. The azimuth steering is 300° from north.

MW. The wind turbines started commercial operation in December 2003. Phase II consists 84 Vestas V80-1.8 MW wind turbines, increasing the total capacity by another 151.2 MW. It began commercial operation in December 2005. The wind turbines measured at the time of experiment are from phase V of the project, which began operations in December 2009 and has 66 GE sle 1.5 MW wind turbines. The rotor diameter of the GE sle 1.5 M wind turbine is 77 m. The hub height, however, has two options according to GE's brochure: 65 m or 80 m. No public data is available on which one is selected for the Blue Canyon wind farm. Yet from the combined height submitted to the FAA from the developer, the hub height for this particular wind farm is estimated to be 65 m.

At the Blue Canyon wind farm, the spotlight mode data were acquired with the radar beam steered to 300.4°. The location where RaXPol was parked and the wind turbines in and close to the LOS are pinpointed in Fig. 3.34. The terrain in the wind turbine proximity is much higher than the radar base. In order to avoid beam

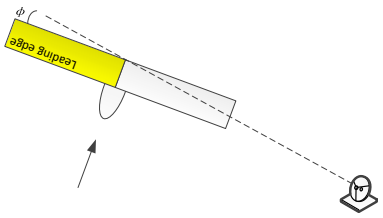

Figure 3.35: Top view of the wind turbine blade of the Blue Canyon wind farm at the time of measurement. The arrow denotes the wind direction recorded by Mesonet.

blockage, the radar elevation angle was set to 2°. The PRF is again set to 10 kHz to avoid spectrum aliasing. Range gate spacing is 30 m and the actual range resolution is 75 m. The wind direction recorded by nearby Mesonet station was 202° from north. Thus, the wind turbines were illuminated from the front this time, but again with an aspect angle of ϕ=8°, which is also close to being parallel to the radar LOS as shown in Fig. 3.35.

Three wind turbines are found along the radar LOS. The beam coverage in elevation is calculated based on the DEM data and 4/3 earth model as shown in Fig. 3.36. The range of the wind turbine from radar and the azimuth offset from the beam center are marked at the bottom of each plot. Unfortunately, none of them has the entire rotor blade in the main beam of the radar. The first two are not even in the main beam in azimuth dimension. The 3^{rd} wind turbine, falls in the main beam azimuthally, but only the upper of the swept area is in the main beam in elevation.

The spectrogram of these wind turbines is shown in Fig. 3.37. The micro-Doppler signatures are different from each other yet also share some similarities. The first and second wind turbine are close to each other, it is therefore assumed that the wind direction and speed are the same. Therefore, the only major difference is the rotation phase, i.e., blade position θ. In fact, the spectrogram looks the same except a shift in the time domain. Because the second wind turbine is further off from the beam

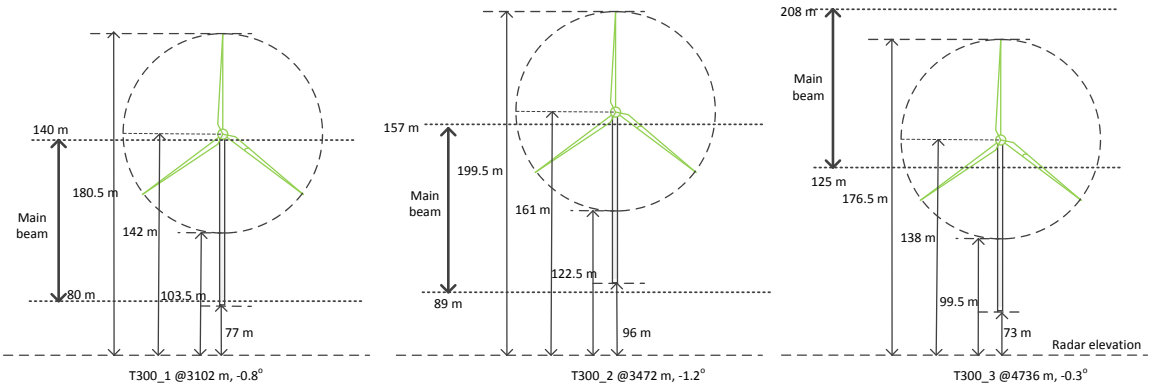

Figure 3.36: Elevation beam coverage of the wind turbines at the Lawton wind farm. The distance and azimuth offset from the beam center are again marked at the bottom of each wind turbine.

center in azimuth, the power density seems much weaker. However, the spectrum component at the zeros frequency turns much more stronger.

As has been discussed previously, the major contribution to the zero-frequency spectrum component is the tower. The RCS of the tower is extremely sensitive to the incident angle, so this spectrogram difference is possibly caused by the incident angle change. In fact, the elevation difference between the two bases is 19 m as shown in Fig. 3.36. At the range of 3000 m, this converted to incident angle difference of 0.36°, which is significant in determining the RCS of the tower.

The negative side of the spectrogram has extremely low SNR for the first two wind turbines, as the upper part of the rotor blade was not fully illuminated by the main beam. On the contrary, the lower half of the blade of the third wind turbine was not in the main beam while the upper half was. Therefore, its spectrogram is opposite to the previous two as is shown in Fig. 3.37 (c). In the Minco field survey, the spectrogram of the wind turbine has clearly defined envelope only on one side of the spectrum. The spectrogram in Fig. 3.37 also has this single-side envelope feature. However, it is most likely caused by the tapering effect of the radar antenna beam pattern as none of the wind turbines was fully illuminated by the main beam.

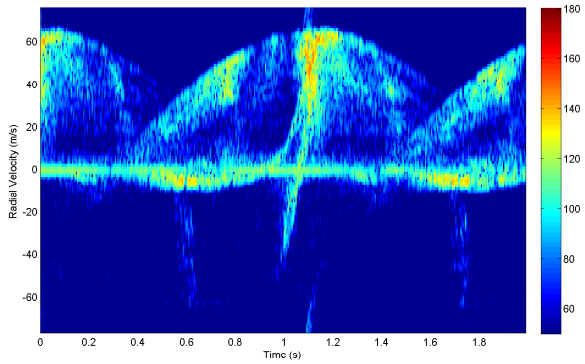

(a)

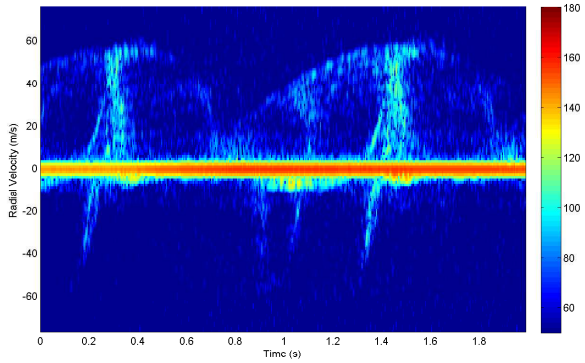

(b)

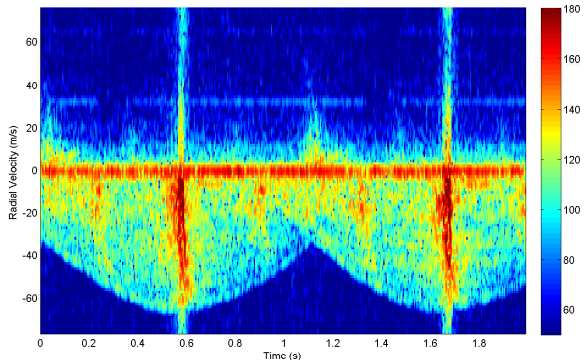

(c)

Figure 3.37: The spectrogram of wind turbines at the Lawton wind farm. From top to bottom are T300_1, T300_2 and T300_3. The color mapping is set to the same scale for direct comparison.

Despite the tapering effect of the beam pattern, the upper half of the rotation plane of the third turbine should be fully illuminated by the main beam according to the calculation result in Fig. 3.36. With the rotor blade orientation in Fig. 3.35, the leading edge moved toward the radar in the upper half of the plane. The envelope on the negative side of the spectrogram thus is attributed to this movement. Compared with the spectrum envelope in the Minco experiment, corresponding to the trailing edge moving away from the radar at the upper half of the plane, it is tempting to draw the conclusion that the spectrum envelope corresponds to the blade sweeping the upper half of the rotation plane. However, the spectrogram of the first two wind turbines in Fig. 3.37 (a) and (b) also suggests that similar envelope also exists on the positive side of the spectrogram, when the trailing edge rolls over the lower half of the rotation plane away from the radar. It is, therefore, difficult to reach a conclusive statement about the Micro-Doppler signature of wind turbines from only two experiments. More measurements in difference scenarios, such as various aspect angle, frequency and wind turbine models are needed.

Chapter 4

Scaled Wind Turbine Model Measurement

Scaled measurement of wind turbine is measuring a scaled wind turbine model that is much smaller than the actual wind turbine in the EM controlled environment, namely the anechoic chamber. The main purpose of the scaled measurement of wind turbine is to address the limitations encountered in radar measurements and provide a configurable testbed for wind turbine studies, where radar data of wind turbines are much easier to obtain. With a scaled wind turbine model, all measurements can be accomplished indoors, where not only the EM environment is controlled, but the motions of wind turbine are also controlled. The scaled measurement also helps understand the fundamentals of the scattering mechanisms of wind turbines and the wind turbine radar signal characteristics. It also provides the measured database for the telemetry based mitigation algorithm that will be discussed in the next chapter.

4.1 The Radar Wind Turbine Testbed

The Radar Wind Turbine Testbed (RWT^2) is a reconfigurable platform designed for indoor microwave measurement of the wind turbine. It includes a scaled wind turbine model, a Vector Network Analyzer (VNA) for frequency domain measurement, a lab radar for time domain measurement and a computer for control and communication. The system schematic is shown in Fig. 4.1. The "external instruments" in the figure include a power amplifier for boosting transmit signal when using VNA, and a pulse generator for synchronization when using the lab radar. The amplifier is optional as the VNA outputs up to 10 mW. The pulse generator was integrated into the lab

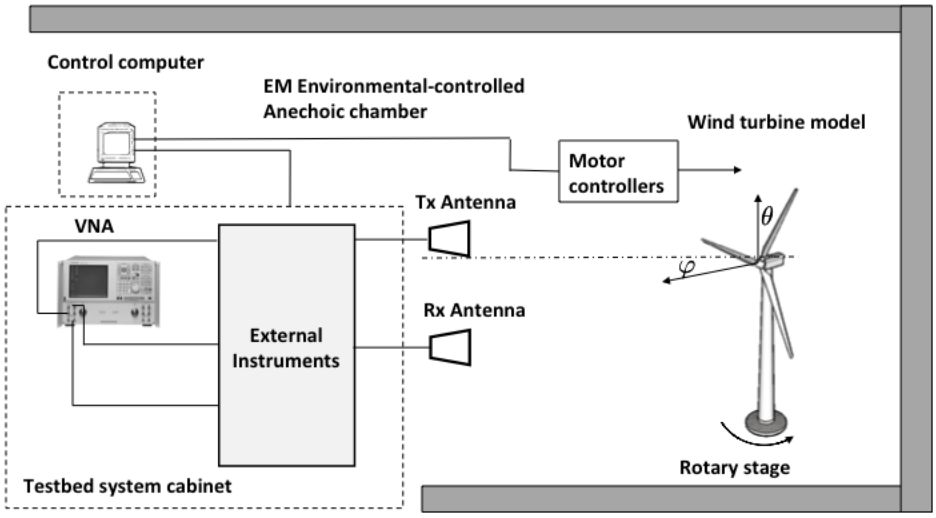

Figure 4.1: Sketch up of the RWT^2 system. Only the VNA is shown in the testbed system cabinet, which can be replaced by the lab radar in the time domain measurement.

radar in the latest design. Therefore, the current system only requires cable adapters between the VNA/lab radar and the antennas.

The transmitting and receiving antennas are identical. There are three pairs of directional antennas used in the measurement: single polarized X-band rectangular horn antenna (AR^2 MA86551), dual-polarized wide band open ridge antenna (Lindgren 3164-05) and Ka-band rectangular horn antenna (Pasternack PE9850-20). Table 4.1 gives a brief comparison of these antennas. The former two are compatible with the lab radar, while the Ka-band antenna can only be used with the VNA due to bandwidth limitation of the lab radar.

The RWT^2 is set up inside the RF anechoic chamber of the Radar Innovation Lab (RIL), where all subsequent experiments are made. The RF anechoic chamber is a room designed to provide a quiet EM environment in limited space to emulate the actual effect of the open-space with infinite dimensions. Fig. 4.2 gives an inside view of the anechoic chamber in RIL. RAM is laid all over the interior surface of

Table 4.1: Comparison of antennas used in the RWT[2]

Model	MA86551	ETS Lindgren 3164-05	PE9850-20
Band(GHz)	8-12.4	2-18	26.5-40
Nominal gain(dB)	17	12 for upper 2/3 band	20
Beamwidth	25°	35° @10GHz	15°
Polarization	single	dual linear	single

the chamber. The RAM is designed with arrays of pyramid pieces pointing inward the chamber as shown in Fig. 4.3. The shape allows multiple reflections between the pyramids, through which the wave energy will be absorbed until it dies out. Typical material of the RAM comprises a rubberized foam material impregnated with controlled mixtures of carbon and iron [69]. This combination provides sufficient loss of the incident wave.

Continuous wave measurement has low range resolution, therefore, all returned wave is assumed to be from the target. In such measurement, the performance of the chamber is critical as any reflections from objects other than the target contribute to the return signal as well. In reality, due to the limited size of the chamber and the cost constraint of high performance RAM, there will be such spurious returns in the measurements. The major contributor to such returns are from the back wall and the ceiling. In almost all of our measurements, the return signal is gated so that most of these interference can be eliminated. To best separate the target return from any interference, the measured target is always placed in the center of the chamber, which is referred to as the "quiet zone".

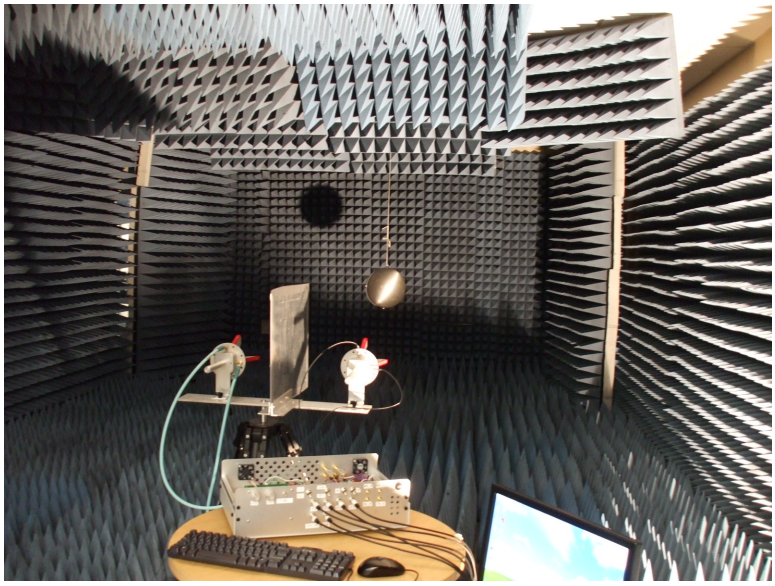

Figure 4.2: Inside the anechoic chamber of RIL. The chamber is semi-closed with a small open area near the entrance for placing equipments. The picture shows measuring of the metal sphere for calibration.

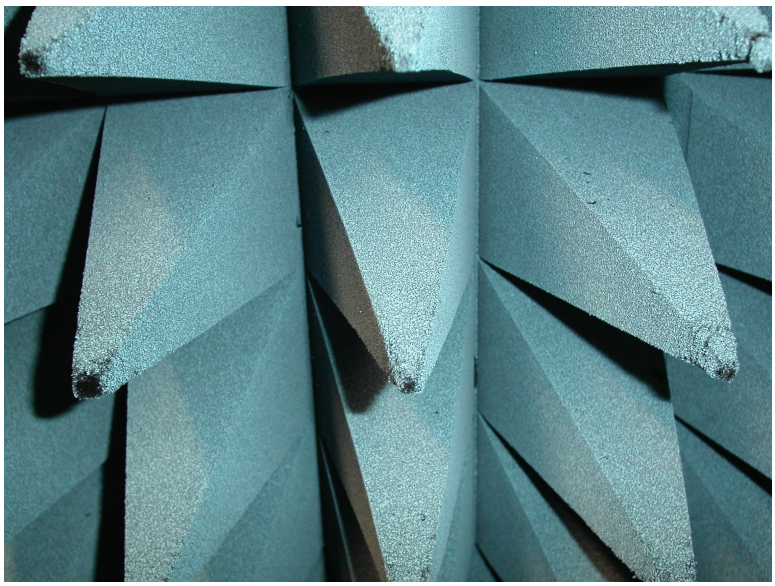

Figure 4.3: A close look of the RAM. There are multiple pyramids in each RAM block for easy installation. The back of each block can be glued to the interior of the chamber.

(a) (b) (c)

Figure 4.4: The inside and out of the wind turbine model: (a) the outside of model. Notice the tower is tapered the same way as a full-size wind turbine, (b) the motor in the nacelle that drives the hub shaft. The wiring of the motor goes through the hollow tower to the base and is connected to the host computer via a serial port, (c) rotary stage supporting the model, which can be remotely controlled to yaw.

4.2 The Scaled Wind Turbine Model

A laboratory scaled wind turbine model has been customized and fabricated based on the geometry of actual wind turbines. A picture of this model is shown in Fig. 4.4. The scaling factor of the model with respect to the typical commercial utility-scale wind turbine is approximately 1:100. The hub height is 1.06 m and the length of each blade is 0.3 m. The body of the tower is made of steel coated with Oriented Polypropylene (OPP) plastic film. Blades are made of Epoxy-fiberglass material. Note that a steel rod is embedded within each blade to simulate the lightning rods in actual wind turbines, which also provides structural enhancement.

A compact motor Quicksilver NEMA 17H-3 is installed inside the nacelle to control blade rotation, i.e., position, speed and direction, as is shown in Fig. 4.4 (b). A servo

motor was used to provide accurate feed back of the current position. Despite its compact size, the motor provides a maximum torque of 400 $mN \cdot m$ at maximum 48 V input and low rotation speed, which is sufficient to drive the light weighted blades. The encoder has 8000 counts per revolution, providing a theoretical accuracy of 0.045°. The motor is connected to the SilverDust I-series controller, which is powered by the DC input and interfaced with the host computer via a serial port connection. A set of ASC-II codes are provided by the manufacturer to control the rotation and request various status, which are used to program our own LabVIEW drivers.

The hollow tower is threaded into a base with a hole for wiring, which is mounted on a rotary stage for yaw control. The actual yaw mechanism of the commercial wind turbine relies on a yaw ring and a set of gears under beneath the nacelle. The gears drive the nacelle to travel around the yaw ring according to the wind direction detected by the anemometer on top of the nacelle, so that the rotor blades can always face into the wind. A powerful AC servo motor is used to rotate the entire model including the tower. However, as the tower is right cylinder, they are essentially the same process. Similar to the roll motor, the rotary stage is controlled by a motor controller, which is connected to the computer via serial port as well. It is worth noting that each blade can be manually pitched if needed.

4.3 Theorem of Similitude

Theorem of similitude is the theoretical basis connecting the full-scale measurement and the scaled model measurement. In order to transform the scattered EM field from the scaled model measurement to that of the full-scale radar target, the time scale factor in terms of wavelength needs to be the same with space scale factor in terms of target dimension. Assuming the full scale target has N scattering centers:

$$\overline{E'} = \sum_{n=1}^{N} \overline{E'_n} e^{-jk' r'_n} \tag{4.1}$$

where $\overline{E'}$ is the scattered field of the full-size target, $\overline{E'_n}$ is that of the n^{th} scattering center, k' is wave number of the full-scale measurement, and r'_n is the range of the n^{th} scattering center. The scaling factors in temporal and spatial domain are:

$$r_n{}' = p r_n \tag{4.2}$$

$$k' = \frac{1}{q} k \tag{4.3}$$

Assuming the scattering amplitude of each scattering center is scaled linearly:

$$\overline{E'_n} = \alpha \overline{E_n} \tag{4.4}$$

The scattering amplitude can be reorganized as:

$$\overline{E'} = \sum_{n=1}^{N} \alpha \overline{E_n} e^{-jk \frac{p}{q} r_n} \tag{4.5}$$

It is obvious that only if $p = q$, will the total scattered field keep the simple linear relation between the full-size and scaled target:

$$\overline{E'} = \sum_{n=1}^{N} \alpha \overline{E_n} e^{-jk r_n} = \alpha \overline{E} \tag{4.6}$$

where it can be further proved [70] that $\alpha = p$. In other word, the scattered field of a scaled model can be linearly converted back to that of the full-size radar target, if and only if the wavelength is scaled the same as the target dimension.

According to the Theorem of Similitude, the measuring frequency needs to be scaled up by the same factor that the target dimension is scaled down. The lab wind turbine model is approximately scaled down 100 times compared to the utility scale commercial wind turbine. The scaled measurement is performed at 10.5 GHz by the scatterometer, corresponding to 100.5 MHz actualy radar measurements for the full-size wind turbine. Even at 40 GHz, the highest frequency measured with the VNA,

the corresponding frequency of full-scale measurement is 400 MHz. Weather radar applications do not use frequencies this low. Though it seems impossible to simply scale the measurement back to the wind turbine- weather radar scenario, the scaled measurements still help to understand how the unique geometry of the wind turbine affects the Micro-Doppler radar signature and statistical characteristics.

4.4 The Scatterometer

The lab radar is named scatterometer as it is made to study the scattering characteristics of measured objects. It is essentially a low-power Pulsed-Doppler radar. As an indoor radar, fine range resolution or wide bandwidth is highly desirable, as range gating is needed to separate target return from clutter. The bandwidth of the scattometer is 100 MHz, resulting in a 1.5 m range resolution. The system specifications of the scatterometer are given in Table 4.2.

The operating frequency is selected at X band based on budget limit and many application requirements. 10.5 GHz is the center frequency of the bandpass filter that was available off-the-shelf at that time, saving development time and extra cost on customizing. The 126 mW transmit power is the combined peak power of both channels. The power density at 0.91m (3 feet) away from the antenna in the LOS is 0.019 mW/cm^2, which complies with the FCC radio safety regulation [71].

Both pulse width and PRF are real-time configurable. The bandwidth is limited by sampling rate of the digitizer, which is 200 MHz. To comply with the Nyquist sampling theorem [7], the bandwidth of the anti-aliasing filter is set to 100 MHz. The radar was originally designed for spotlight mode to focus on target for a long period of time. Mechanical azimuth steering was later added for scaning. The system noise is -94 dBm with a dynamic range of 93 dB, which is determined by the 16-bit sampling depth. The radar transceiver is designed with small form factor similar to a standard ATX tower.

Table 4.2: System specifications of the scatterometer

Frequency	10.5 GHz
Transmit power	126 mW
Pulse width	6-200 ns
PRF	95-24400 Hz
System bandwidth	100 MHz
Scan type	Mechanical azimuth
Polarization	Linear dual pol
Mode	PPI/Spotlight
Dynamic range	93 dB
System noise	-94 dBm
Transceiver dimension	400 mm × 300 mm × 130 mm

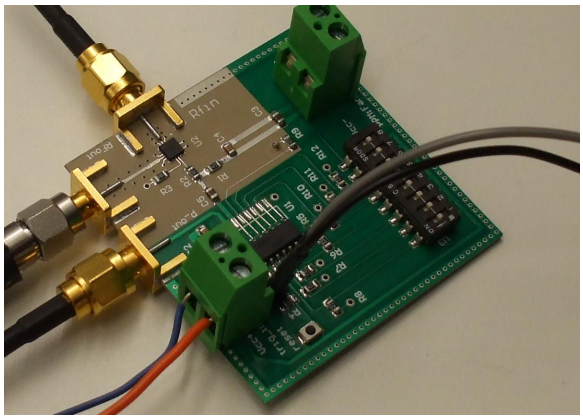

Figure 4.5: The pulse generator. The upper left area is the RF switch and peripheral circuits. Silkscreen was voided to keep the impedance calculation simple.

Since the bandwidth is the most limiting factor, the system design process mainly focuses on meeting this requirement. For the transmitter, a pulse generator was designed and tested as shown in Fig. 4.5. The board is a RF-digital mixed design. A Single Pole Double Throw (SPDT) RF switch is used to generate the pulse at 10.5 GHz, with one output terminated. The path between the driver input of the RF switch and the digital pulse generator output was kept short to maintain the signal integrity. Fig. 4.6 shows the time-domain test result. The edges of the pulse are well preserved. However, the isolation of the switch output in the test is only 20 dB, which is much lower than expected. The leakage in the transmitter idol period will result in active interference. Therefore, the commercial off-the-shelf RF switch module HMC-C019 was used in the final design. The test result is shown in Fig. 4.7.

As for the receiver, LNA with low inter-modulations are selected to reduce the interference within the bandwidth. Direct conversion is used instead of the more sophisticated super-heterodyne design. Converting signal directly to baseband quadratically can save half of the sampling rate with the expense of doubling the digitizing channels. With the dual-pol expansion, a total of four channels are needed at the digital end. The system block diagram of the transceiver is shown in Fig. 4.8.

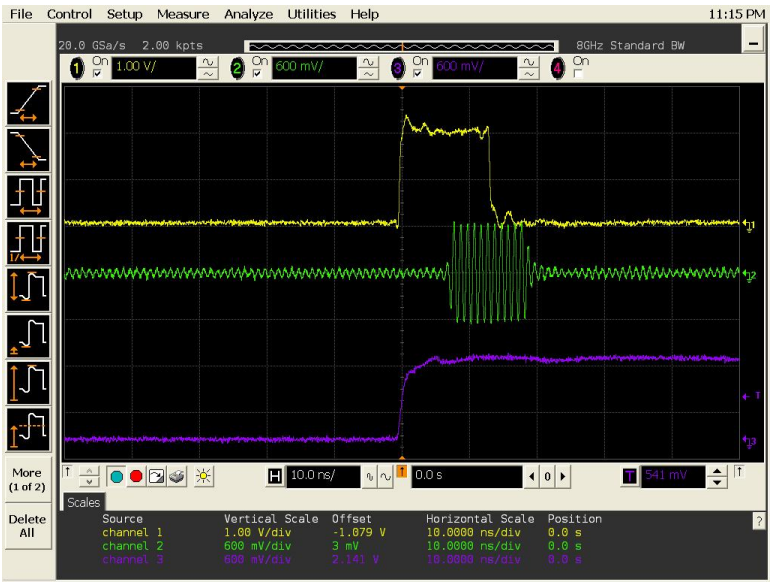

Figure 4.6: Test measurement of the self-designed pulse generator. Yellow is the driving pulse approximately 12 ns wide. Green is the output of the switch. And purple is trigger for the pulse generator.

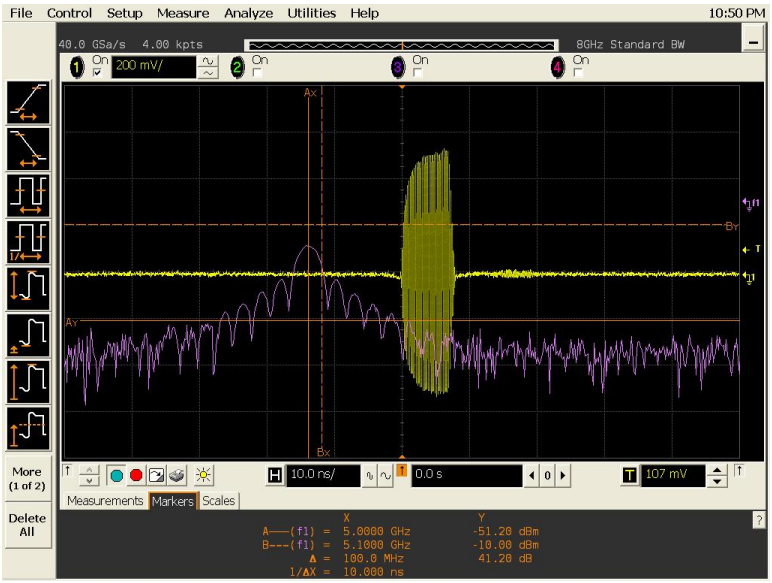

Figure 4.7: Test measurement of the commercial RF switch module. Yellow is output waveform in the time domain and purple is the corresponding Fourier transform. The test was performed at 5 GHz instead of 10.5 GHz as the oscilloscope only supports up to 8 GHz sampling.

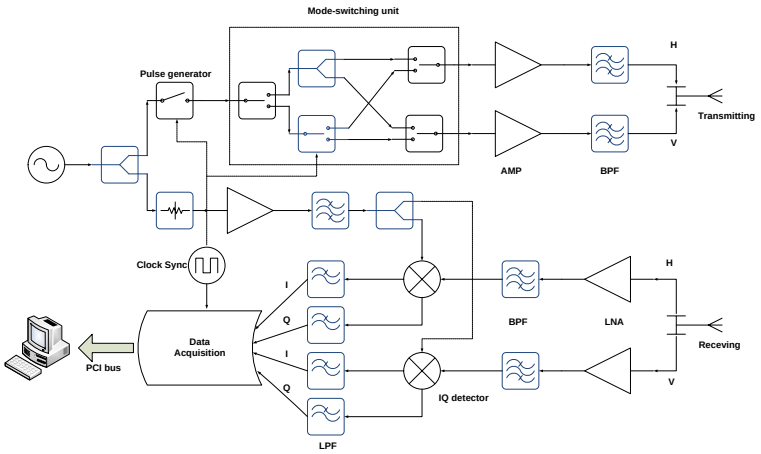

Figure 4.8: Block diagram of the scatterometer transceiver. Notice because the direct-conversion architecture, four channels are required to digitize the baseband signal.

A switching module consisting RF switches and dividers is inserted into the transmit chain. The module is designed for selecting polarization mode from single-pol H, single pol V, simultaneous dual-pol and alternative dual-pol. The alternative dual-pol mode interleaves H and V polarization from pulse to pulse as illustrated in Fig. 4.9, while in simultaneous dual-pol mode, pulses of both polarization are transmitted at the same time.

The scatterometer must be phase-coherent to make valid Doppler measurements. Therefore, all digital signal in the system needs to be synchronized to avoid sampling jitter. As illustrated by Fig. 4.10, $t0$ is when the Digital Acquisition Unit (DAU) is triggered, $t1$ and $t2$ are when the AD converter actually starts sampling after being triggered by consecutive pulses. If the trigger clock is not synchronized with the sampling clock, the actual sampling time could be off by a jitter $\delta t = t2 - t1$ from pulse to pulse, which may lead to invalid Doppler measurements. The clock synchronization board shown in Fig. 4.11 was thus designed to generate trigger clocks from the sampling clock, which keeps all digital clocks synchronized. The opened transceiver case is shown in Fig. 4.12. A part list for all RF components used can be

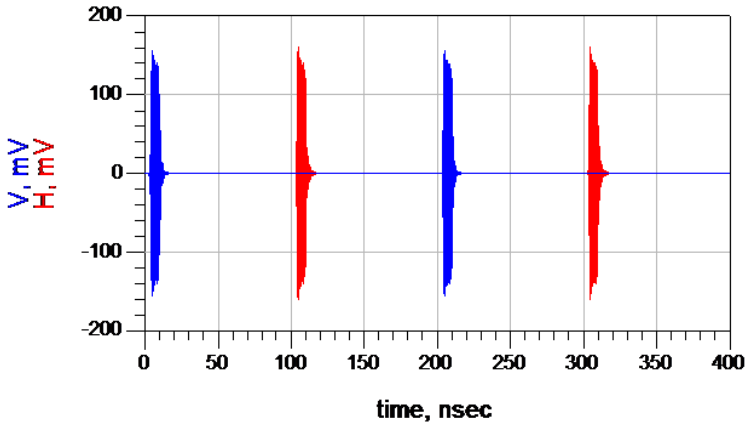

Figure 4.9: Demonstration of transmitting in alternative dual-pol mode from pulse to pulse. A low duty cycle is used for demonstration only.

found in Table A.1. Because most of the RF components have to be customized, the overall cost of the transceiver takes more than half of the entire scattometer budget.

The digitizer for the scatterometer is a commercial data acquisition card Razor CompuScope 1642 from GaGe, which has 4 channels, 200 MS/s maximum sampling rate and 16-bit resolution. Sampled data are buffered into the on-board memory, and the sampling is stalled when pulling the data out from the memory, which is inefficient for real-time measuring with frequent data reading. However, the board comes with a large memory of 256 MB, sufficient for most indoor measurements that last not too long. The analog inputs are 50 omhs, ensuring impedance matching with the transceiver outputs. The sampling clock is fed to the clock synchronization board, which generates the trigger signal for the card. The card has a small form factor that can be connected to a PCI slot in the host computer.

4.5 IQ Imbalance Calibration

The output IQ signal should be equal-amplitude and orthogonal in theory as they are down converted from the same input quadratically. However, uneven gain and phase

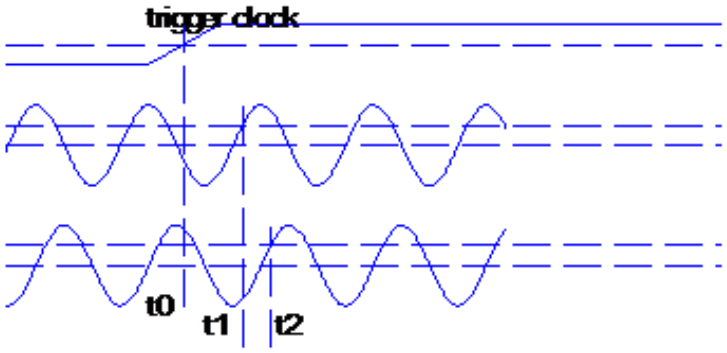

Figure 4.10: Jitter caused by misalignment of the trigger clock with the sampling clock. Without loss of generality, the trigger levels is set to 50% of the clock amplitude.The first sample after the trigger occur at different time because of the asynchronism of the trigger and the sampling clock.

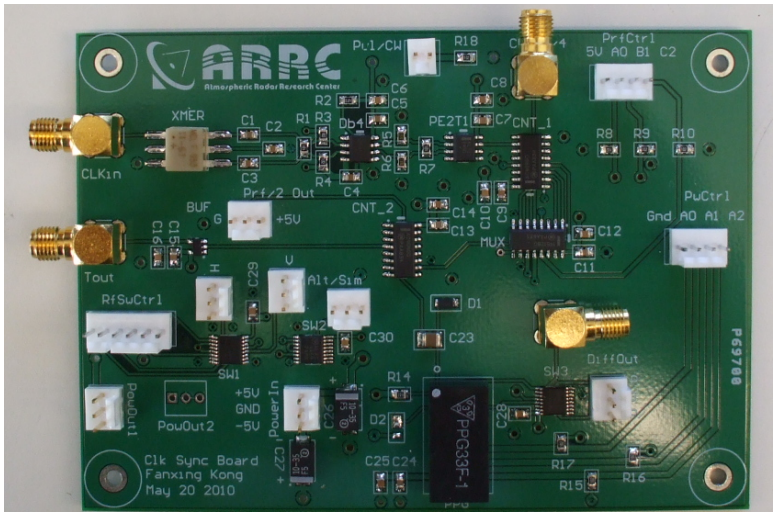

Figure 4.11: The clock synchronization board. In addition to synchronization, the control modules for configuring the PRF, pulse width, and polarization mode are all integrated on this board.

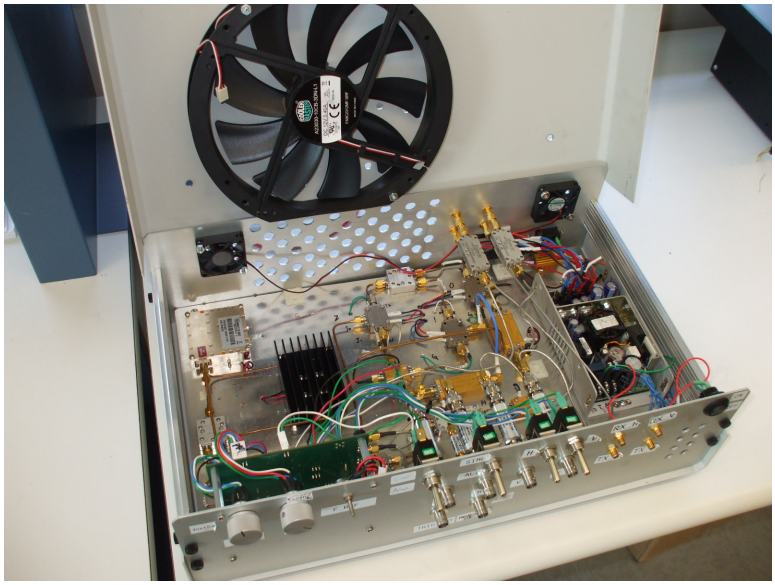

Figure 4.12: The scatterometer transceiver box. All RF components except the antennas are in this case. The synchronization board is wired to the front panel switches for reconfiguring the system.

distortion in the analog down-conversion chain can lead to imbalanced IQ outputs, which will cause spurious spectra components. For a pulse Doppler radar, it is critical to ensure the accuracy of spectrum estimate. Thus, the IQ imbalance needs to be calibrated.

Two methods were developed for this calibration. The first one is by signal processing without involvement of additional hardwares. Using the inphase channel as reference, the distorted quadrature output can be modeled:

$$Q_m = Q + \alpha I \tag{4.7}$$

where Q_m and Q are the measured and true quadrature output. α is a constant projection coefficient. I and Q are orthogonal as:

$$< I, Q >= 0 \tag{4.8}$$

Substituting Q_m into the above equation:

$$< I, Q_m - \alpha I >=< I, Q_m > - < I, \alpha I >=< I, Q_m > -\alpha < I, I >= 0 \tag{4.9}$$

$$\alpha = \frac{< I, Q_m >}{< I, I >} \tag{4.10}$$

The advantage of this method is that it does not require additional hardware, thus can be implemented from pulse to pulse. So even if the distortion is time-variant, this method is still effective. The other method requires a tone signal, which has a small frequency offset from the scatterometer operating frequency, yet still in the system bandwidth. The demodulated IQ signal with arbitrary phase and amplitude distortion is:

$$I_m(n) = \alpha cos(\omega n) \ + I_0 \tag{4.11}$$

$$Q_m(n) = \beta \sin(\omega n + \phi) \ + Q_0 \tag{4.12}$$

where I_0 and Q_0 are the DC offset in each channel, α and β are the amplitude of I and Q, ϕ is the phase offset and I_0 and Q_0 are the amplitude offset. The 1^{st} and 2^{nd} moment and the cross correlation coefficient of the measured signal are:

$$M_I(1) =< I_m(n) > = \ \alpha < cos(\omega n) \ > + I_0 = I_0 \tag{4.13}$$

$$M_Q(1) =< Q_m(n) >= \beta < \sin(\omega n + \phi) \ > + Q_0 = Q_0 \tag{4.14}$$

$$M_I(2) =< (I_m(n) - I_0)^2 >=< \alpha^2 \cos^2 \omega n >= \alpha^2 < \frac{1 + cos2\omega n}{2} >= \frac{\alpha^2}{2} \tag{4.15}$$

$$M_Q(2) =< (Q_m(n) - Q_0)^2 >= \beta^2 < \sin^2(\omega n + \phi) \ >= \frac{\beta^2}{2} \tag{4.16}$$

$$C_{IQ} = \frac{< (I_m(n) - I_0)(Q_m(n) - Q_0) >}{\sqrt{<}(I_m(n) - I_0)^2 > \sqrt{<}(Q_m(n) - Q_0)^2 >} = \sin(\phi) \tag{4.17}$$

The moments and cross correlation coefficient can be estimated from measurements. Thus, the estimates for amplitude offset, amplitude ratio and phase offset are :

$$\hat{I}_0 = \hat{M}_I(1) \tag{4.18}$$

$$\hat{Q}_0 = \hat{M}_Q(1) \tag{4.19}$$

$$\widehat{\alpha} = \sqrt{2\hat{M}_I(2)} \tag{4.20}$$

$$\widehat{\beta} = \sqrt{2\hat{M}_Q(2)} \tag{4.21}$$

$$\hat{\sin}(\phi) = \hat{C}_{IQ} \tag{4.22}$$

$$\hat{\cos}(\phi) = \sqrt{1 - \hat{C}_{IQ}^2} \tag{4.23}$$

The actual IQ signals are equal-amplitude and orthogonal:

$$I(n) = \beta \cos(\omega n) \tag{4.24}$$

$$Q(n) = \beta \sin(\omega n) \tag{4.25}$$

And they can be estimated from the measured signal as:

$$\hat{I}(n) = \frac{\widehat{\beta}}{\widehat{\alpha}} I_m(n) \tag{4.26}$$

$$\hat{Q}(n) = -\frac{\widehat{\beta} \sin \hat{\phi}}{\widehat{\alpha} \cos \hat{\phi}} I_m(n)) + \frac{Q_m(n)}{\cos \hat{\phi}} \tag{4.27}$$

Or in the matrix form:

$$\begin{bmatrix} \hat{I}(n) \\ \hat{Q}(n) \end{bmatrix} = \begin{bmatrix} \frac{\hat{\beta}}{\hat{\alpha}} & 0 \\ -\frac{\hat{\beta}\hat{\sin}\phi}{\hat{\alpha}\hat{\cos}\phi} & \frac{1}{\hat{\cos}\phi} \end{bmatrix} \cdot \begin{bmatrix} I_m(n) \\ Q_m(n) \end{bmatrix} \tag{4.28}$$

Due to the use of external signal source, it is assumed that the distortion is time-invariant, and this calibration is performed only once before the measurement. However, because all parts are passive after the mixer stage, the imbalance can be considered as constant phase and amplitude offset. The time-invariant is therefore a valid assumption.

An example of the down converted IQ of a single-tone test signal is shown in Fig. 4.13, where I and Q are obviously imbalanced. Using the second method, the calibrated IQ signal is shown in Fig. 4.14. After the calibration, the I and Q are well balanced with equal amplitude and 90° phase difference. In Fig. 4.15, the imbalanced signal has spurious spectral components at zero and the image frequency. After the calibration, both are eliminated. The IQ imbalance calibration is a necessary step in any receivers with analog quadratic mixing stage.

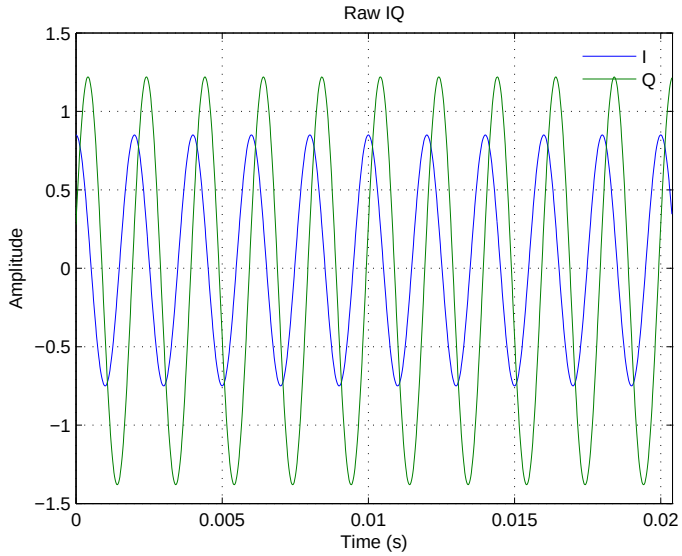

Figure 4.13: Imbalanced IQ of the test single-tone signal. The amplitude ratio $\alpha/\beta = 0.62$. The amplitude offset $I_0 - Q_0 = 0.13$. And the Q channel has a phase advance over I of $30°$.

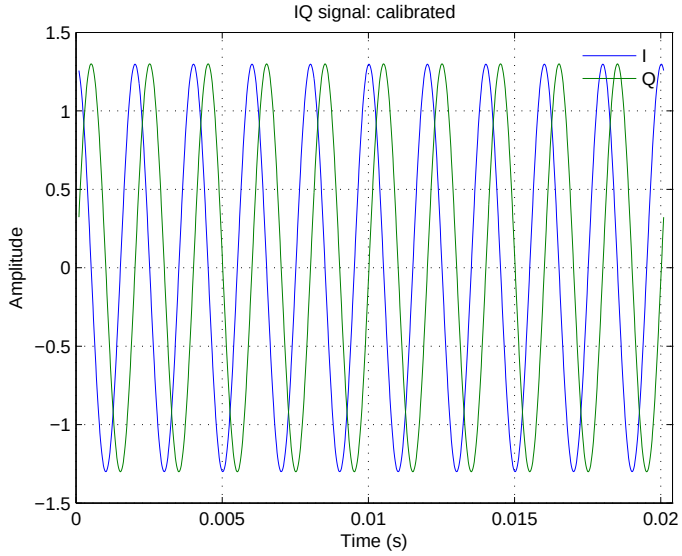

Figure 4.14: The calibrated IQ signals have the same amplitude and are orthogonal as the phase difference is $\pi/4$.

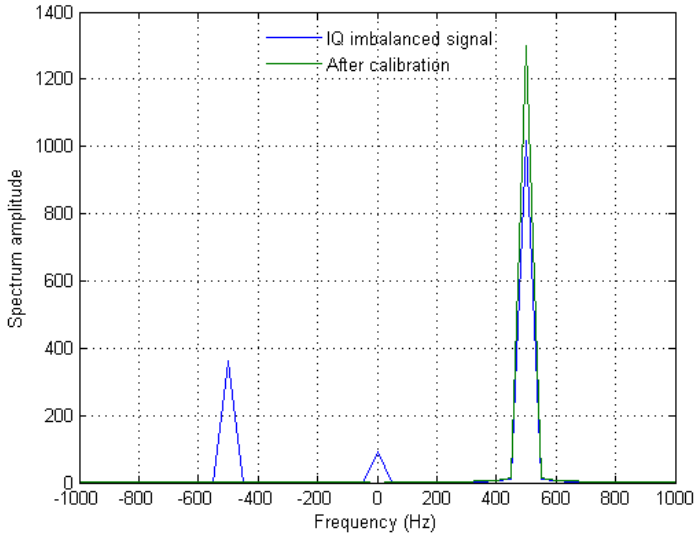

Figure 4.15: Spectrum estimates from the IQ signal before and after calibration. The spurious images are suppressed by calibration.

4.6 Frequency Domain Measurement

The frequency domain measurements were made using the Agilent VNA $E8364B$, which is a powerful instrument working up to 50 GHz. Our measurements are implemented at two frequency bands: X and Ka. The VNA is configured to measure in stepped frequency mode, where single-tone measurements were made at each frequency step. The rotor blade of the wind turbine model increments a small angle after the data of each frequency sweep are saved. A complete revolution of the blade rotation was measured. Thus, the data is two dimensional, one of which is the blade position, the other is the measuring frequency as illustrated in Fig. 4.16. The frequency dimension is converted to time/range by Inverse Fourier Transform (IFT), where the time series of the return signal from the wind turbine model can be extracted.

Analogous to the fact that the sampling interval in time domain determines the bandwidth in frequency domain, the spacing between frequency steps also determines

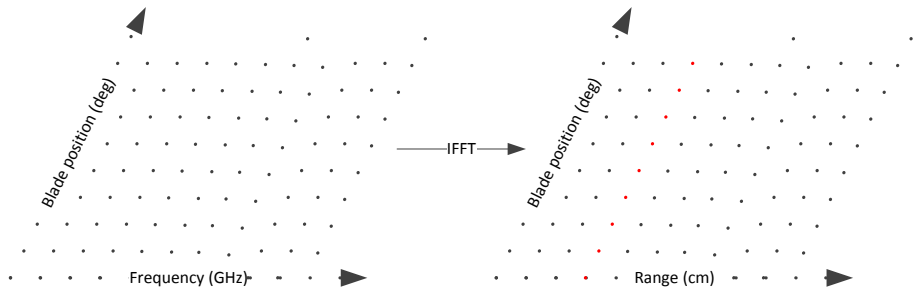

Figure 4.16: Illustration of measuring grids in the frequency domain. The data can be converted to time domain by Fourier transform in the frequency domain.

the time span, or the unambiguous range. The frequency step is 1 MHz in our measurements, which corresponds to 1 μs time span or 150 m unambiguous range, which is obviously sufficient for the size of the anechoic chamber even taking into account the system delay and possible multi-path scattering. The frequency span is equivalent to the bandwidth in time-domain measurements and is set to 200 MHz, which is twice that of the scatterometer. It is intentionally set larger to account for the windowing effect when converting to the time domain.

The measured data at Ka band is shown in Fig. 4.17. The blade may be off from the correct position due to placement error. However it is clear that the return signal has remarkable pattern every 60°. It is also interesting to see that the wind turbine model seems to have frequency selection characteristics, as the return signal is obviously weaker near 39.87 GHz and 39.92 GHz. Though this is from only one azimuth aspect and pitch, it may be possible to reduce the returned power of wind turbine by minor shift of radar operating frequency.

Next the frequency-domain measurements need to be converted to time domain as shown in Fig. 4.16. The data are windowed along the frequency domain samples and then converted to range by IFT. After the conversion, the data become range profiles of the wind turbine model at different blade positions as shown in Fig. 4.18. Obviously, the brightest line corresponds to the return signal of the wind turbine

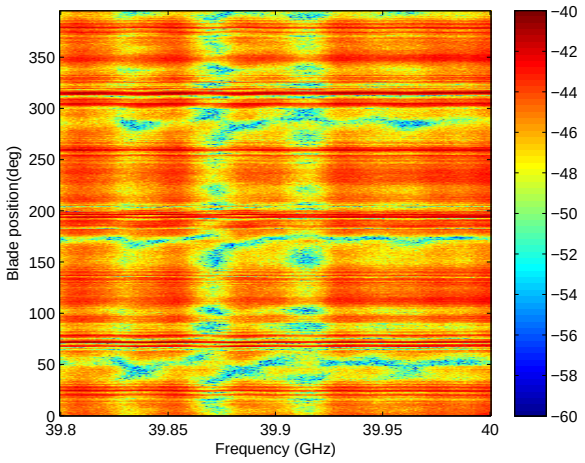

Figure 4.17: Data of frequency measurement in dB at Ka-band. The frequency is centered at 39.9 GHz with 200 MHz span. The blade rotates for approximately 400° during the measurement with 0.5° increment. The azimuth aspect $\phi = 45°$.

model. The data from all blade positions are averaged as shown in Fig. 4.19, where the peak around 600 cm should be from the wind turbine model. Notice it is not exactly where the wind turbine model is located because the reference time zero is actually before the wave is transmitted. The first peak is the direct coupling from the transmitt to receive channel. The peak near 1000 cm is the return from the wall on the back of the chamber. The minor bump after may be due to multi-path scattering.

The return signal of the wind turbine model at different blade position is extracted and shown in Fig. 4.20. The Ka-band and X-band measurement are compared against each other without calibrating the loss difference of the cables and antennas. Therefore, the amplitude difference cannot reflect the frequency selection characteristic. It is interesting to notice that the overall variation of the return signal in terms of changing blade position is similar.

The spectrogram showing the micro-Doppler signature of the wind turbine model at two different frequencies are shown in Fig. 4.21. Because the frequency sweeping is relatively slow, the frequency-domain measurements were actually performed when

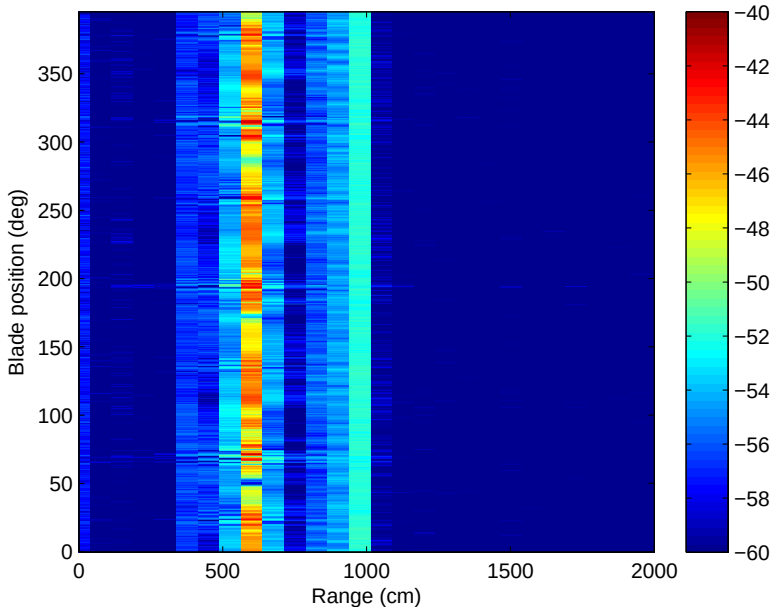

Figure 4.18: Frequency domain data converted to range profiles. Hamming window has been applied in the frequency domain to lowering range sidelobes.

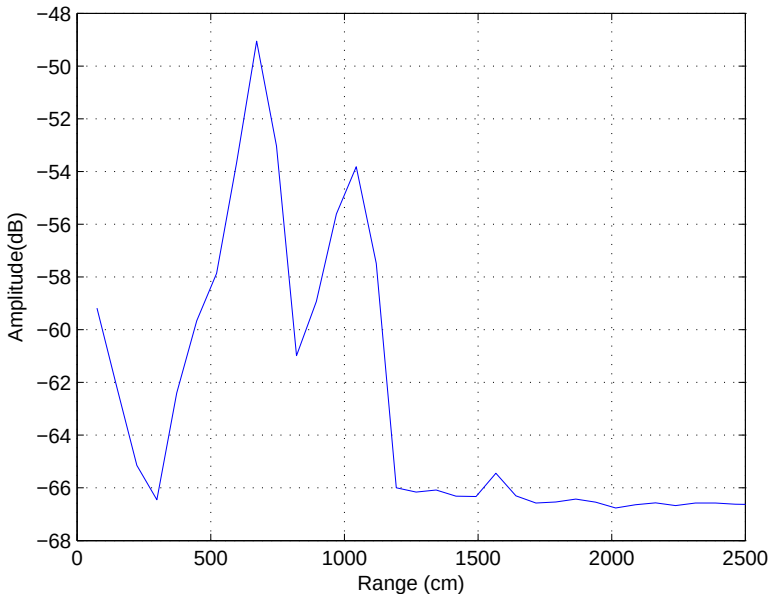

Figure 4.19: The averaged range profile of the VNA measurement. The major contribution to the peak at the wind turbine location is the tower as it is stationary from one measurement to the next.

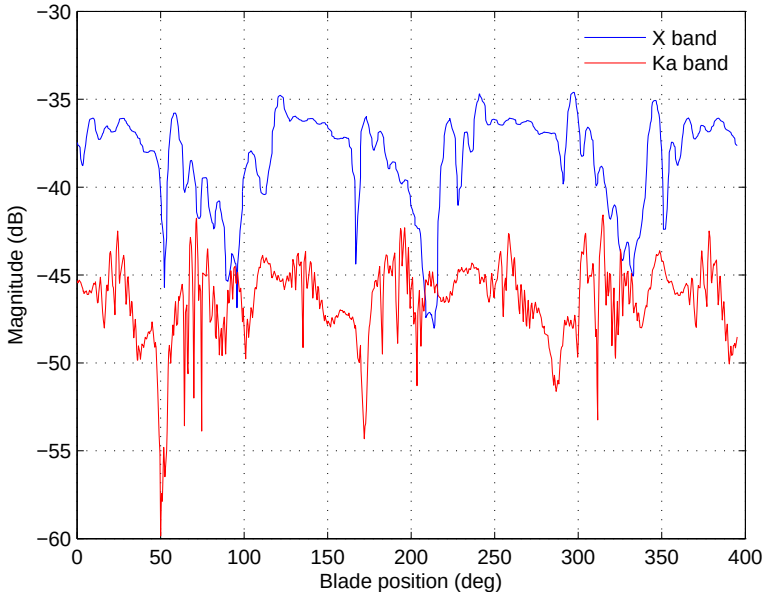

Figure 4.20: The return signal varying with blade position of the wind turbine model using frequency domain measurement. The system gains of antennas, cables, etc. are different for the two measurements.

the rotor blade was stationary. The increment angle is small to avoid ambiguity due to insufficient sampling. Assuming arotating rate of ω, the corresponding PRT is:

$$t_p = \frac{\Delta\theta}{\omega} \tag{4.29}$$

where $\Delta\theta = 0.5^\circ$ is the blade position increment between two consecutive measurements. The ambiguity velocity is:

$$v_a = \frac{\lambda}{4t_p} = \frac{\lambda\omega}{4\Delta\theta} \tag{4.30}$$

The blade tip velocity normalized to v_a is:

$$\overline{v}_{tip} = \frac{D\omega/2}{v_a} = \frac{2D\Delta\theta}{\lambda} \tag{4.31}$$

which is irrelevant to the virtual rotation rate ω. D is the rotor diameter. For example, if the rotation were to become "faster", v_a would increase proportionally. However, the spectrogram is the same except the corresponding velocity axis. In other word, the spectrogram is only determined by the measurement configurations.

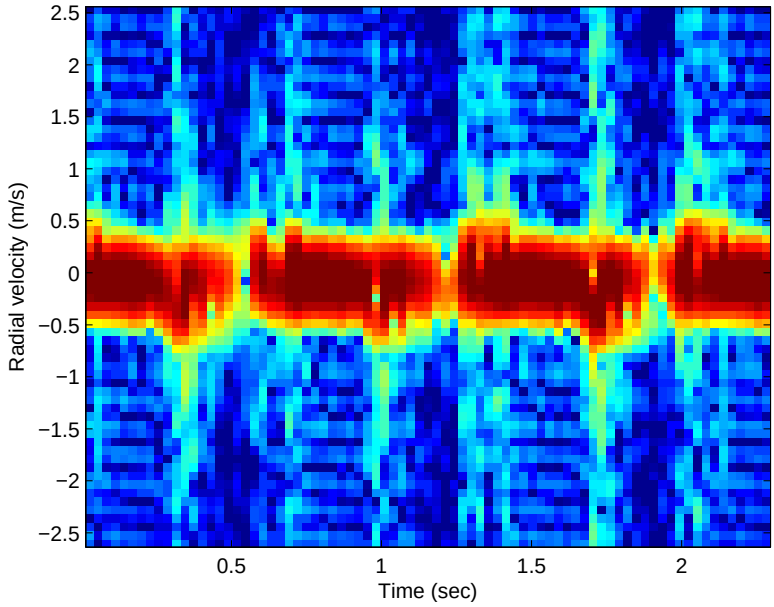

(a)

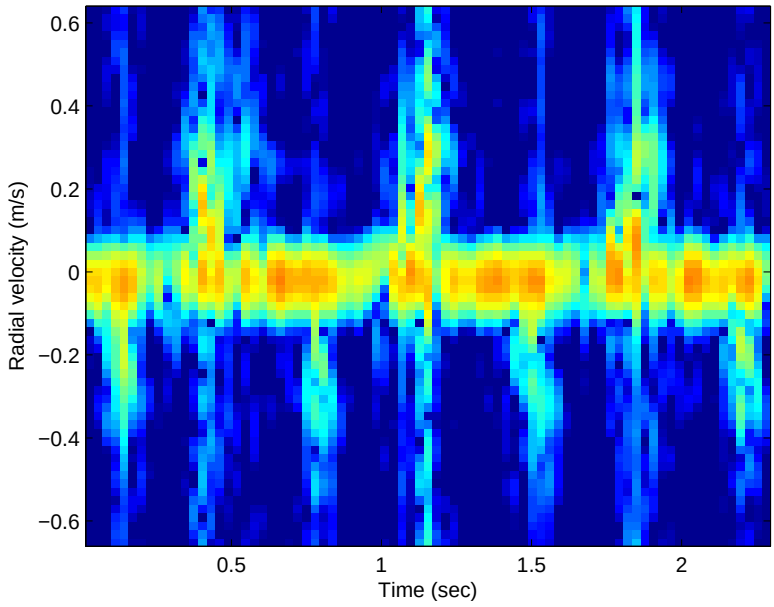

(b)

Figure 4.21: The spectrogram of the wind turbine return signal by frequency-domain measurements: (a) X-band measurement; (b) Ka-band measurement. The aliasing velocity is different as the the wavelength is different. The virtual rotation rate is set to 28.5 rpm.

Because of the oblique incident, the already short blade seems even "shorter" after projecting onto the LOS. In Fig. 4.21 (a), the flashes are so short that they are barely visible. Yet as the wavelength becomes shorter, the flashes extend further and the spectrum seems "finer" in Fig. 4.21 (b). The actual Doppler resolution is determined by the dwell time, which is the same for both measurements. However, the "relative" Doppler resolutions are different. The maximum number of Doppler velocity resolution units within each flash is:

$$N_d = \frac{v_{max}}{\Delta v} = \frac{v_{tip}}{\Delta v} |\sin \phi| \tag{4.32}$$

where v_{max} is the maximum radial velocity, which is v_{tip} projected onto the LOS; Δv is radial velocity resolution and is proportional to the Doppler resolution:

$$\Delta v = \frac{\lambda}{2} \Delta f_d = \frac{\lambda}{2T} \tag{4.33}$$

where Δf_d is the Doppler resolution, T is the temporal resolution of the spectrogram:

$$T = \frac{\Theta}{\omega} \tag{4.34}$$

where Θ is the angle swept by the rotor blade in T. Substituting the tip velocity $v_{tip} = D\omega/2$ into equation (4.32):

$$N_d = \frac{D\Theta}{\lambda} |\sin \phi| \tag{4.35}$$

where N_d is proportional to wavelength. N_d characterizes the fineness of the Doppler spectrum at each flash. The larger N_d is, the more detail can be observed within the flash. For the wind turbine model, in order to match N_d of measuring the full-size wind turbine using WSR-88D radar, a millimeter measurement is needed at over 300 GHz as is shown in Table 4.3.

This relative spectral resolution loss is unavoidable with our hardware limitation. The last column of Table 4.3 gives the difference between N_d of the full-size wind

Table 4.3: Scale comparison of radar and wind turbines

Radar	$f(GHz)$	$D(m)$	D/λ	N_d
WSR-88D	2.7	80	720	126
VNA	up to 40	0.7	93	16
Scatterometer	10.5	0.7m	25	4
Millimeter radar	308.6	0.7m	720	126

turbine and wind turbine model measurements assuming $\Theta = 10°$. The Doppler spectrum of the scaled measurement is expected to be approximately 30 times coarser than that of the full-size measurements. Nevertheless, it still reveals some interesting features that are different from the WSR-88D full-size wind turbine measurement.

4.7 Time Domain Measurement

The frequency domain approach is limited to stationary measurement due to relatively long measurement cycle of the VNA, i.e., the interval between consecutive measurements. The time needed for measuring all blade and yaw positions is tremendous. Therefore, the scatterometer is used for direct time domain measurement, the setup of which is shown in Fig. 4.22.

Because of the much shorter cycle time, the scatterometer is able to continuously sample the return signal while the blade is rotating. The measurement was thus carried out in the sequence of stop-spin-sample-go. The blade rotates for a complete revolution at each aspect angle ϕ, while the radar keeps sampling, and then stops and yaws to the next yaw position $\phi + \delta\phi$ until it turns back to the initial position. The return signal power of the wind turbine model with incrementing blade position by both the frequency-domain and time-domain measurements are compared in

Figure 4.22: Time domain measurement setup. The bottom of the wind turbine model is covered to reduce scattering from the base. The monitor shows the software user interface developed using LabVIEW.

Fig. 4.23, which closely match each other. However, the time needed to perform the measurement is significantly reduced in the time-domain measurement. A direct comparison of the time required to perform each measurement is listed in Table 4.4. The PRF of the scatterometer is set to 1515 Hz and the blade rotation rate is 20 rpm. The yaw increment $\delta\phi = 1^\circ$ for both cases, while $\delta\theta$ is much finer for the time-domain measurement. Most importantly, the wind turbine model can now be measured for all blade positions and aspect angles within a realistic time frame.

Table 4.4: Time required for frequency and time domain measurements

	Cycle time	**Single revolution**	**All rotation and yaw**
Frequency domain	2.24 sec	56 min	14 days
Time domain	0.66 ms	3 sec	18 min

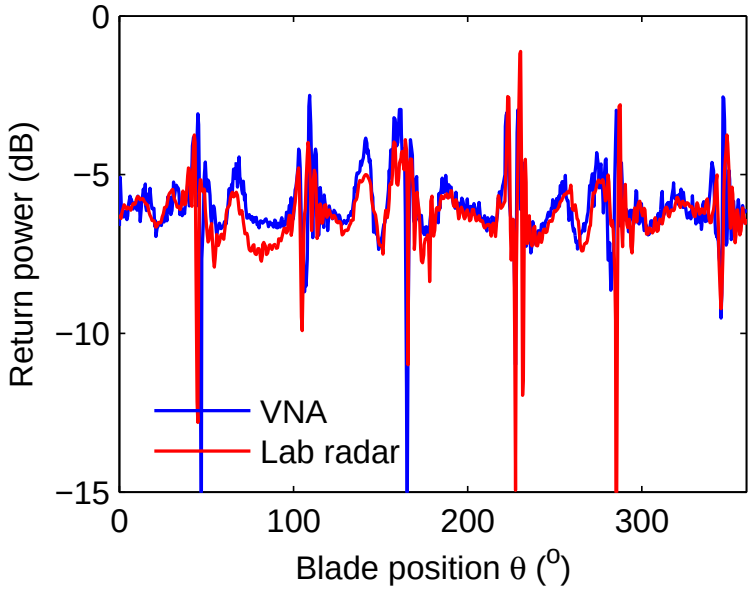

Figure 4.23: Comparison of the return power of wind turbine model. Notice, the measured results are not exactly aligned with the actual blade position.

Examples of the Doppler spectrum of wind turbine model by time-domain measurement are shown in Fig. 4.24. The flashes occur when one of the blades is perpendicular to the radar LOS, and θ becomes multiple times of 60°, which is consistent with previous EM characterization. In addition these Doppler flashes are at the same positions as the return power peaks in Fig. 4.23, where both the spectrum width and the RCS reach maximum at the same time. When the blade is perpendicular to the radar LOS, aligned with the tower, it is believed that such alignment leads to constructive in-phase coherent integration of backscattered EM field and causes high return power. Because the blade rotation quickly breaks the in-phase lineup, scattering centers having range shifting in scales comparable to radar wavelength will cause significant oscillations due to coherent integration, the peak drops rapidly and starts oscillating.

The sinusoidal trajectory in Fig. 4.24 (a) correspond to the tip of the blade, which is consistent with both the EM simulation and the RaXPol measurement. It is

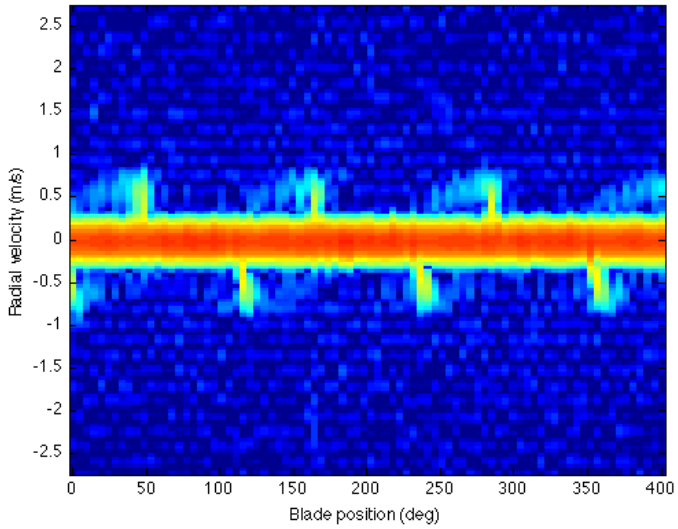

(a)

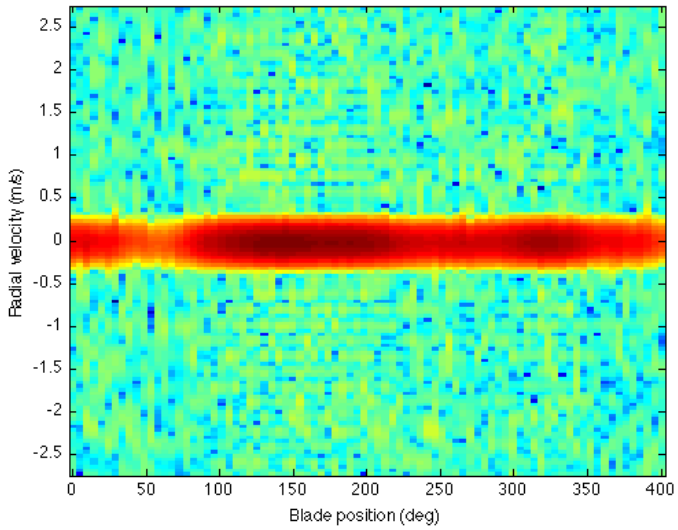

(b)

Figure 4.24: Doppler spectrum of the scaled wind turbine model from the time-domain measurement: (a) $\phi = 90°$. The rotation plane is parallel to the radar beam, (b) $\phi = 0°$. The rotation plane is facing to the radar beam.

worth noting that the flashes corresponding to the leading edge occur almost exactly at integral number of 60°, but earlier for peaks caused by the trailing edge. This phase difference is approximately the same as the blade angle α because the trailing edges turn to vertical earlier as a result of the blade shape. Fig. 4.24 (b) shows the spectrogram of the wind turbine model as it yaws to $\phi = 0°$, when the rotation plane is perpendicular to the radar LOS. At this position, theoretically, if the incident field is plane wave, the return is constant as the blade rotates, but there will be some slow variations in reality due to near-field effect. Hence, the spectrogram only has a horizontal centerpiece but no flashes. In this case, the wind turbine is equivalent to stationary ground clutter and can be mitigated by conventional ground clutter filtering techniques.

The return power variation of vertical and horizontal polarization in terms of the rotation and yaw is shown in Fig. 4.25. As the blade rotates for one revolution, 6 significant peaks are observed at most aspect angles except at $\phi = 0°$ and 180°, when the blade rotation plane is perpendicular to the radar LOS. As ϕ approaches 0° and 180°, the specular reflection from the front/back of blade starts to dominate, thus the two peaks corresponding to edge diffraction merge into one. As a result of the asymmetric blade structure, the return power is not symmetric about $\phi = 180°$. In fact, an arbitrary point on the blade passing through the vertical position above the nacelle at (θ, ϕ) will pass vertically below the nacelle at $(\theta - 60°, 360° - \phi)$.

The periodicity of rotation fluctuation can be used to distinguish wind turbines from desired targets. However, the dwell time during which the wind turbine is continuously illuminated needs to be long enough to observe this periodicity, which is impractical for current scanning radar operations. Assuming the wind turbine is far from the radar and the azimuth dimension of the wind turbine is much smaller than the radar beam width, the swept angle of the rotor blade within the dwell time is:

$$\Theta = \omega \frac{\Psi}{\Omega} \tag{4.36}$$

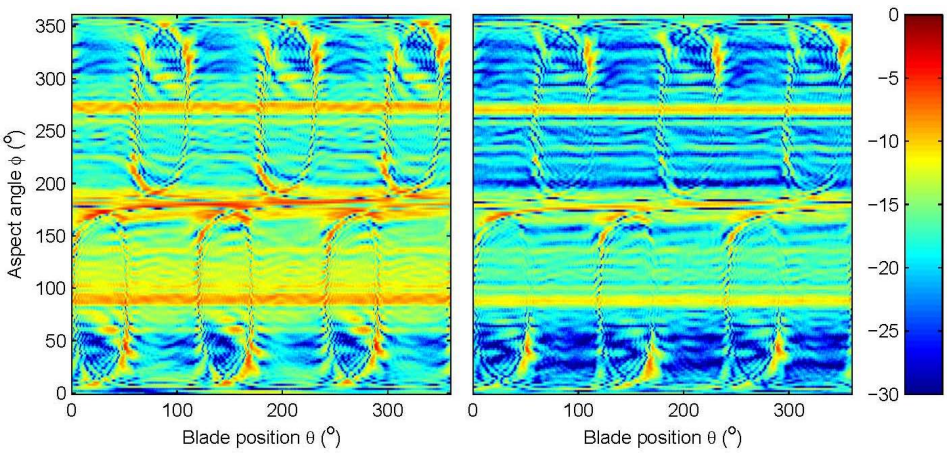

Figure 4.25: Measured radar return power variation of the wind turbine model in terms of blade position and aspect angle. Left is vertical polarization, right is the horizontal polarization.

where Ψ is antenna beam width and Ω is radar scan rate. For example, if the wind turbine spins at 15 rpm and the radar scans at $18°/s$ with $1°$ beam width, then $\Theta = 5°$. With such a short observation window, the wind turbine model returns are found to have diverse statistics from scan to scan as is shown in Fig. 4.26. The short-time mean varies as the blade rotates, indicating the statistical non-stationarity. The variance is exceptionally higher due to the fast oscillation where the return power peaks occur. This large variance is one of the radar signatures that can help identify wind turbines. With large variance, the decorrrelation time at such positions are expected to be lower as is shown in Fig. 4.26 (c). In fact, less than $0.5°$ decorrelation angle is observed at these positions.

Many large modern wind turbines have a variable rotation rate, so it is reasonable to assume uniformly distributed random blade position. The statistics of the rotation fluctuation thus characterizes the yaw fluctuation since the latter is the slow variation over a relatively long time. The mean and standard deviation of the return power in terms of aspect angle are shown in Fig. 4.27. The mean power has three major peaks at $\phi = 90°, 180°, 270°$, which correspond to the three aspect positions shown in Fig. 4.27.

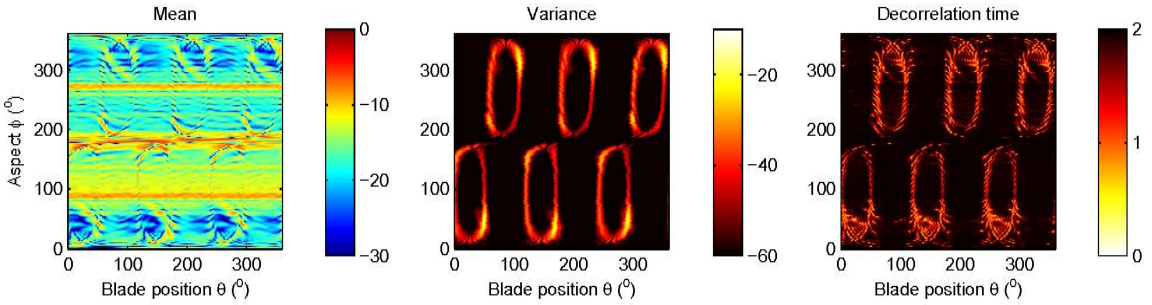

Figure 4.26: Short-time statistics in terms of rotation and yaw: (a) short-time mean in dB, (b) short-time variance in dB, (c) decorrelation time in terms of blade rotation (degrees) corresponding to where correlation coefficient drops to $e^{-\frac{1}{2}}$. All statistics are calculated coherently within a sliding window of 5°.

As the wind turbine yaws to 90° and 270°, one side of the nacelle is perpendicular to the radar LOS, resulting in specular reflections, which causes the mean return power to rise. The peak at $\phi = 180°$, however, is caused by specular reflection from the back of the nacelle. The standard deviation is also maximized at $\phi = 180°$, which can be attributed to the reflection from the backside of the blades. Therefore, the dominant scattering mechanism is specular reflection and proper design of the nacelle shape reducing normal incidence may suppress the interference to radars.

Due to the blade rotation, the return power of a wind turbine fluctuates from pulse to pulse. It is therefore necessary to model the Probability Density Function (PDF) of the return power fluctuations. Since the aspect angle is determined by the wind direction, which normally varies quickly, it is assumed $\phi = \phi_0 + \Delta\phi$, where $\Delta\phi$ describes the wind direction variation. The measurement PDF estimates $p_m(\sigma)$, along with Rayleigh $p_R(\sigma)$, Swerling IV $p_S(\sigma)$ and Gamma $p_G(\sigma)$ fittings are shown in Fig. 4.28. The mode, corresponding to the peak of the PDF, along with the

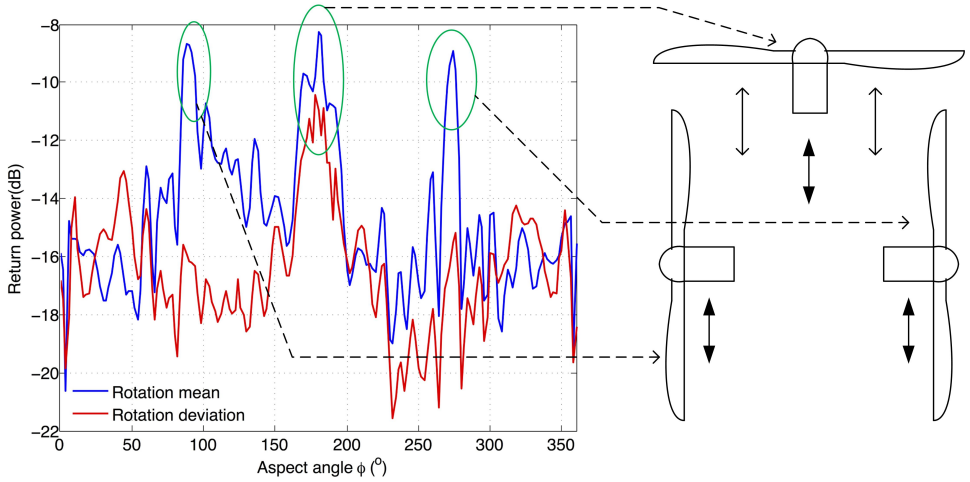

Figure 4.27: Mean and standard deviation of the return power in terms of aspect angle ϕ: both the mean and standard deviation at each aspect angle are estimated across one complete revolution.

Root Mean Square Error (RMSE) are given in Fig. 4.29 (a) and (b), respectively, for comparison. The RMSE is defined as:

$$e = \sqrt{\frac{1}{\Sigma}\int_0^{\Sigma} |p_m(\sigma) - p_f(\sigma)|^2 \, d\sigma} \tag{4.37}$$

where Σ is the dynamic range of measured return power, $p_m(\sigma)$ and $p_f(\sigma)$ are the measured and fitted distribution, respectively. Both Rayleigh and Swerling IV are single-parameter distributions and are given in the following equations, where $\overline{\sigma}$ is the mean.

$$p_R(\sigma) = \frac{4\sigma}{\overline{\sigma}^2} e^{-\frac{2\sigma}{\overline{\sigma}}} \tag{4.38}$$

$$p_S(\sigma) = \frac{2\sigma}{\overline{\sigma}} e^{-\frac{\sigma^2}{\overline{\sigma}}} \tag{4.39}$$

$$p_G(\sigma) = \frac{\sigma^{k-1}}{\Gamma(k)\theta^k} e^{-\frac{\sigma}{\overline{\sigma}}} \tag{4.40}$$

The Gamma distribution is determined by the shape parameter k and scale parameter θ, where $k > 1$ because of nonzero modes in the measurement distribution. Swerling IV is equivalent to Gamma with $k = 2$. The comparison shows that Gamma

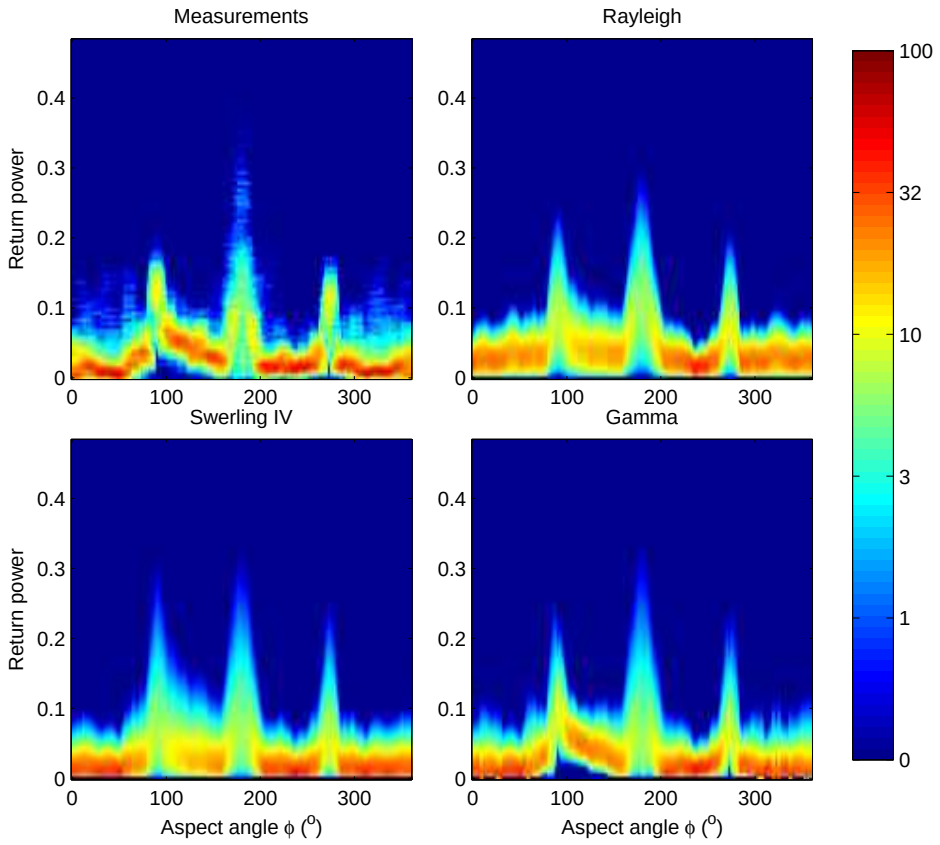

Figure 4.28: Comparison of different PDF fittings, where the probability density is mapped to different colors. The aspect variation $\Delta\phi = 6°$, and the rotation fluctuation samples are decimated by 10 to decorrelate measurements. Maximum likelihood estimation has been used for all fittings.

fitting has the overall best fitting performance. However, when the actual mode of measurements is close to zero, all models have difficulties approximating the actual distribution.

The dual-polarized radar signatures of the wind turbine model have been measured and derived. Stokes parameters are used to describe the polarization state of the wind turbine:

$$Q_{HV} = E_H E_H^* - E_V E_V^* \tag{4.41}$$

$$U_{HV} = E_H E_V^* + E_V E_H^* \tag{4.42}$$

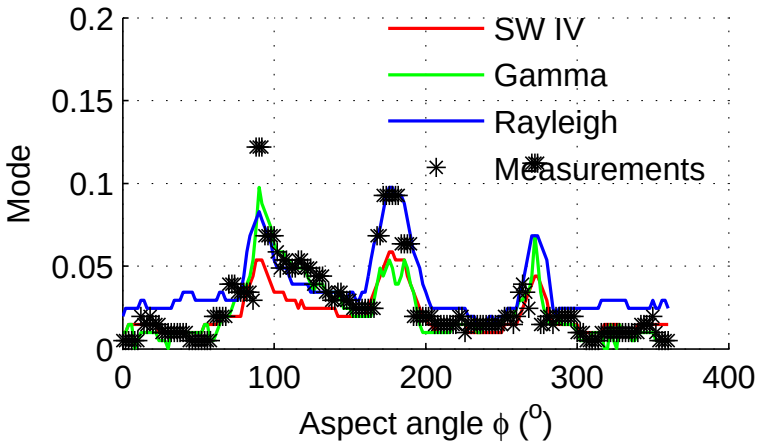

(a)

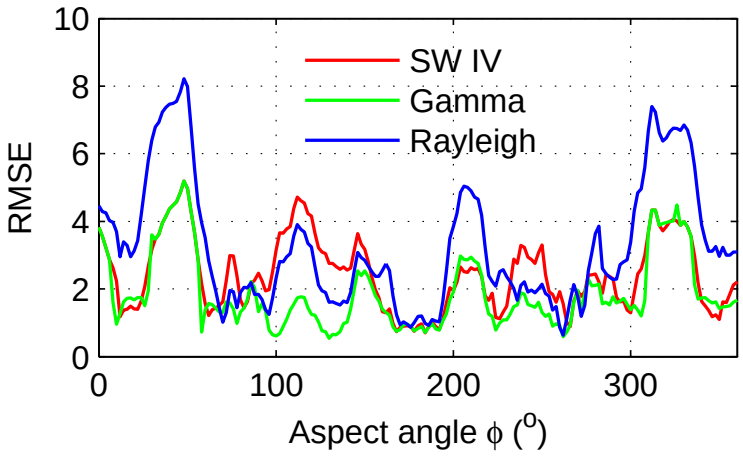

(b)

Figure 4.29: Comparison of different fittings: (a) mode (the value that appears most often), (b) RMSE.

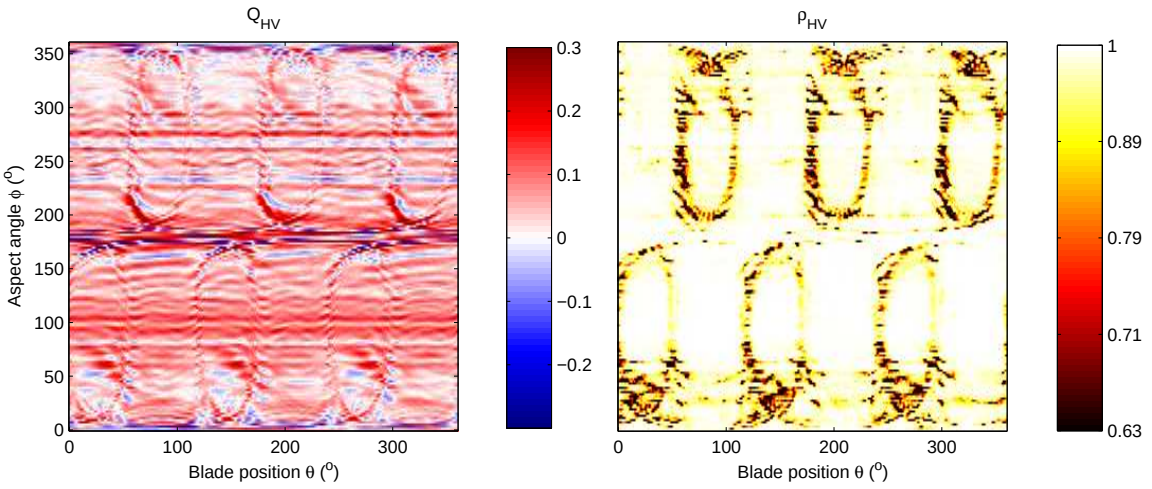

Figure 4.30: Dual-polarized signatures in terms of rotation and yaw. on the left is the degree of polarization Q_{HV}. The cross correlation coefficient ρ_{HV} is on the right. Both have been averaged on an overlapping window of 5°.

$$V_{HV} = -i(E_H E_V^* - E_V E_H^*) \tag{4.43}$$

where E_H and E_V are scattered field in horizontal and vertical polarization, respectively, Q_{HV} is the degree of polarization, U_{HV} and V_{HV} are the shape parameters of the polarization ellipse, from which the cross correlation coefficient is derived:

$$\rho_{HV} = \frac{\sqrt{U_{HV}^2 + V_{HV}^2}}{2|E_H E_V^*|} \tag{4.44}$$

The cross correlation coefficient ρ_{HV} is a normalized measure of the correlation between HH and VV polarization states.

Q_{HV} and ρ_{HV} derived from the time domain measurements are shown in Fig. 4.30. Because VV measurements are much higher than HH. As a result, Q_{HV} is found to be less than zero for most blade and yaw positions, indicating that a horizontal polarized radar may be less susceptible to wind turbine interference. The cross-correlation coefficient shows similar periodicity as the return power variation. It is interesting to notice that ρ_{HV} has relatively low values at positions where the the Doppler flashes occur, which could be a result of scattering phase difference.

Chapter 5

Mitigation of Wind Turbine Clutter for Weather Radar

5.1 Telemetry Based Mitigation

Modern utility scale wind turbines are equipped with multiple embedded sensors, monitoring various operating status, such as the wind direction and speed at the hub height, the rotation rate of the blade, the yaw counting, etc. If this information can be sent to radar operators in real time, and if a large database of the radar IQ signal of the wind turbines being observed is available, then it is possible to mitigate the wind turbine signal by a set of signal processing techniques that will be discussed in the following.

First, a database of IQ signal of the wind turbine needs to be established. Ideally, all factors affecting the wind turbine radar return should be considered, such as the blade rotation, yaw, pitch, and incident elevation angle. Since the elevation angle can be considered as a constant rotation phase shift, the blade position, yaw and pitch variations need to be included in the database. To reduce the computational complexity in this study, it is assumed that the pitch is always precisely known by telemetry. The aspect angle may come with a bias as in reality, a small difference may exist between the rotation axis and the wind direction. However, this is usually within 1°. Therefore, the correct aspect angle is assumed known as well in the following.

The parameters that need to be transmitted are pitch, wind direction, and blade rotation rate. With the wind direction, the azimuth aspect angle of the rotation axis with respect to the radar LOS can be derived, assuming the rotor blades always face

into the wind. Rotation rate allows us to convert the sampling interval in seconds to the actual angle separation in degrees and interpolate the database to appropriate grids. In the following studies, the database of the wind turbine model IQ signal for different azimuth aspect and blade position are acquired from the time domain scaled measurements. The same pitch and rotation rate in real-time signal and the database are used for simplicity and will demonstrate the mitigation scheme by simulation.

According to the superposition theorem, an additive mixing model of the desired target and WTC is:

$$x(n) = w(n) + s(n) \tag{5.1}$$

where $x(n)$ is the real-time return signal, $s(n)$ is desired weather signal and $w(n)$ is the wind turbine signal. $w(n)$ is a deterministic signal in this context as the aspect, pitch and rotation rate are known. $s(n)$ is Gaussian distributed random process. Given $x(n)$, the first step is to find $w_o(n)$ from the database, which is most "similar" to $x(n)$. The criteria used to evaluate the "similarity" is Maximum Cross Correlation Coefficient (MCCC):

$$\rho_i = \left| \frac{\sum_{n=0}^{N-1} w_i(n) x^*(n)}{\sqrt{\sum_{n=0}^{N-1} |w_i(n)|^2} \sqrt{\sum_{n=0}^{N-1} |x(n)|^2}} \right| \tag{5.2}$$

where N is the number of samples in $x(n)$, ρ_i is the cross correlation coefficient. $w_i(n)$ is a segment of IQ signal from the database, whose corresponding pitch and aspect is the same as the telemetry:

$$w_i(n) = W(n + i, \phi, \psi) \tag{5.3}$$

where ϕ and ψ are the telemetered aspect and pitch, respectively. Since the aspect, pitch and rotation rate are all telemetered, an exhaustive search of the time series in blade rotation dimension is performed based on either of the criteria above and the optimal $w_o(n)$ can be found. Notice the IQ signal has zero mean of the signal as the conventional clutter filter has been applied.

If $w_o(n) = w(n)$, then it can be easily subtracted from $x(n)$ coherently. However, there will be uncertainties due to many minor factors not included into the database, such as the blade vibration due to wind gust, multi-path scattering, AP, etc. According to the Central Limit Theorem, many contributing random factors will result in a Gaussian distributed additive interference term $p(n)$. Since both $p(n)$ and $s(n)$ are Gaussian distributed and they are independent, their sum $I(n) = p(n) + s(n)$ is also Gaussian distributed. When $I(n)$ is large enough, the search may result in erroneous results that are off by a few samples. The Wiener filter is, therefore, used to condition the signal. Assuming the following linear relationship between $w_o(n)$ and $w(n)$:

$$w(n) = \sum_{k=0}^{N-1} b(n-k) w_o(k) \tag{5.4}$$

where $b(n)$ is the filter coefficients. The optimal $b(n)$ is given by the Wiener-Hopff equation [72]:

$$B = R^{-1} Q \tag{5.5}$$

where B is the coefficient vector, R is the covariance matrix estimate of $w_o(n)$ and Q is the cross correlation vector estimate:

$$B = [b_0, b_1, \cdots, b_{N-1}]^T \tag{5.6}$$

$$R = \begin{bmatrix} r(0) & r(1) & \cdots & r(N-1) \\ r(-1) & r(0) & \cdots & r(N-2) \\ \vdots & \vdots & \vdots & \vdots \\ r(2-N) & \cdots & \cdots & r(1) \\ r(1-N) & r(2-N) & \cdots & r(0) \end{bmatrix} \tag{5.7}$$

$$r(n) = \sum_{k=0}^{N-1} w_o^*(k) w_o(k-n) \tag{5.8}$$

$$Q = [q(1), q(2), \cdots, q(N)]^T \tag{5.9}$$

$$q(n) = \sum_{k=0}^{N-1} w_o^*(k) x(n) \tag{5.10}$$

The filtered $w_o(n)$ is the best estimate of $w(n)$ and is subtracted coherently from $x(n)$ to recover $s(n)$:

$$\hat{s}(n) = x(n) - w_o(n) \tag{5.11}$$

A simulation validating this method is implemented as such: a simulated weather signal is added to the lab measured data in real time. The mixed signal is then passed to the processing engine and mitigation is performed dwell by dwell. The database is provided by previously measured wind turbine model data for all aspect angles and blade positions. The spectrogram comparison before and after the mitigation is shown in Fig. 5.1.

The real-time wind turbine model data shown are collected by the time domain scaled measurement. When Doppler flashes occur, WTC has wide spectrum width, and the desired weather signal is most severely contaminated because most of the spectrum is contaminated and it is extremely difficult to eliminate the clutter without aggressively reducing desire signal power by conventional clutter filtering techniques.

The simulation gives SCR improvement of better than 20 dB. It is worth noting, though only weather signals are simulated as the desired target, this mitigation scheme can be applied to any target returns contaminated by WTC in real-time and scan-to-scan basis. This method is also implemented in the real-time RWT^2 system and a video clip of the experiment can be found at ARRC's website [73] $http://arrc.ou.edu/\ fanxing/WTCresearch.html$.

5.2 Adaptive Spectrum Processing

The PSD of weather activities, is usually modeled as Gaussian or multiple-Gaussian. In other words, the radial velocities of precipitation particles cluster around one or several values in the spectrum rather than scattering randomly like white noise. This useful property can be extended to a much larger scale depending on the type of weather phenomena being observed. Furthermore, in a large area, the distribution of

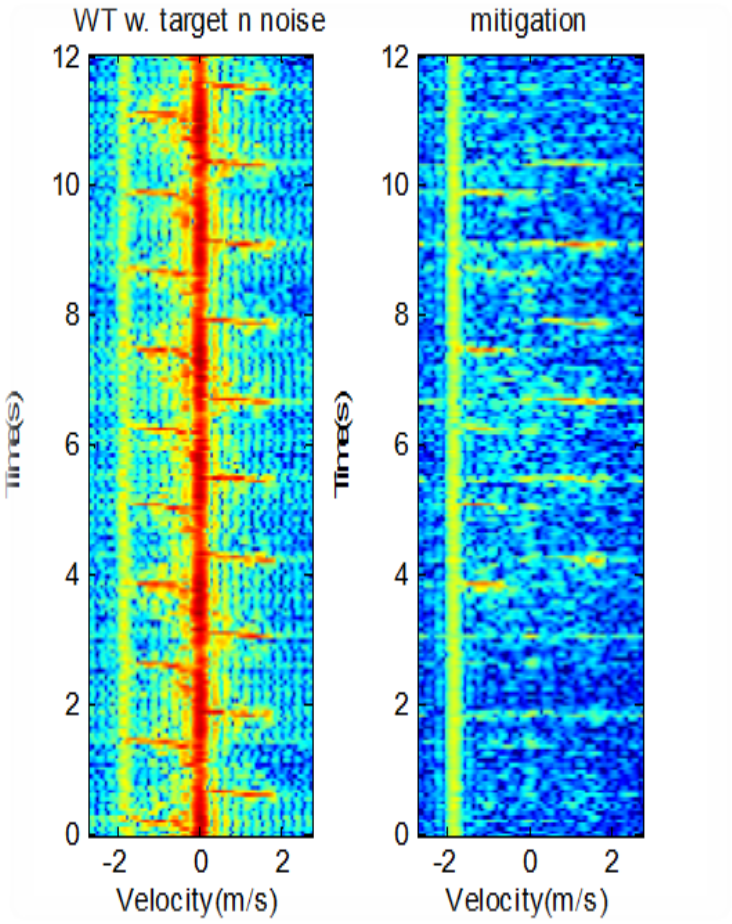

Figure 5.1: Simulations showing the telemetry based mitigation results. From left to right are: simulated weather signal superposed on real-time spotlight-mode wind turbine returns. Although the spotlight-mode data are used to show the mitigation result, the method works on a scan-to-scan basis. The SCR is -10 dB.

the mean radial velocity estimated from all resolution volumes is similar to the PSD of each resolution volume. Therefore, a "bandpass filter" based on the histogram of mean radial velocity can be adaptively generated from the weather observation in and around the wind farm area to filter the WTC contaminated PSD of each resolution volume for moment estimate improvement.

The purpose of Adaptive Spectrum Processing (ASP) is to recover the true moment estimate only when there is confirmed WTC contamination "within" the weather activity of interest. In other words, weather and WTC coexist in the same resolution volume. Therefore, a detection of this coexistence is necessary in order to identify which resolution volume needs to be processed. Detection algorithms [25, 43] can be used for this purpose. In the present study, however, in order to have the true weather moment estimates to evaluate the moment estimate improvement, a simulated data set was made by combining independent IQ signal from the wind farm return and the weather return. Weather and wind turbine coexist in the simulated data if any of the following is true:

$$|z_{xt}(r,\theta) - z_{wx}(r,\theta)| > 3 \tag{5.12}$$

$$|v_{xt}(r,\theta) - v_{wx}(r,\theta)| > 2 \tag{5.13}$$

$$|w_{xt}(r,\theta) - w_{wx}(r,\theta)| > 1 \tag{5.14}$$

where $z_{xt}(r,\theta)$, $v_{xt}(r,\theta)$, $w_{xt}(r,\theta)$ are the reflectivity, mean radial velocity and spectrum width estimate from the simulated *weather + turbine* data at range r and azimuth θ, while $z_{wx}(r,\theta)$, $v_{wx}(r,\theta)$, $w_{wx}(r,\theta)$ are those from the true weather return. In other words, if the difference of reflectivity estimate is more than 3 dB between the mixed data and the true weather data, or if the radial velocity difference is greater than 2 ms^{-1}, or the spectrum width difference is larger than 1 ms^{-1}, then the corresponding resolution volume is considered as weather return corrupted by WTC. It is worth noting that the weather and wind turbine return are assumed to be independent for the mixed data to be valid. They are actually not strictly independent

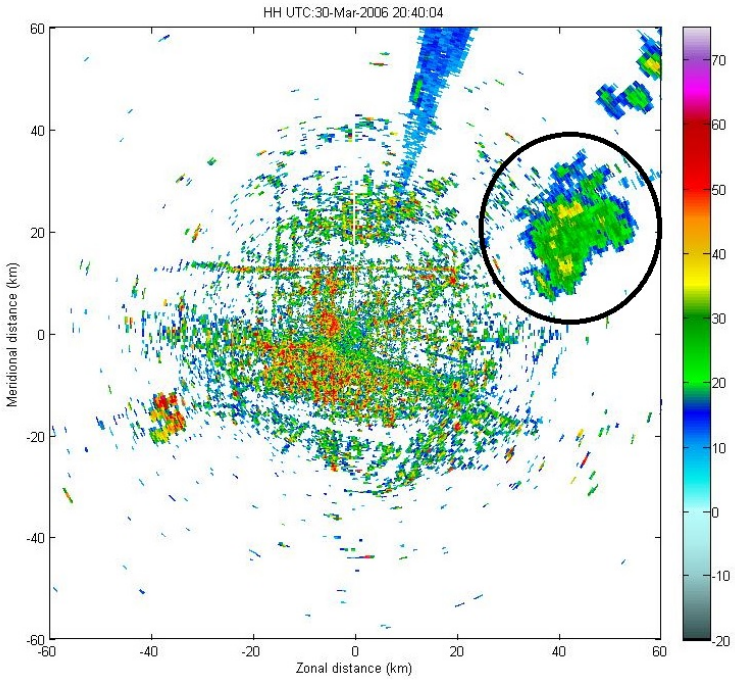

Figure 5.2: Reflectivity of KDDC Level I data without clutter filtering. The Gray County wind farm is on the southwest of the radar featuring high reflectivity, an isolated storm is seen on the northwest moving to the east.

as the wind turbine may shadow the weather that is immediately behind it. It also create a local vortex that may slightly broaden the spectrum width of the weather. However, when the resolution volume is relatively large compared to the size of the wind turbine, these can be neglected.

The Level I data from the KDDC radar featuring the Gray County wind farm is used to generate mixed data of weather and wind turbines. As is shown in Fig. 5.2, an isolated storm moves from the west to east at the northeast of the radar, at approximately the same range as the wind farm. The azimuth, however, is 180° apart. Based on the independent assumption, the wind farm is rotated to the storm location and add the IQ signal together to simulate the scenario of the storm overlapped with the wind farm.

The reflectivity, mean radiao velocity and spectrum width estimate of the rotated wind farm, the weather return and the mixed data are shown in Fig. 5.3. The wind farm has high reflectivity, random radial velocity and wide spectrum bandwidth. The weather return, has a tapered reflectivity profile from the center of the storm to the edge. The mean radial velocity is relatively uniform and the spectrum width is much smaller compared to the wind turbine return. The moments of the weather and wind farm mixed data seem more like the wind farm in the corrupted area.

Though not the case for the Gray County wind farm, but some wind farms have loosely distributed wind turbines, which are spaced relatively far from each another. One reason for this design is to keep the vortex interference between them small so that the overall efficiency is high, but more important, is the terrain requirement. Many wind farms are built on a ridge for better wind conditions. Therefore, the spacing between wind turbines on different ridges can be fairly large. The weather return in between is thus unaffected by the wind turbines, providing clean moment estimates. Sometimes when the wind direction is parallel to the radar LOS, the blades rotate perpendicular to the LOS and the radial velocity is close to zero due to the 90° projection. In this case, the conventional ground clutter filter can effectively mitigate the WTC, resulting moderately contaminated moment estimates. These two cases are generally referred to as "uncontaminated" as along as none of equation (5.12) to (5.14) is met. Therefore, there can be some of these uncontaminated volumes within the wind farm as illustrated by Fig. 5.4.

The mean radial velocity estimates from these uncontaminated volumes can be used as an initial data pool to obtain the PDF of the weather, starting with the uncontaminated volumes inside the wind farm by only counting those in the circumscribed sector of the wind farm. The reflectivity and mean radial velocity estimates of these volumes are shown in Fig. 5.5. There are not many uncontaminated volumes as the wind turbines in this wind farm are very close to each other.

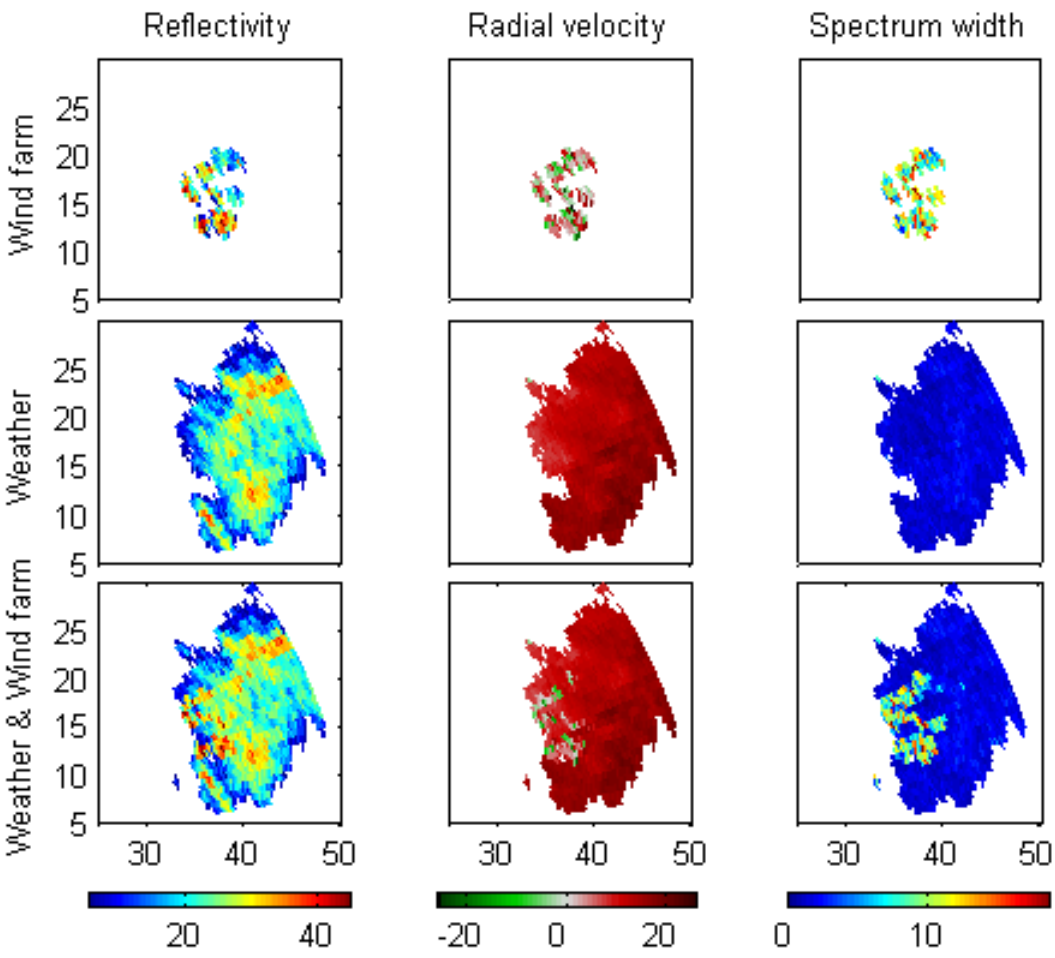

Figure 5.3: Moment estimates from the azimuth rotated wind farm, the weather and the combined data. A high pass filter with a bandwidth of 2.5 ms^{-1} was applied and the filtered power spectrum density was used for moment estimates.

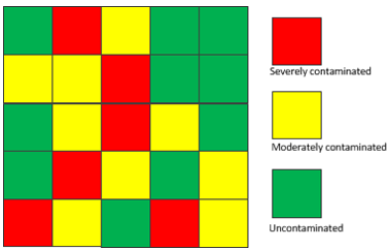

Figure 5.4: An illustration of different levels of contamination within the wind farm area. Both clean (green) and moderately contaminated (yellow) resolution volumes are considered uncontaminated.

Based on this initial data pool, the discrete PDF $p_0(v_r)$ is obtained by counting velocity estimates from each resolution volume and the initial mean radial velocity of the data pool is calculated as:

$$v_0 = \sum v_r p_0(v_r) \tag{5.15}$$

To increase the statistical credibility of the PDF estimate, more samples are needed from such uncontaminated estimates. Therefore, the data pool is expanded in both azimuth and range iteratively based on the following criteria:

$$|v_n - v_{n-1}| < v_{th} \tag{5.16}$$

where v_{th} is the threshold to keep the variation from each iteration small as most weather signal should have similar velocity distribution in close vicinity. If the criteria is not satisfied, the iteration will stop. The final data pool expanded in this case is shown in Fig. 5.6. The evolving of the PDF through iterations is shown in Fig. 5.7. Most of the precipitation is moving away from the radar with a positive radial velocity. The average speed is approximately 15 ms^{-1}.

The PDF from the final iteration is then normalized and used as the frequency response to filter PSD of contaminated resolution volumes. The filtered PSD of contaminated volumes are shown in Fig. 5.8. The weather signal is hardly visible in the

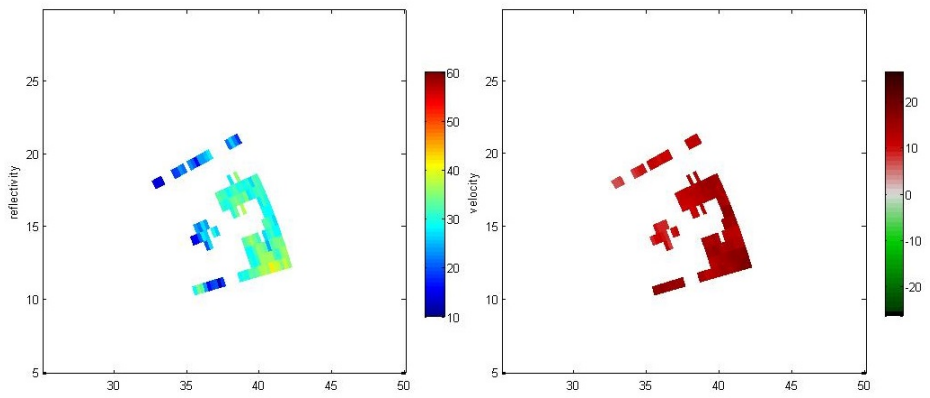

Figure 5.5: The initial data pool used to estimate the PDF of weather in the wind farm area. On the left is the reflectivity estimate, while the mean radial velocity estimate is on the right.

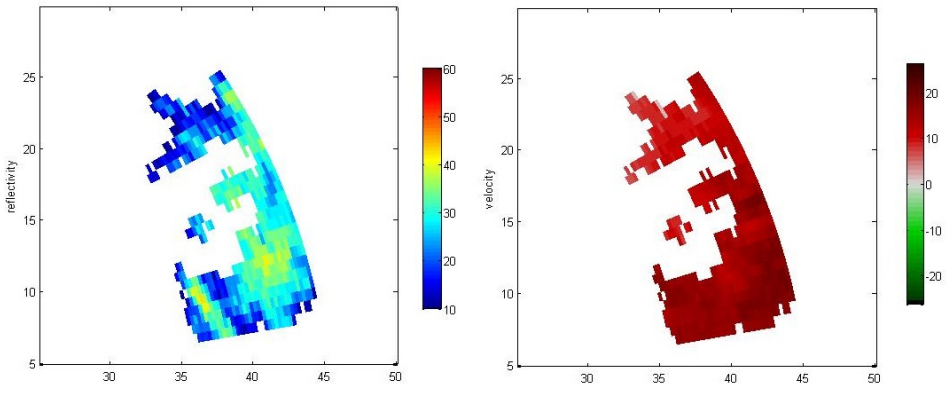

Figure 5.6: Final data pool used to estimate the PDF of the radial velocity of weather in the proximity of the wind farm at the end of the iteration. Notice the radial velocity estimate of the weather is nearly uniform.

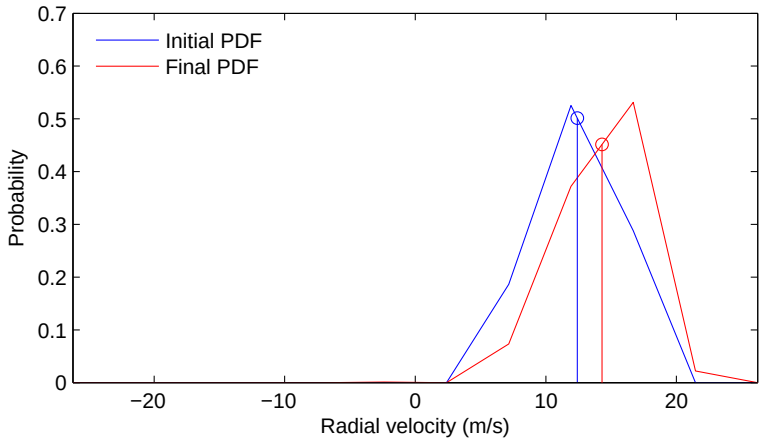

Figure 5.7: Comparison of the PDF estimated from the inital and final data pool through many times of iterations. The estimated mean velocities are also marked.

corrupted data. After the ASP, the negative side of the spectrum is significantly mitigated and the recovered spectrum resembles the true weather spectrum. It is worth noting that the spectrum components of WTC overlapped with the weather spectral component cannot be removed by ASP as they are inseparable in the frequency domain, which is one limitation of ASP.

Moment estimates are recovered based on the filtered PSD as shown in Fig. 5.9. The moments of the wind farm, true weather and mixed data are also shown for comparison. The radial velocity and spectrum width estimates are significantly improved. The recovered reflectivity estimate, however, compared with the true weather, is still biased due to the clutter residues. Fig. 5.10 shows the moment estimate bias comparison before and after applying ASP. It is obvious that as SCR increases, the estimation bias decreases for all moment estimates before and after ASP. Also, the moment estimates recovered by ASP has consistently lower bias for SCR less than 0 dB. Table 5.1 compares the average moment estimate bias and variance before and after ASP is applied. On average, the moment estimates are significantly improved, especially the mean radial velocity and the spectrum width.

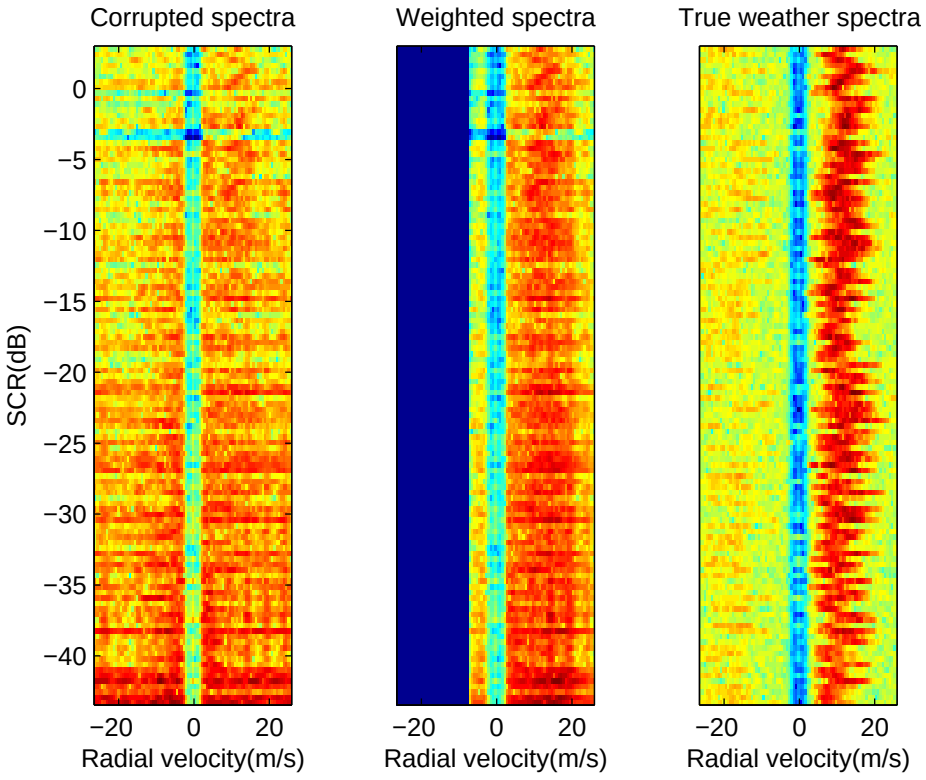

Figure 5.8: PSD from the WTC contaminated volumes, ASP processed and the true weather. The spectra from different volumes are stacked in the order of ascending SCR from bottom to top.

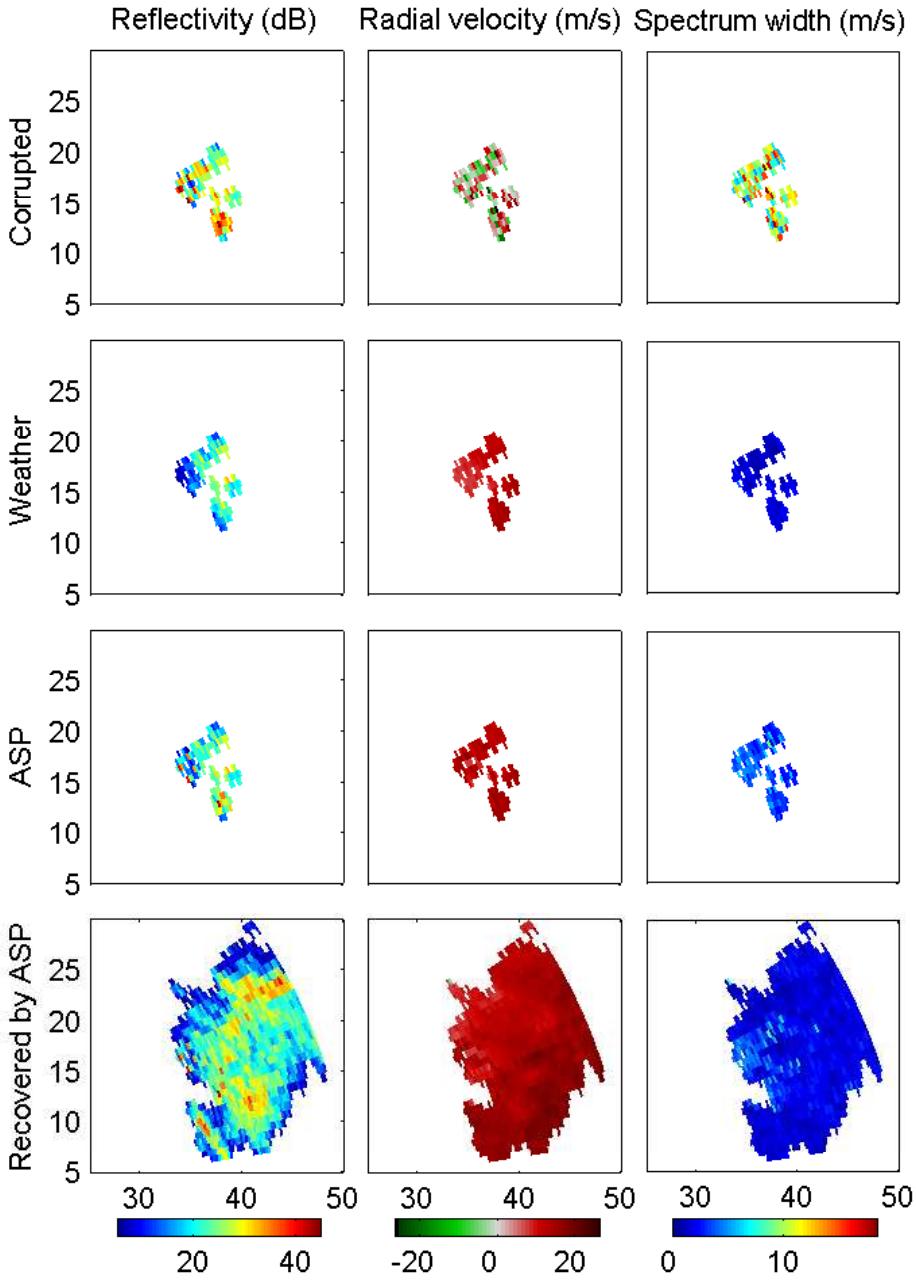

Figure 5.9: Recovered moment estimates by ASP compared with the true weather and corrupted data. Covariance method has been applied in estimating the moments.

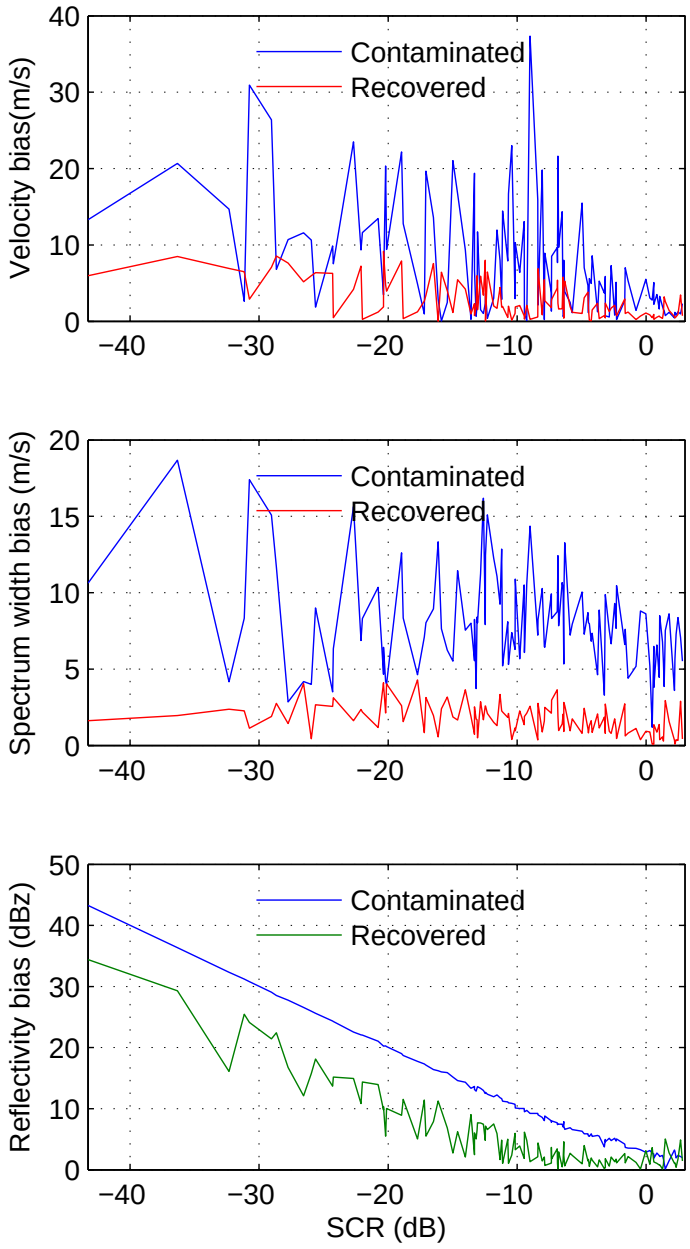

Figure 5.10: Comparison on the bias of moment estimate before and after applying ASP. Moment estimates from weather has been used as the true value.

Table 5.1: Improvement of moment estimates by applying ASP

Moment estimate comparison	**Bias/variance**		
	Reflectivity (dBz)	Radial velocity (ms^{-1})	spectrum width (ms^{-1})
Contaminated	11.4/14.2	-6.8/10.4	8.1/8.7
ASP recovered	4.5/8.6	2.3/3.6	1.8/2.0

As a short summary for the ASP mitigation algorithm, it generally improves the moment estimates in resolution volumes featuring both weather and wind turbine radar returns, especially when the SCR is low. The improvement for reflectivity estimate is limited as the frequency selection cannot mitigate WTC in the same Doppler frequency with weather. However, other mitigation methods such as spatial interpolation [28] can be applied as a supplement for reflectivity estimate. It is obvious that ASP is adaptive in the sense that the filter automatically updates as the weather changes. Unfortunately, the adaptivity cannot be demonstrated in this study due to lack of appropriate Level I data of weather and wind turbine coexistence.

5.3 WTC Mitigation of Moment Data

Telemetry and ASP mitigation require Level I IQ data and are both implementable in real-time operational mode. Yet the reality is that Level I data cannot be stored most of the time due to the large storage requirement. Only Level II moment data are archived in operational mode. Hence, a mitigation scheme has been developed using only Level II moment data, which can be applied offline.

Wind turbines blades, although high above the ground, are still near-surface target compared to various weather phenomena, which can extend to several kilometers high.

The radar beam becomes progressively higher as it propagates. At elevation of 0.5°, the beam bottom at 30 km is approximately 70 m above the antenna feed horn. While the beam bottom of 1.5° scan is over 160 m at the same range, which is higher than the blade and tower combined height of most wind turbines, not taking into account the terrain effect. Therefore, at the wind turbine location, it is usually true that only the lowest elevation scan at 0.5° is contaminated by WTC. The next higher elevation scan often has weather returns only. Fig. 5.11 gives an example of this elevation difference. It is clearly shown that the wind farm disappears on the reflectivity map at higher elevation scan as expected.

The area contaminated by WTC in the lowest elevation can be excluded as invalid data for moment estimates. Such "exclusion zones" are usually known by the radar operators if the coordinates of wind turbines are given in latitude and longitude. Based on the clean data at a higher elevation, it is tempting to patch the low elevation scan with the high elevation data since the two often look similar as shown in Fig. 5.11. However, the moment estimates can be significantly different in consecutive elevation scans. An example is shown in Fig. 5.12, where the radial velocity estimates at the two elevations are compared against each other. The difference is obvious, especially in the southwest of the view, where the precipitation is largely moving away from the radar (green) in the lower elevation, yet matching toward the radar (red) at higher elevation. This wind shear is commonly seen in weather fronts, inversion and downburst, etc., which are all important weather activities to meteorologists. Therefore, the WTC contaminated area cannot be simply patched by data from higher elevation scans.

A moment estimation method based on Maximum A Posterior (MAP) is developed to patch the exclusion zone in the lowest elevation scan of weather radar. In Bayesian statistics, the posterior probability is the conditional probability assigned after the relevant evidence is taken into account. Furthermore, the distribution of posterior probability is the probability distribution of unknown random quantity, conditional

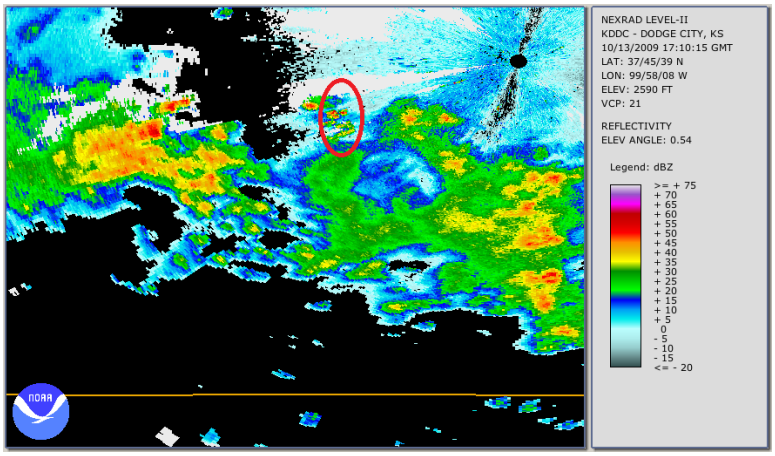

(a)

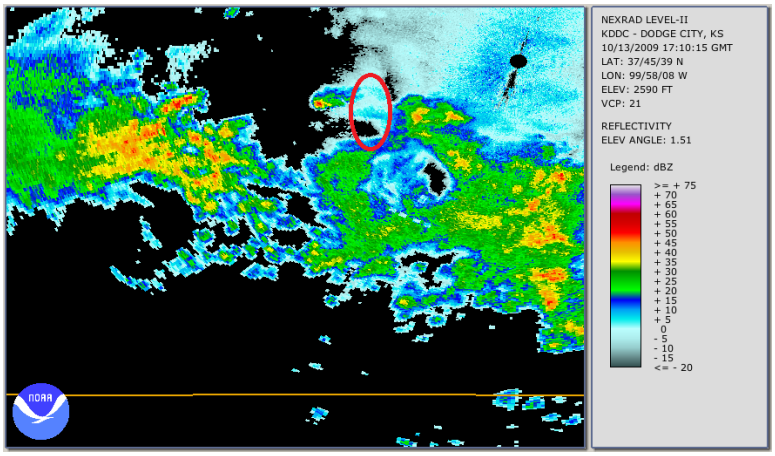

(b)

Figure 5.11: Level II data of the same volume scan from KDDC weather radar in VCP21 mode: (a) reflectivity estimate at the lowest elevation 0.54°, (b) reflectivity at the 2^{nd} lowest elevation 1.51°. The Gray County wind farm is circled in red.

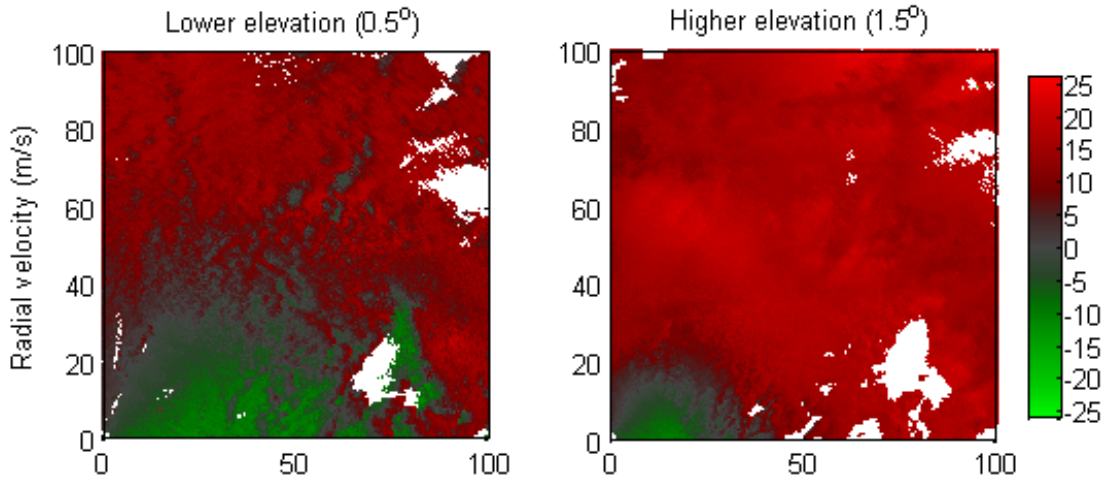

Figure 5.12: Comparison of mean radial velocity at 0.5° and 1.5°. The transparent color is due to range aliasing.

on observed evidence. In our context, the unknown quantity to be estimated is the moments of the lowest elevation scan at the exclusion zone. The observations, are the moments at the corresponding higher elevation. Given the posterior probability distribution, the best estimate is the one with highest posteriori probability:

$$\hat{X_L} = \underset{x_L}{arg\,max}\{X_L|p(X_L|X_H)\} \tag{5.17}$$

where X_L and X_H are the moment estimate of the lower and higher elevation, respectively. For simplicity, it is assumed that the moment of lower elevation is only conditioned on the corresponding moment of higher elevation.

Therefore, the key is to obtain the posterior probability distribution. Similar to ASP using data from the uncontaminated resolution volumes and nearby area to estimate the radial velocity distribution, the moment estimates from these resolution volumes at both elevations are used to train the posterior probability distribution. The same data pool used in ASP simulation is used here. The moment estimates of the wind farm only, weather only and the mix data of the higher elevation is shown in Fig. 5.13. Compared to Fig. 5.3 of the lower elevation, the reflectivity of the wind

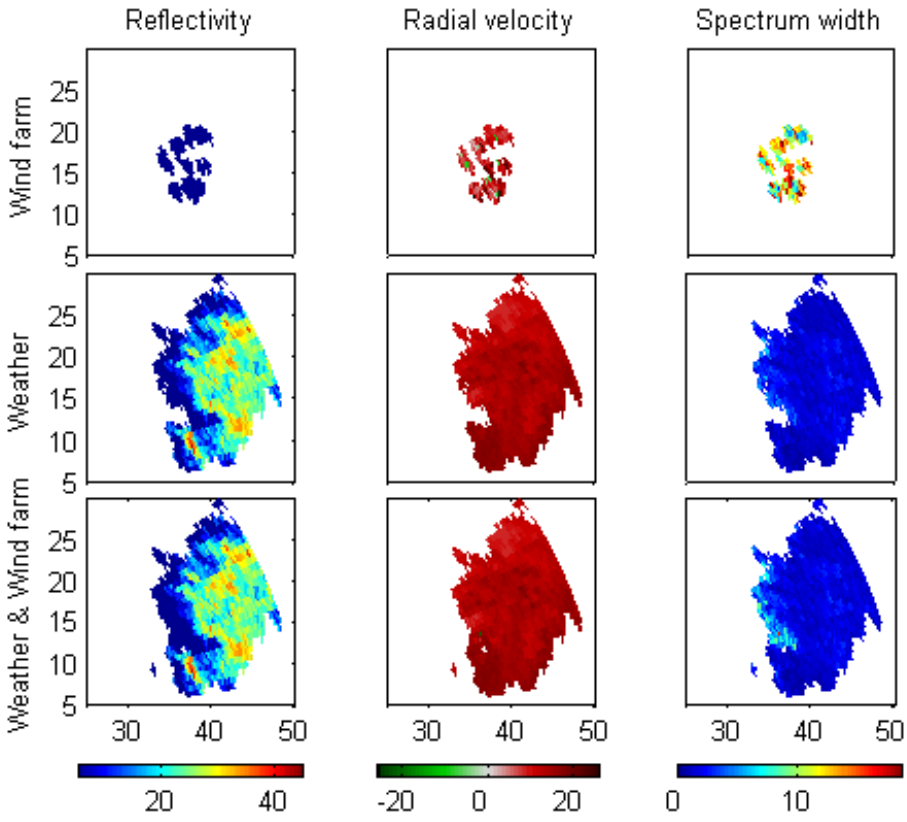

Figure 5.13: Moment estimates from the azimuthally rotated wind farm, the weather and the mixed data at elevation of 1.5°. A high pass filter with bandwidth of 2.5 ms^{-1} is applied and the filtered power spectrum density is used for moment estimates.

farm is much weaker, most of which are below 10 dBz. Therefore, the signal to clutter ratio at this elevation should be relatively high, which is true as shown in Fig. 5.14. In all of the resolution volumes contaminated by WTC at the lower elevation scans, the SCR is above zero, ranging from 0 to 50 dB. With SCR of this high, the estimate bias of the weather should be realtively small. Thus, estimates at the higher level are considered uncontaminated in the context.

The conditional probability given the higher elevation estimates $p(Z_L|Z_H)$, $p(V_L|V_H)$ and $p(W_L|W_H)$ are estimated using the uncontaminated volumes in and near the wind farm for each observed Z_H, V_H and W_H and are shown in Fig. 5.15. The distribution

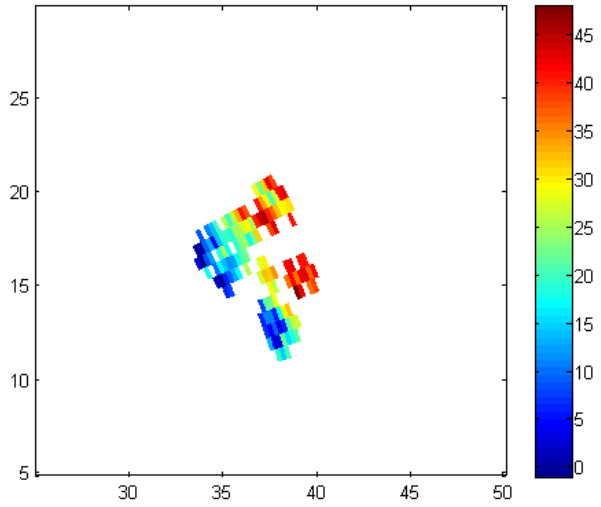

Figure 5.14: SCR of the wind farm area at 1.5° elevation scan in dB. The SCR is relatively low at the southwest part because it falls on the edge of the storm, where the weather return has lower reflectivity.

is normalized to the total number of lower elevation resolution volumes corresponding to the given moment of the upper elevation volume. Some of the distribution may be singular due to insufficient number of sample volumes used for estimation. In order to obtain sufficient samples, the moments at the higher elevation level have been distributed into evenly spaced bins. The increment steps is 1 dB for the reflectivity and 0.5 ms^{-1} for both radial velocity and spectrum width.

The recovered moment estimates at the lower elevation are compared with the ones from true weather and the mix data in Fig. 5.16. High reflectivity estimates in the WTC contaminated area are slightly over corrected. The recovered reflectivity in the contaminated area seems lower than the actual reflectivity of weather return. Similar over correction occurs for the mean radial velocity estimates, as part of the recovered area seems darker than the radial velocity estimate of the weather. The spectrum width, however, improves the most without significant errors.

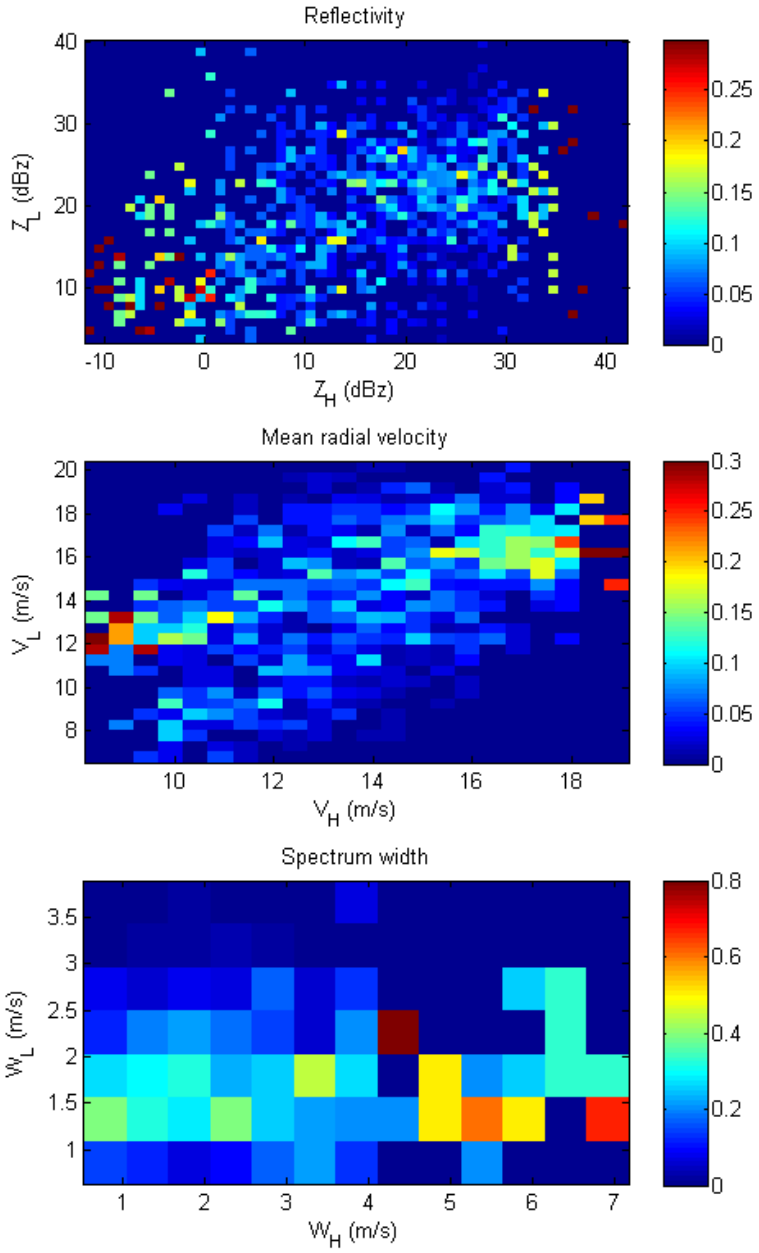

Figure 5.15: Posterior probability distribution. The probability is normalized and color coded. The total number of resolution volume pairs used to estimate the distribution is approximately 1000.

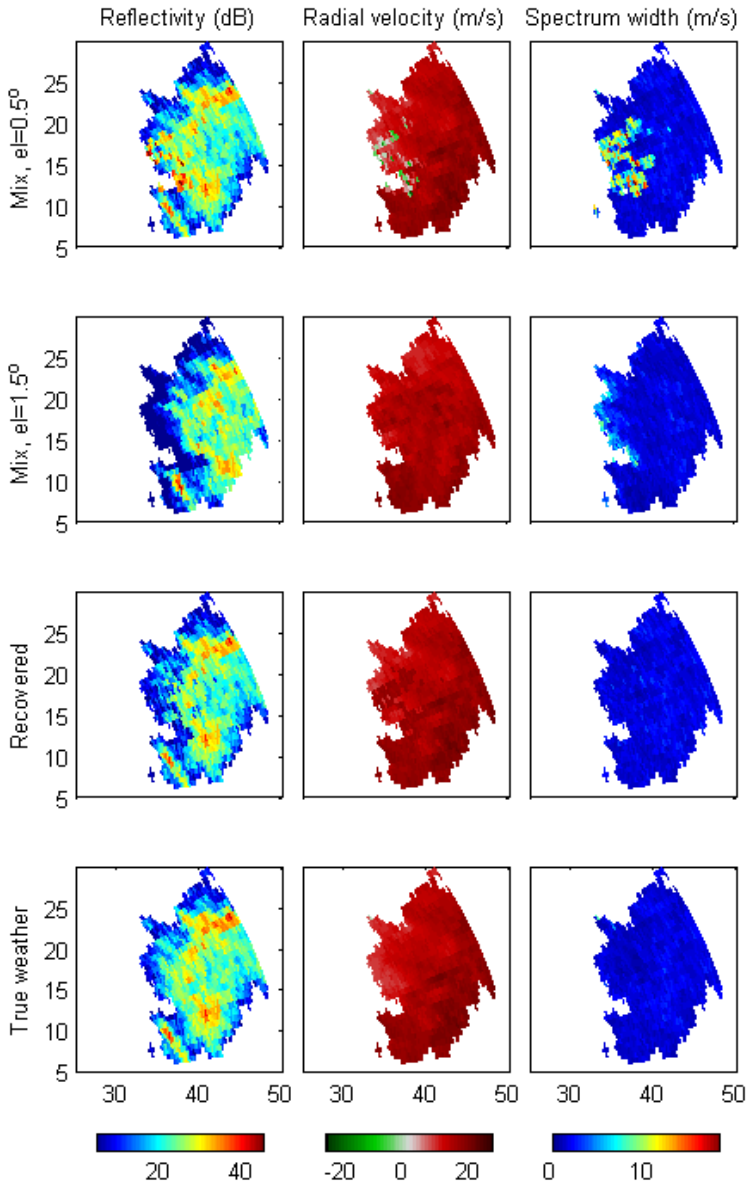

Figure 5.16: Moment estimates of mixed data of wind turbines and weather at 0.5°, moments of mixed data at 1.5°, moments recovered at 0.5° and moment estimates of the weather at 0.5°.

Table 5.2: Improvement of moment estimates by applying MAP based mitigation

Moment estimate comparison	**Bias/variance**		
	Reflectivity (dBz)	Radial velocity (ms^{-1})	spectrum width (ms^{-1})
Contaminated	11.4/14.2	-6.8/10.4	8.1/8.7
ASP recovered	-4.9/8.8	3.7/4.8	0.0/0.8

To quantify the estimation bias, the recovered moment estimates are compared against the corresponding moments of the true weather, which are sorted in ascending SCR as shown in Fig. 5.17. Again, the estimation bias decreases as the SCR increases. When the SCR is greater than zero, the reflectivity and radial velocity estimates from the corrupted data actually have lower bias than the recovered moments, which is consistent with the ASP method. Therefore, both methods are only effective for low SCR cases, i.e., when SCR is less than 0 dB. It is interesting to notice that the recovered spectrum width has consistently better performance even with high SCR.

Table 5.2 lists the average estimate bias and variance improvement for all three moment estimates. The results are consistent with the observation in Fig. 5.16, where the reflectivity is underestimated and mean radial velocity is overestimated. The spectrum width, however, is non-bias on average for this case. The improvement by implementing the mitigation algorithm based on MAP is similar to ASP. However, only Level II data are used in the MAP mitigation. It is also worth mentioning that both mitigation methods are not limited in mitigating WTC, but can be applied to mitigate general non-stationary clutter in weather radar observations, whose Doppler spectrum varies from scan to scan, as both algorithms rely only on the characteristics of the weather signal.

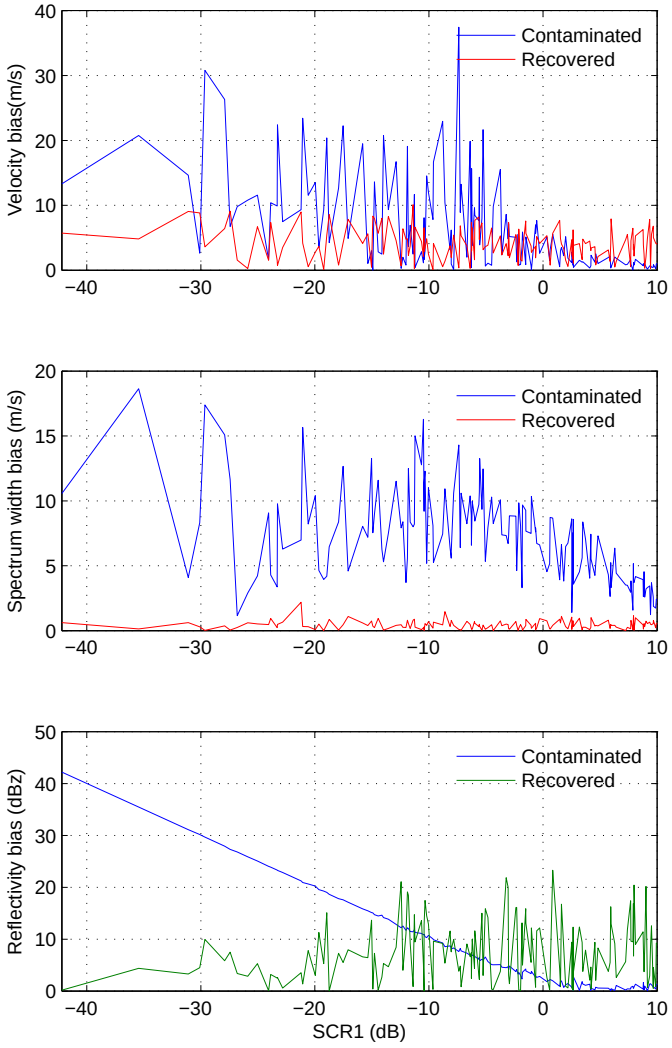

Figure 5.17: Bias analysis of the mitigation algorithm based on MAP. All moment estimate bias has been sorted in asecnding SCR. However, the increment of SCR is non-uniform.

5.4 Wind Farm Siting and Mitigation

The most effective way to reduce wind turbine clutter is to site wind turbines far away from the radar. As the beam propagates, the beam height becomes progressively higher above the ground due to the earth curvature. Therefore, at certain distance, the bottom of the beam will be higher than the combined height of the tower and the blades. Using the 4/3 equivalent earth model, it is calculated that at 50 km, the bottom of the 0.5° beam, which is the lowest among all NEXRAD VCP modes is approximately 170 m above the radar antenna feed horn level. Not taking into account the terrain effect, this is higher than most utility-scale wind turbines. Therefore, 50 km is usually used to roughly determine the LOS avoiding distance of proposed wind farms.

Because the dimensions of the utility-scale wind turbines are exceptionally large, strong radar returns are often expected, which will result in low SCR if the radar target falls in the same resolution volume with the wind turbine. For rigid targets, the SCR is exclusively determined by the RCS ratio of the target and wind turbine. However, weather radar observes various forms of precipitation, the reflectivity of which is calculated based on the cumulative return from the entire resolution volume. The SCR can be obtained from comparing the radar equation and weather equation:

$$SCR = \frac{< p_{wx}(r) >}{< p_{wt}(r) >} = r^2 \frac{\eta}{\sigma} D_1 \tag{5.18}$$

where η is the reflectivity of weather and σ is the RCS of the wind turbine. D_1 is the constant term. The SCR is proportional to the square of range as the size of the resolution volume is proportional to the square of range. This unique characteristic makes it even more beneficial to have wind turbines sited far away from weather radars.

The ROC has published the rule-of-thumb on wind farm impact versus range to nearby NEXRAD radar [30]. The impact increases as the wind farms are sited closer

to the radar, especially within 18 km. Multiple radar elevation scans are likely to be contaminated if the wind farms are inside this distance, which further limits the data availability. The multi-path clutter effect is also more likely to occur at closer distance. This has been used as a guidance for wind farm developers since. If a proposed wind farm is closer than this range, the developer is suggested to consult ROC for further investigation. Though the guidance is on voluntary basis, it has shown some positive responses.

The histograms of the range of US wind farms to closest NEXRAD radar before and after 2008 are shown in Fig. 5.18. Before 2008, based on the statistics, there are 11 wind farms within 18 km of a NEXRAD radar out of 549 wind farms being studied. After 2008, an extra 542 wind farms have been added, including operational, under construction and proposed, only 5 of which are within 18 km of any NEXRAD radars. This significant decrease suggests that the official guidance from the radar community, even on a voluntary basis, may raise the awareness of the wind power community and positively affects the siting of wind farms, mitigating the potential WTC in advance.

Many of the wind farm developers may be cooperative at the time of siting if there are other options. The FAA provides a Preliminary Screening Tool (PST) based on radar LOS coverage [74]. The tool is to assist the developers to determine if a proposed site will be in the radar LOS and whether an aeronautical study is necessary before the construction. The NEXRAD radars have been recently added to the PST, so that the developer can also make use of this tool to find out the potential impact of the proposed wind farms on nearby weather radar.

The distance from the radar is not the only factor that determines whether the wind turbines fall in the radar LOS coverage. The elevation difference between the wind turbine and the radar, i.e., the terrain in the radar vicinity is also an important contributing factor. Generally, the radar is built high above the ground to avoid

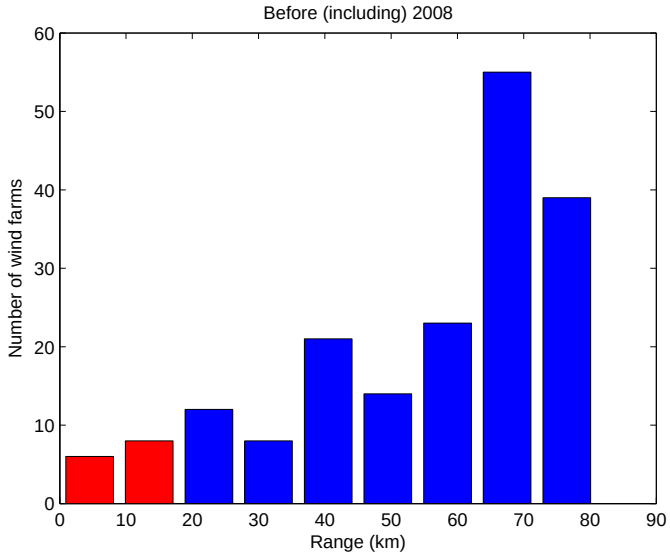

(a)

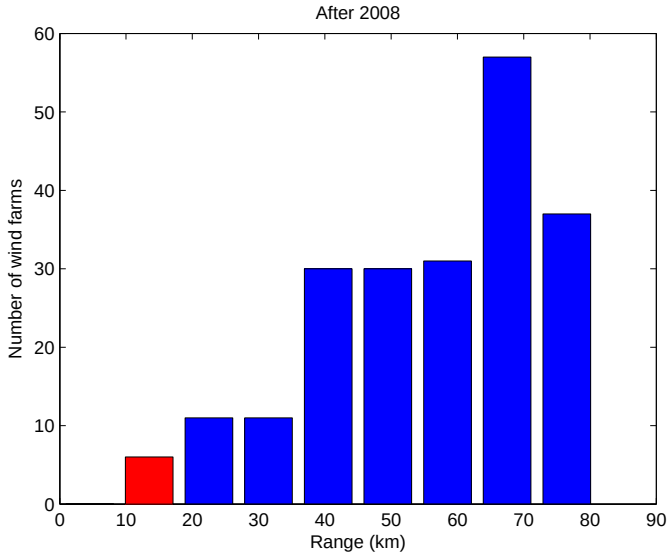

(b)

Figure 5.18: Comparison of histograms on wind farm distance to NEXRAD radar before(including) and after 2008. Only those within 80 km of the radar are considered. The red bars accounts for wind farms in 18 km of any NEXRAD radar.

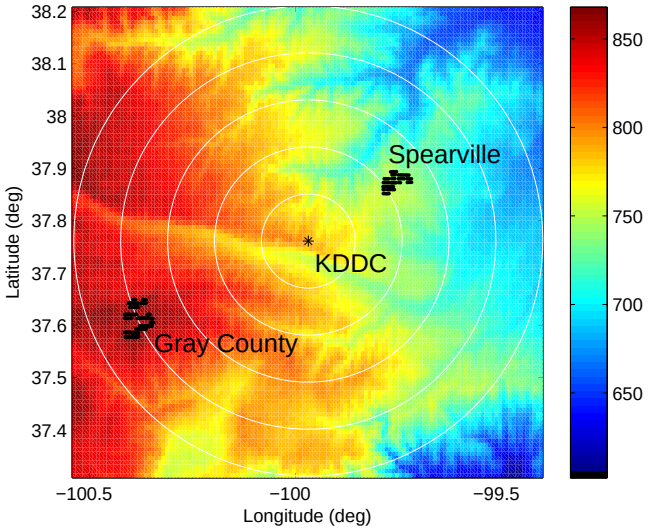

Figure 5.19: Terrain map near the KDDC radar site. The pseudo color represents elevation in meters above sea level and the radar antenna is approximately at 816 m.

potential ground clutter and beam blockage. The wind turbines are also installed at higher ground for more favorable wind conditions. As an example, the terrain near the KDDC site is shown in Fig. 5.19, where it is higher on the west of the radar and lower on the east. Both the wind farms and the radar are higher than surrounding terrain.

The wind turbine blade sweeps from h_b to h_t in elevation:

$$h_b = h_h - D/2 \tag{5.19}$$

$$h_t = h_h + D/2 \tag{5.20}$$

where h_b, h_t are height of the bottom and top of the rotation plane, h_h is hub height above the radar feed horn, and D is the rotor diameter. For Vestas V47 wind turbine in the Gray County wind farm, h_b=41.5 m, h_h=65 m and h_t=88.5 m. For the GE 1.5 MW wind turbine in Spearville wind farm, h_b=41.5 m, h_h=80 m and h_t=118.5 m. It is interesting to notice that the two wind turbines have the same h_b, even though they

have different hub height and rotor diameter. Fig. 5.20 shows the LOS coverage of both wind farms taking into consideration the terrain and wind turbine dimensions.

Only if the wind turbine falls into the LOS coverage at h_b, will the entire blades be fully illuminated at all time. Otherwise, the blades will only be partially illuminated, which is the case for both wind farms. At h_h, most wind turbines in the Gray County wind farm are in the LOS coverage of the radar, however, none of the wind turbines in the Spearville wind farm is. At h_t, all wind turbines in both wind farms fall into the LOS coverage. For all wind turbines in the Speaville wind farm, only the upper half of the rotation plane is partially illuminated by the radar. A much different conclusion could be drawn if relying only on the beam and wind turbine height without any knowledge of the terrain. Therefore, terrain information is necessary to correctly evaluate the impact of a wind farm to nearby radar and to effectively guide the siting of wind farms in order to avoid or reduce the potential radar clutter effect.

The Level-II data at the KDDC site for the entire year of 2008 are used to calculate the average reflectivity at the two wind farms. Only the clear air VCP32 mode is taken into account to exclude the possibility of having weather signal mixing into the wind turbine returns. Throughout the year, both the wind speed and direction vary so that the azimuth aspect angle and pitch should change correspondingly. The average reflectivity, therefore, represents the RCS of the wind turbines in the average sense, which is shown in Fig. 5.21.

Both of the wind farms are isolated clutter as previously discussed, which is again confirmed as the high reflectivity closely match the wind turbine locations. The resolution volumes in between wind turbines have much lower reflectivity than the ones with wind turbines, suggesting the range uncertainty due to the atmospheric variation is minimal. It is interesting to notice some other features which are also preserved in the average reflectivity map. Conventional ground clutter should have

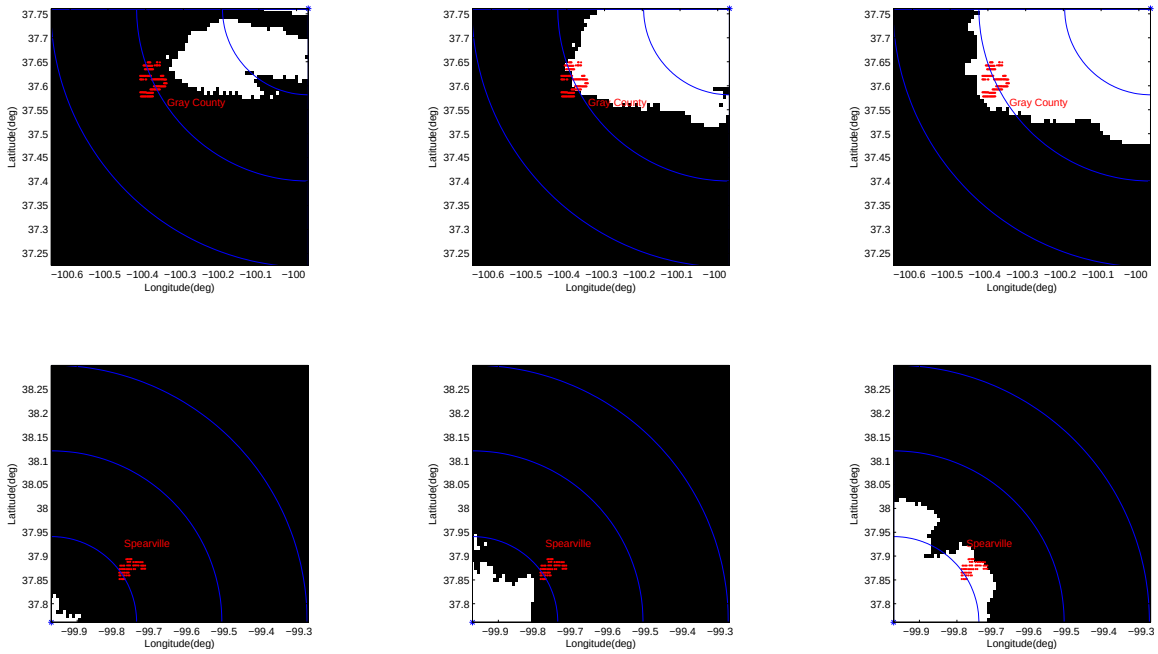

Figure 5.20: KDDC radar LOS of the two wind farms, the columns from left to right corresponds to h_b, h_h and h_t. The range rings are 20 km apart and the whilte area is the LOS for wind turbines at the given height. The 4/3 earth equivalent model has been used to estimate the LOS.

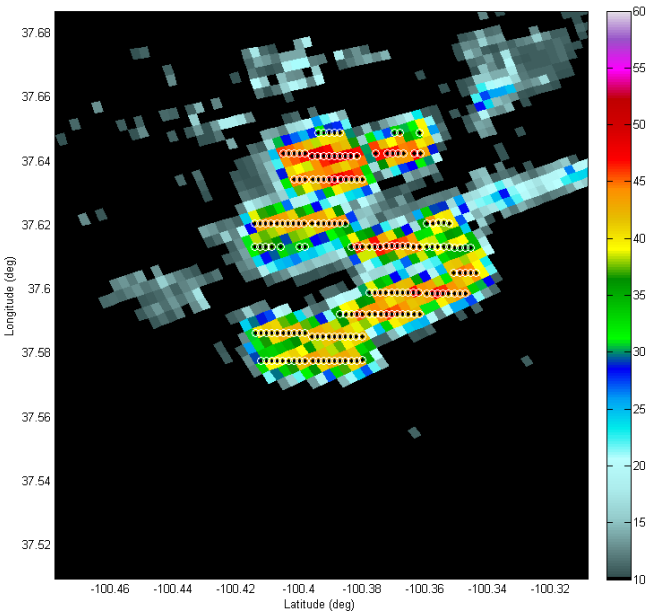

(a)

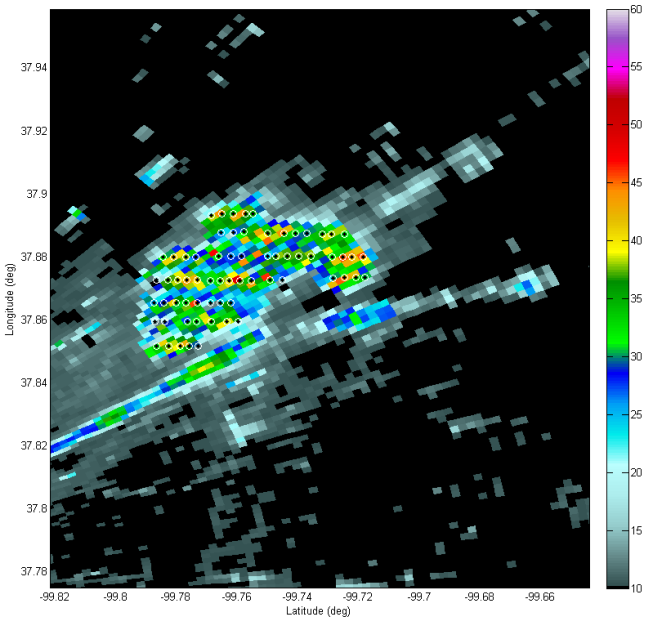

(b)

Figure 5.21: Annual average reflectivity estimate in 2008: (a) the Gray County wind farm, (b) the Spearville wind farm

been mitigated by GMAP filter, yet there is a line feature crossing both wind farms, which is caused by moving vehicles along Highway 56.

The size of the GE 1.5 M wind turbine in Spearville wind farm is much larger than the Vestas V47 wind turbine in Gray County wind farm. The average RCS should be larger correspondingly. In addition, the range of the Spearville wind farm is closer to the radar. Because the reflectivity is inversely proportional to the square of the range, the reflectivity of the wind turbine resolution volumes in Spearville wind farm should be much higher than the ones in Gray County wind farm. However, it is clearly shown in Fig. 5.21 that the actual reflectivity of the Spearville wind farm is much lower than the Gray County wind farm. The terrain dependent LOS coverage in the vicinity of KDDC radar previously discussed explains this difference as the Spearville wind farm is less illuminated by the main beam of the radar.

The siting of wind farms is a comprehensive process, which includes long-term investigation of wind resource, environmental analysis on land usage constraint, impact analysis on bird migration, power grid integration, etc. However, it is not long before that the radar avoidance starts to be included in this process. Without effective mitigation strategies applied in operation, it is best to site the wind farms as far away from the radar as possible. Terrain variation must be included as well to determine the actual LOS coverage at given height.

Chapter 6

Conclusions and Suggestions for Future Studies

The impact of wind turbines on radar has been gradually realized in the past decade. Because of the extremely large size, wind turbines normally have high RCS, resulting low SCR, which significantly degrades the radar data quality. The rotation of the blade can cause non-stationary micro-Doppler radar signatures that varies from scan to scan and turbine to turbine, which the conventional ground clutter filter has failed in mitigating.

Characterization of the radar signatures of wind turbines is a challenging task. Commercial EM solvers usually mesh the target surface into many small polygons, then calculate the RCS and phase of these elements and coherently integrate for the back scattered field. This process will require exceptionally large computational power due to the electrical large size and complex motions of the wind turbine. In order to calculate the RCS of large wind turbine in realistic time frame, a high-frequency approximation based on PO and GTD has been developed for the wind turbine tower. The simulation result is closely comparable with FEKO.

The cause of various impacts of wind farms on the weather radar operations were analyzed, including receiver saturation, beam blockage, isolated clutter, AP, and multi-path clutter effect. Case studies of the NEXRAD radar were provided for typical isolated and multi-path clutter effect. The GMAP ground clutter filter utilized in NEXRAD radar signal processing was applied on WTC. The large bias of moment estimate after the filter due to clutter residue corresponding to the fast moving blade of the wind turbine is why mitigation techniques are needed for WTC.

Field studies with mobile radar RaXPol were carried out. The raw IQ data analysis reveals the unique micro-Doppler signatures of the wind turbine. The limitations of characterizing wind turbine radar signal by radar measurement motivated the development of the Radar Wind Turbine Testbed for characterizing wind turbine radar signature by scaled measurements. A scaled wind turbine model was customized and frequency domain measurement using VNA and time-domain measurement using the scatterometer are performed. The scatterometer is a high-resolution indoor radar developed independently from scratch. Two IQ calibration techniques are developed for correcting the IQ imbalance. The first-ever measurement was performed on a wind turbine for all blade position and azimuth aspects. The signal statistics are analyzed and the WTC signal is best fit with Gamma distribution. After all, it is a non-stationary random process.

Mitigation using telemetry information is first exploited. The rotation rate, wind speed and pitch of each wind turbine are included in the telemetry. With this assumption, the WTC contaminated weather signal can be recovered by searching through the knowledgebase of pre-stored WTC IQ signal and Wiener filter based signal conditioning. The ASP algorithm, designed for weather radar is introduced in this study. A band pass filter is adaptively formed from scan to scan to filter out the WTC spectrum components outside the estimated signal bandwidth. The recovered moments improves significantly in terms of estimation bias and variance, especially the mean radial velocity and spectrum width. A mitigation method based on MAP was also developed for Level-II data, which achieves similar performance as ASP, yet only requiring moment data, thus can be applied offline. Integrating any of the above mitigation techniques into current radar system requires a large amount of testing. Therefore, the current most effective way of mitigation perhaps is avoiding proposed wind farms in the radar LOS coverage by carefully studying the DEM, wind turbine dimensions, etc.

A wide scope of work has been done throughout this study. The RCS characterization of the wind turbine is important but extremely challenging. Recommendations for future work include applying reliable and fast hybrid high frequency approximations like the PO+GTD on calculating the RCS of the rotor blade. With the scatterometer fully functioning now, it will be straightforward to verify any upcoming RCS characterization methods for wind turbines.

The scatterometer needs to be expand to millimeter wave range. Millimeter-wave measurements of the wind turbine model are needed to correctly match the scaling ratio. Although dual-polarized measurements have been made using the scatterometer, not many analysis have been made, which should are recommended for future studies. Future field measurements should follow the analysis in this study to determine the proper beam steering in both azimuth and elevation to ensure the wind turbine under study reside in the main beam of the radar. And, it is strongly encouraged to use the GUI developed in this study to immediately check the data on site.

As for the mitigation strategy, the three techniques proposed in this study still need to be tested via a large amount of data before going operational. Quantitative analysis on the performance improvement is much needed to further verify the effectiveness of the proposed mitigation schemes. The database of the telemetry method should be replaced by abstract features independent from weather signal if applicable.

The wind turbine interference to nearby radars is only recently recognized as a new type of clutter. Many studies have just started in this area. The characterization of the radar signature of wind turbines and mitigation of the clutter effect are two most sopisticated topics in this area, which have been carried out parallel in this study. Though not many signatures characterized in this study have been directly applied in current mitigation strategies yet, they are critical in developing more effective mitigation algorithms.

Reference List

[1] J. C. Maxwell, "On physical lines of force," *The London, Edinburgh and Dublin Philosophical Magazine and Journal of Science*, 1861.

[2] H. Hertz, *Electric Waves: Being Researches on the Propagation of Electric Action with Finite Velocity Through Space (English Translation)*. Dover, 1893.

[3] J. Gough and G. Britain, *Watching The Skies: A History Of Ground Radar For The Air Defence Of The United Kingdom By The Royal Air Force From 1946 To 1975*. London: HMSO, 1993. [Online]. Available: http://isbnplus.org/9780117727236

[4] M. I. Skolnik, *Introduction to Radar Systems*, 3rd ed. New York: MaGraw-Hill, 2001.

[5] IEEE, *IEEE Standard Letter Designations for Radar-Frequency Bands*, IEEE Std., 2003.

[6] P. Stocia and R. L. Moses, *Spectral Analysis of Signals*, 1st ed. Prentice Hall, 2005.

[7] A. V. Oppenheim and R. W. Schafer, *Discrete-Time Signal Processing*, 2nd ed. Prentice Hall, 1998.

[8] P. B. Chilson, W. F. Frick, J. F. Kelly, K. W. Howard, R. P. Larkin, R. H. Diehl, J. K. Westbrook, T. A. Kelly, and T. H. Kunz, "Partly cloudy with a chance of migration: Weather, radars, and aeroecology," *Bulletin of the American Meteorological Society*, vol. 93, no. 5, pp. 669–686, 2011.

[9] W. Melvin, "A STAP overview," *Aerospace and Electronic Systems Magazine, IEEE*, vol. 19, no. 1, pp. 19–35, Jan 2004.

[10] G. Capraro, A. Farina, H. Griffiths, and M. Wicks, "Knowledge-based radar signal and data processing: A tutorial review," *Signal Processing Magazine, IEEE*, vol. 23, no. 1, pp. 18–29, Jan 2006.

[11] A. D. Siggia and R. E. Passarelli, "Gaussian model adaptive processing (GMAP) for improved ground clutter cancellation and moment calculation," in *Radar Conference (EuRAD), European*, 2004.

[12] B. Isom, "Characterization and mitigation of wind turbine clutter for the WSR-88D radar network," Master's thesis, University of Oklahoma, 2007.

[13] AWEA, "Awea U.S. wind industry fourth quarter 2012 market report," American Wind Energy Association, Tech. Rep., 2012.

[14] DOE, "20% wind energy by 2030, increasing wind energy's contribution to U.S. electricity supply," Department of Energy, Tech. Rep., 2008.

[15] T. J. Price, *Oxford Dictionary of National Biography.* Oxford University Press, 2004.

[16] Nature, "wind turbines cause trouble to bird," http://www.nature.com/news/the-trouble-with-turbines-an-ill-wind-1.10849.

[17] D. Colby, R. Dobie, G. Leventhall, D. M. Lipscomb, R. J. McCunney, M. T. Seilo, and B. Sondergaard, "Wind turbine sound and health effects: An expert panel review," American Wind Energy Association, Tech. Rep., 2009.

[18] T. D. Crum and R. L. Alberty, "The wsr-88d and the wsr-88d operational support facility," *Bulletin of the American Meteorological Society*, vol. 74, no. 9, pp. 1669–1687, 1993.

[19] R. P. Fanxing Kong, Yan Zhang, "Scattering of wind turbines - radar wave propagation analysis in wind farms," in *URSI meeting*, Boulder, CO, Jan. 2014.

[20] DOD, "Report to the congressional defense committees: the effect of windmill farms on military readiness," Department of Defense, USA, Tech. Rep., 2006.

[21] T. B. A. Senior, D. L. Sengupta, and J. E. Ferris, "TV and FM interference by windmills," University of Michigan, Tech. Rep. 014438-1-F, 1977.

[22] G. J. Poupart, "Wind farms impact on radar aviation interests," QinetiQ Ltd, Tech. Rep. W/14/00614/00/REP, 2003.

[23] M. M. Butler and D. A. Johnson, "Feasibility of mitigating the effects of windfarms on primary radar," Alenia Marconi Systems Ltd,, Tech. Rep. W/14/00623, 2003.

[24] A. Buterbaugh, B. M. Kent, K. C. Hill, G. Zelinski, R. Hawley, L. Cravens, T. Van, C. Vogel, and T. Coveryou, "Dynamic radar cross section and radar Doppler measurements of commercial general electric windmill power turbines part 2- predicted and measured Doppler signatures," in *AMTA symposium*, St Louis, MO, 2007.

[25] B. M. Kent, K. C. Hill, A. Buterbaugh, G. Zelinski, R. Hawley, L. Cravens, Tri-Van, C. Vogel, and T. Coveyou, "Dynamic radar cross section and radar Doppler measurements of commercial general electric windmill power turbines part 1: Predicted and measured radar signatures," *Antennas and Propagation Magazine, IEEE*, vol. 50, no. 2, pp. 211–219, April 2008.

[26] R. J. Vogt, T. D. Crum, J. T. Snow, R. Palmer, B. Isom, D. W. Burgess, and M. S. Paese, "An update on policy considerations of wind farm impacts on WSR-88D operations," in *24th International Conference on Interactive Information and Processing Systems (IIPS) for Meteorology, Oceanography, and Hydrology*, no. 6B.4. Amer. Meteor. Soc, 2008.

[27] R. J. Vogt, J. R. Reed, T. D. Crum, J. T. Snow, R. Palmer, B. Isom, and D. W. Burgess, "Impacts of wind farms on WSR-88D operations and policy considerations," in *23rd International Conference on Interactive Information and Processing Systems (IIPS) for Meteorology, Oceanography, and Hydrology.* American Meteorology Society, 2007.

[28] B. M. Isom, R. D. Palmer, G. S. Secrest, R. D. Rhoton, D. Saxion, T. L. Allmon, J. Reed, T. Crum, and R. Vogt, "Detailed observations of wind turbine clutter with scanning weather radars," *Journal of Atmospheric and Oceanic Technology*, vol. 26, no. 5, pp. 894–910, 2009.

[29] R. J. Vogt, T. Crum, J. Sandifer, R. Steadham, T. L. Allmon, G. Secrest, E. J. Ciardi, R. Guenther, and R. Palmer, "Continued progress in assessing and mitigating wind farm impacts on WSR-88Ds," in *25th Conf. on International Interative Information and Processing Systems (IIPS) for Meteorology, Oceanography and Hydrology*, no. 11B.6. American Meteorology Society, 2009.

[30] R. J. Vogt, T. D. Crum, M. J. B. Sandifer, E. J. Ciardi, and R. Guenther, "A way forward wind farm - weather radar coexistance," in *Wind Power Conf.* American Wind Energy Association, 2009.

[31] R. J. Vogt, T. D. Crum, W. Greenwood, E. J. Ciardi, and R. Guenther, "Recent efforts to improve estimates of and mitigate potential wind turbine clutter impacts on WSR-88Ds," in *27th International Conference on Interactive Information and Processing Systems (IIPS) for Meteorology, Oceanography, and Hydrology.* AMS, Jan. 2011 2011.

[32] R. J. Vogt, T. D. Crum, and E. J. Ciardi, "How to successfully work with NOAA on wind turbine–NEXRAD rdar interference issues, an update," in *Wind Power Conf.*, 2012.

[33] D. W. Burgess, T. D. Crum, and R. J. Vogt, "Impacts of wind farms on WSR-88D radars," in *AMS Annual Conf.* American Meteorology Society, 2008.

[34] J. Pinto, J. C. G. Matthews, and C. Sarno, "Radar signature reduction of wind turbines through the application of stealth technology," in *Antennas and Propagation, 2009. EuCAP 2009. 3rd European Conference on*, 2009, pp. 3886–3890.

[35] J. Pinto, J. Matthews, and C. Sarno, "Stealth technology for wind turbines," *IET Radar Sonar & Navigation*, vol. 4, no. 1, pp. 126–133, 2010.

[36] L. Rashid and A. Brown, "Partial treatment of wind turbine blades with radar absorbing materials (RAM) for RCS reduction," in *Antennas and Propagation (EuCAP), 2010 Proceedings of the Fourth European Conference on*, 2010, pp. 1 – 5.

[37] L. S. Rashid and A. K. Brown, "Radar cross-section analysis of wind turbine blades with radar absorbing materials," in *Radar Conference (EuRAD), 2011 European*, 2011, pp. 97–100.

[38] S. Appleton, "Stealthy turbines development," http://www.taplondon.co.uk/bwea31/files/steveappleton.pdf, 2010.

[39] W. Benner, "MPAR program overview and status," in *23rd International Conference on Interactive Information and Processing Systems (IIPS) for Meteorology, Oceanography, and Hydrology*, 2007.

[40] C. A. Jackson and M. M. Butler, "Options for mitigation of the effects of windfarms on radar sytems," in *Radar Systems, 2007 IET International Conference on*, 2007, pp. 1 – 6.

[41] J. Perry and A. Biss, "Wind farm clutter mitigation in air surveillance radar," *Aerospace and Electronic Systems Magazine, IEEE*, vol. 22, no. 7, pp. 35–40, 08 August 2007.

[42] E. Aarholt and C. A. Jackson, "Wind farm gapfiller concept solution," in *Radar Conference (EuRAD), 2010 European*, 2010, pp. 236–239.

[43] B. Gallardo-Hernando, F. Perezrez-Martinez, and F. Aguado-Encabo, "Detection and mitigation of wind turbine clutter in C-band meteorological radar," *IET Radar, Sonar & Navigation*, vol. 4, no. 4, pp. 520–527, 2010.

[44] F. Nai, R. D. Palmer, and S. M. Torres, "Range-Doppler domain signal processing to mitigate wind turbine clutter," in *Radar Conference (RADAR), 2011 IEEE*. IEEE, 2011, pp. 841–845.

[45] F. Nai, "Wind turbine clutter mitigation for weather radars," Master's thesis, University of Oklahoma, 2011.

[46] J. C. G. Matthews, C. Sarno, and R. Herring, "Interaction between radar systems and wind farms," in *Antennas and Propagation Conference, 2008. LAPC 2008. Loughborough*, 2008, pp. 461–464.

[47] F. Darcy and D. d. l. Vega, "A methodology for calculating the interference of wind farm on weather radar," in *Antennas & Propagation Conference, 2009. LAPC 2009. Loughborough*, 2009, pp. 665–667.

[48] G. Greving, W. D. Biermann, and R. Mundt, "Radar and wind turbines - RCS theory and results for objects on the ground and in finite distances," in *Microwaves, Radar and Remote Sensing Symposium (MRRS), 2011*, 2011, pp. 321–326.

[49] Y. F. Lok, J. Wang, and A. Palevsky, "Simulation of radar signal on wind turbine," in *Radar Conference, 2010 IEEE*, 2010, pp. 538–543.

[50] Y. Zhang, A. Huston, R. D. Palmer, R. Albertson, F. Kong, and S. Wang, "Using scaled models for wind turbine EM scattering characterization: Techniques

and experiments," *Instrumentation and Measurement, IEEE Transactions on*, vol. 60, no. 4, pp. 1298–1306, 2011.

[51] C. Morlaas, M. Fares, and B. Souny, "Wind turbine effects on VOR system performance," *IEEE Trans. Aerosp. Electron. Syst.*, vol. 44, no. 4, pp. 1464–1476, 2008.

[52] D. Jenn and C. Ton, "Wind turbine radar cross section," *International Journal of Antennas and Propagation*, vol. 2012, p. 14, 2012.

[53] A. Naqvi, S. T. Yang, and H. Ling, "Investigation of Doppler features from wind turbine scattering," *IEEE Antennas and Wireless Propagation Letters*, vol. 9, pp. 485–488, 2010.

[54] R. J. Doviak and D. S. Zrnic, *Doppler Radar and Weather Observations*, 2nd ed. Mineola, New York: Dover Publications, INC., 2006.

[55] R. R. Rogers and M. K. Yau, *A Short Course in Cloud Physics*. Butterworth-Heinemann, 1984.

[56] R. J. Doviak, V. Bringi, A. Ryzhkov, A. Zahrai, and D. S. Zrnic, "Considerations for polarimetric upgrades to operational WSR-88D radars," *Journal of Atmospheric and Oceanic Technology*, vol. 17, no. 3, pp. 257–278, 2000.

[57] P. H. Hilderband and R. S. Sekhon, "Objective determination of the noise level in Doppler spectra," *Journal of Applied Meteorology*, vol. 13, pp. 808–811, 1974.

[58] V. C. Chen, *The Micro-Doppler Effect in Radar*. Norwood, MA: Artech House, 2011.

[59] G. T. Ruck, *Radar cross section handbook, Volume I.* Plenum Press, 1970, vol. 1.

[60] R. B. Dybdal, "Radar cross section measurements," *Proceedings of the IEEE*, vol. 75, no. 4, pp. 498–516, 1987.

[61] R. G. Kouyoumjian and J. Peters, L., "Range requirements in radar cross-section measurements," *Proceedings of the IEEE*, vol. 53, no. 8, pp. 920–928, 1965.

[62] R.A.Ross, "Investigation of scattering principles Volume III - analytical investigation," Rome Air Development Center, Tech. Rep., 1969.

[63] "FEKO," http://www.feko.info.

[64] N. K. Patel, G. W. Jim, and A. D. Free, "NEXRAD open radar data acquisition (ORDA) receiver characteristics," in *21st International Conference on Interactive Information Processing Systems (IIPS) for Meteorology, Oceanography, and Hydrology*, 2005.

[65] J. Hubbert, S. Ellis, and M. Dixon, "Weather radar ground clutter. Part II: Real-time identification and filtering," *Journal of Atmospheric and Oceanic Technology*, vol. 26, no. 7, pp. 1181–1197, 2009.

[66] "RaXPol," http://arrc.ou.edu/raxpol.html.

[67] A. L. Pazmany and H. B. Bluestein, "A mobile, rapid scanning, X-band, polarimetric (RaXPol) Doppler radar system," in *35th Conference on Radar Meteorology*, 2011.

[68] "Oklahoma mesonet," www.mesonet.org.

[69] E. Knott, J. Shaeffer, and M. Tuley, *Radar Cross Section*. SciTech Pub., 2004.

[70] D. C. Jenn, *Radar And Laser Cross Section Engineering*, 2nd ed. AIAA, 2005.

[71] R. F. Cleveland, D. M. Sylvar, and J. L. Ulcek, "Evaluating compliance with FCC guidelines for human exposure to radiofrequency electromagnetic fields," Federal Communications Comission, Tech. Rep., 1997.

[72] A. D. Poularikas and Z. M. Ramadan, *Adaptive Filtering Primer with MATLAB*. CRC Press, 2006.

[73] F. Kong, "Wind turbine research at ARRC," http://arrc.ou.edu/~fanxing/WTCresearch.html.

[74] FAA, "DoD preliminary screening tool," https://oeaaa.faa.gov/oeaaa/external/gisTools/gisAction.jsp?action=showLongRangeRadarToolForm.

Appendix A

Scatterometer Part List

Table A.1: Scatterometer RF transceiver part list

Parts	**Vendor**	**Model**	**Quantity**
10.5-GHz Oscillator	Miteq	DLCRO-1-10500-3-15P	1
Power divider	Miteq	PD2-7000/12400-30S	3
SPST switch	Hittite	HMC-C019	1
SPDT switch (fast)	Hittite	HMC-C011	1
SPDT switch	Miteq	SW2-020180AI2NF	3
Power amp.	Miteq	AMF-2B-08001200-45-25P	2
LNA	Miteq	AMF-5F-08001200-15-10P	2
Medium power amp.	Miteq	Legacy part	1
Mixer	Miteq	IRM0812HC2Q	2
Band pass filter	Marki	fb-1050	5
Low pass filter	Minicircuits	BLP-100+	4
Attenuator	Minicircuits	K2-BW3+	1

Appendix B

List of Acronyms and Abbreviations

ACF	Auto Correlation Function
AFRL	Air Force Research Laboratory
AP	Anomalous Propagation
ARMA	Auto Regressive Moving Average
ARRC	Advanced Radar Research Center
ARSR	Air Route Surveillance Radar
ASR	Air Surveillance Radar
ATC	Air Traffic Control
CAD	Computer Aided Design
CSR	Clutter to Signal Ratio
DEM	Digital Elevation Model
DFT	Discrete Fourier Transform
DSP	Digital Signal Processor
EM	Electromagnetic
EMI	Electromagnetic Interference
FAA	Federal Aviation Association
FMCW	Frequency Modulated Continuous Wave
GC	Ground Clutter
GMAP	Gaussian Model Adaptive Processing
GO	Geometrical Optics
GTD	Geometric Theory of Diffraction
HAWT	Horizontal Axis Wind Turbine

HF	High Frequency
IFD	IF Digitizer
IFT	Inverse Fourier Transform
LNA	Low Noise Amplifier
LOS	Line of Sight
MAP	Maximum A Posterior
MCCC	Maximum Cross Correlation Coefficient
MMIC	Monolithic Microwave Integrated Circuit
MTI	Moving Target Indicator
MUSIC	MUltiple SIgnal Classification
NASA	National Aeronautics and Space Administration
NEXRAD	Next Generation Weather Radar
NSSL	National Severe Storm Laboratory
NWS	National Weather Service
OPENEI	OPEN Energy Information
OPP	Oriented Polypropylene
ORDA	Open Radar Data Acquisition
OTH	Over The Horizon
PAR	Phase Array Radar
PBL	Planetary Boundary Layer
PDF	Probability Density Function
PEC	Perfect Electric Conductor
PO	Physical Optics
PR	Public Relation
PRF	Pulse Repetition Frequency
PRI	Pulse Repetition Interval
PRT	Pulse Repetition Time

PSD	Power Spectrum Density
PST	Preliminary Screening Tool
RAM	Radar Absorbent Material
RaXPol	Rapid X-band Polarimetric radar
RCS	Radar Cross Section
RF	Radio Frequency
RIL	Radar Innovation Lab
RMSE	Root Mean Square Error
ROC	Radar Operation Center
RWT^2	Radar Wind Turbine Testbed
SAR	Synthetic Aperture Radar
SCR	Signal to Clutter Ratio
SDR	Software Defined Radio
SNR	Signal to Noise Ratio
SPDT	Single Pole Double Throw
VAWT	Vertical Axis Wind Turbine
VCP	Volume Coverage Pattern
VNA	Vector Network Analyzer
WSR-88D	Weather Surveillance Radar – 88 Doppler
WTC	Wind Turbine Clutter